2012

Evaluation of a proton pencil bean algorithm for dose calculations in heterogenous media

Nels C. Knutson
Louisiana State University and Agricultural and Mechanical College, nknuts1@lsu.edu

EVALUATION OF A PROTON PENCIL BEAM ALGORITHM FOR DOSE CALCULATIONS IN HETEROGENEOUS MEDIA

A Thesis

Submitted to the Graduate Faculty of the
Louisiana State University and
Agricultural and Mechanical College
In partial fulfillment of the
Requirements for the degree of
Master of Science

in

The Department of Physics and Astronomy

by
Nels C. Knutson
B.A., University of Montana, 2007
B.A., University of Montana, 2009
August 2012

Acknowledgements

This work was supported in part by a grant issued by the United States Department of Defense (DOD). This research was supported by contract W81XWH-10-1-0005 awarded by The U.S. Army Research Acquisition Activity, 820 Chandler Street, Fort Detrick, MD 21702-5014. This report does not necessarily reflect the position or policy of the Government, and no official endorsement should be inferred. I would like to thank the DOD for their funding of this project and continued support for future work on this project. I would like to thank Louisiana State University (LSU) and Mary Bird Perkins Cancer Center (MBPCC) for providing financial support and other great resources to me during my three years here. I would like to thank the High Performance Computing (HPC) at LSU for all of their time, resources, and help. This project would not have been possible without HPC. Portions of this research were conducted with high performance computational resources provided by LSU (http://www.hpc.lsu.edu).

I would like to thank Dr. Jonas Fontenot and Dr. Kenneth Hogstrom for having great foresight and faith in me when giving me this project. Prior to being selected for this project, I had indicated I was interested in protons and shielding and had also stated that I was a terrible programmer. I was not well versed in MCNPX, LINUX, the details of charge particle transport, nor had I heard of the Cauchy Lorentz distribution when I started this project. I was a little concerned to say the least. However, it has been one of the most rewarding and fun challenges I have ever experienced. Without Dr. Fontenot encouraging me to learn these new materials I would have never been able to accomplish this project or have the great satisfaction that came from learning these skills.

I would also like to thank John Chapman for helping me learn this very difficult material and putting up with my constant questions. It was extremely fun and rewarding to work on this project and I could not have done it without John's help. I would also like to thank Michael Thomas for helping me put the PBA on the HPC cluster. This step saved me a lot of time. I would also like to thank Alex Pacheco at HPC for helping to start running MCNPX and all of the headaches that go along with that. I would like to thank both Mike and Alex for putting up with my Linux illiteracy; as Dr. Fontenot says, I am a Bill Gates victim.

I would like to thank my committee (Dr. Kenneth Hogstom, Dr. Wayne Newhauser, Dr. Jonas Fontenot, and Dr. Catherine Deibel) for all of their guidance in this project. It has been invaluable to have so much and such a variety of expertise at my disposal. It has been a pleasure to work on the development of a proton pencil beam algorithm under the guidance of experts in pencil beam transport, Monte Carlo transport, and charge particle transport in general.

I would also like to thank the entire LSU Medical Physics & Health Physics department for giving me the strong didactic background that made this project possible. I would like to thank Dr. Kip Matthews, Dr. Polad Shikhaliev, and Dr, Wei-Hsung Wang for providing a great learning experience. I would also like to thank Yvonne Thomas and Susan Hammond for helping me get everything together, scheduling all of my committee meetings, and making sure to catch my screw ups in paperwork. Also, I would like to thank all of my colleagues and friends here at LSU for listening to me ramble about protons and letting me bounce ideas off of them. In particular I would like to thank Tony Mazza who has been a giant inspiration. Tony's upbeat and unwavering faith when dealing with adversity has been a huge inspiration to me. I have had a great experience at LSU and I will look back at my days here fondly; I would just like to thank everyone who made that possible.

I also have to thank all of the people who helped me get here. I would like to thank everyone at the University of Montana Physics department. I would like to thank Dr. David Andrews for introducing me to Medical Physics and teaching me the core upper division physics courses. I would like to thank Dr. James Jacobs for introducing me to the wonderful world of Physics. My life changed in 2003 when I took Physics 221 from Dr. Jacobs, just as so many other students who Dr. Jacobs inspired. I have heard so many people say "Dr. Jacobs was the reason I did physics." I know this is true for me. Numerous times I told Dr. Jacobs he was the best teacher I have ever seen and he would always brush it off and say it's just the physics people love. Dr. Jacobs loved to teach and loved physics so much. There was nothing like seeing his excitement and love for what he was doing. I wish he could have read this and known what a gift he had given me when he first sparked my interest in physics. I wish I could tell him the he was an amazing teacher, friend, and person. I miss Dr. Jacobs very much and I wouldn't be here today if it weren't for him.

I would also like to thank my family for all of the help and support they have given me over the years. My mother, father, step father, step mother, and little sister have provided unbelievable amounts of support all throughout my life and I could not have done this without them. I would like to thank my mother for teaching me strong study skills early in life. I owe all of my success to my mother, who as a single parent raised two kids while going to school. She received her BS in Electrical Engineering from the University of North Dakota when I was in third grade and my sister was in first grade. She has always been a great inspiration and is responsible for my academic achievements.

Finally I would like to dedicate this work to Dr. James Jacobs who passed away in August of 2011.

Table of Contents

List of Tables

List of Figures

Abstract

Purpose: To develop an improved nuclear halo dose model of a pencil beam algorithm (PBA) for dose calculation of proton beams in heterogeneous media.

Methods: The proton PBA consisted of a central axis term and an off axis term. The central axis term was determined from a central axis depth dose profile of a Monte Carlo simulated proton beam in water and was scaled by a mass stopping power ratio to account for other materials. The off axis term was determined from Fermi-Eyges scattering theory with material-dependent scattering powers to calculate the lateral spread of the proton beam in heterogeneous media. The nuclear halo dose, which was caused by large angle and non-elastic scattering events, was modeled using two terms: a Gaussian distribution and a Cauchy-Lorentz distribution. Depth-dependent widths and amplitudes of each distribution were determined by fitting a simulated 1-mm x 1-mm pencil beam in water. The PBA was evaluated in approximately 30 test phantoms containing bone and/or air heterogeneities at 4 energies and for 2 field sizes. Agreement between PBA and Monte Carlo simulations of the test conditions was quantified by computing the percentage of points within 2 percent dose difference or 1 mm distance to agreement.

Results: With the improved nuclear halo model, PBA calculations showed better than of 97% of dose points within 2% or 1 mm of MC distributions for all geometries examined. For phantoms containing laterally infinite heterogeneities, agreement between PBA and MC distributions was 100% at 2% or 1mm. For phantoms containing laterally finite heterogeneities, agreement was at least 97%. The points failing were due to the central axis approximation of the PBA in regions not influenced by the nuclear halo model.

Conclusions: The nuclear halo model developed in this work improves the agreement of the PBA with MC simulations in heterogeneous phantoms, particularly in low-dose regions that can be important for scanned-beam proton therapy.

Chapter 1: Introduction

1.1 Background and Significance

1.1.1 Physics of Proton Radiation Therapy

Radiation is used to treat cancer by depositing energy into tumors. Different types of radiation exhibit different energy deposition characteristics. As will be shown, high-energy protons offer fundamental advantages in energy deposition over other types of therapeutic radiation such as photons. The dosimeteric benefits of protons come to light in the physics of the interactions between the protons and different materials.

Interactions between protons and matter can be broken up into three main categories: energy loss, scattering, and nuclear interactions.

1.1.1.1 Energy Loss

Protons lose their energy predominately by the excitation and ionization of orbital electrons of the target media. The mechanism of this interaction is the Columbic force between the proton and the electron. This can be described by imaging the following scenario described by Turner (2004). Imagine a proton traveling at a velocity V through a ring db thick by dx wide with a radius b (Figure 1.1). Further imagine there is an electron located in this ring that will feel a Columbic force from the proton as it approaches.

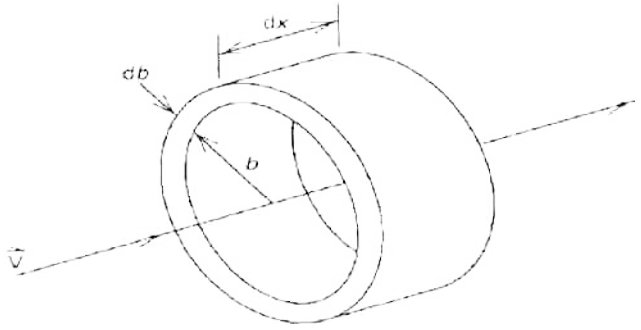

Figure 1.1: The geometry of a proton with velocity V interacting with an electron located in the ring with a thickness db, width dx, and a radius b. Figure from Turner (2004).

If one starts with Newton's second law (Eq. 1), the momentum p imparted on the electron from the proton via the Coulomb force can be determined. Assuming that the net force along the direction of travel of the proton is 0, the force is completely in the perpendicular direction.

$$\frac{dp}{dt} = F = k_o z e^2 \frac{\cos\theta}{r^2} = k_o z e^2 \frac{b}{r^3} \quad (1)$$

Where, b is the impact parameter or perpendicular distance between the proton and electron, r is the straight line distance between the proton and the electron, ɵ is the angle between r and b, ko = 8.9876 x 10^9 Nm^2 C^{-2}, e is the charge of an electron, z is the atomic number of the projectile and ze is the charge of the projectile. By integrating over time as shown by Turner (1995), the energy lost by a proton (Q) from a single electron located in the ring is inversely proportional to the energy of the proton and is shown below.

$$Q = \frac{p^2}{2m} = \frac{2k_o^2 z^2 e^4}{mV^2 b^2} \quad (2)$$

Where V is the velocity of the proton, and m is the mass of the proton. The differential energy deposited to n electrons per unit volume in the ring is then

$$-dE = \frac{2k_o^2 z^2 e^4}{mV^2 b^2}(2\pi n b\, db\, dx) \quad (3)$$

The differential energy loss per infinitesimal distance dx is the called the linear stopping power and can be found from equation number three by integrating with respect to b.

$$\frac{-dE}{dx} = \frac{4\pi k_o^2 z^2 e^4 n}{mV^2}\int_{b_{min}}^{b_{max}} \frac{db}{b} = \frac{4\pi k_o^2 z^2 e^4 n}{mV^2} ln \frac{b_{max}}{b_{min}} \quad (4)$$

Equation 4 predicts a large and infinitesimally narrow peak of energy deposition as the protons approach zero energy. This is called the pristine Bragg peak and, depending on the incident energy, occurs at different depths. In reality, each proton undergoes stochastic energy loss, causing a broadening of the Bragg peak called range straggling. Because of range straggling and variations in path lengths due to scattering, the Bragg peak has a width that can be described by a Gaussian. Since all incident protons stop at nearly the same depth,

Gottschalk (2009b) determined the rms width of Bragg peak is approximately 1% -1.5% of the range, i.e. the depth of distal 80% of Bragg peak (d_{80}). A full quantum mechanical and relativistic treatment of the problem has been shown by Bethe (1930). Berger (2005) computed the stopping powers for protons in this manner and the stopping power of protons in water can be seen in Figure 1.2. The Bragg peak and the finite range of protons have been the largest motivations for their use in radiation therapy (Figure 1.3).

Figure 1.2: Linear stopping power for liquid water plotted vs. proton energy. Data from Berger (2005).

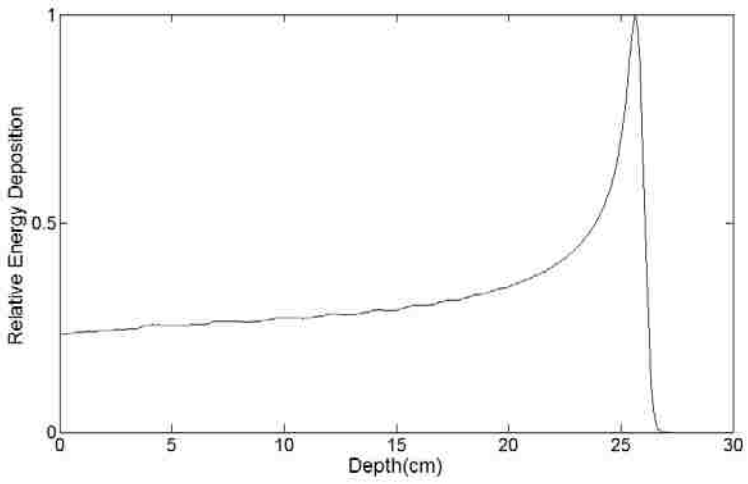

Figure 1.3: Relative energy deposition vs. depth for a 250 MeV proton beam incident on water.

1.1.1.2 Scattering

The scattering of protons is predominantly due to the Columbic elastic interactions with the target nucleus, resulting in small angular deflections with minimal energy loss. Deflections of the

proton due to the Coulomb force can be categorized as multiple Coulomb scatter (most common), plural scatter (less common), and single scatter (least common). Multiple Coulomb scattering (MCS) is defined as many small angle scatter events. Single scatter is defined as a single relatively larger deflection than the deflections caused by MCS. Plural scattering is defined as an intermediate number of scattering events between single and multiple scattering. Even though these interactions occur with the nucleus, they are not generally referred to as nuclear interactions as they are due to the electromagnetic force, not the nuclear force. The term nuclear interaction will be reserved for inelastic and non-elastic collisions with the nucleus which is discussed later.

The distribution of charged particles incident on a thick target was described by Moliere (1948) and the application of this work to protons was provided by Gottschalk (1992). The distribution is characterized by a Gaussian first term combined in a power series with higher order terms. Due to the complex form of this distribution, it is desirable make approximations to this theory that can be more easily adapted for use in dose calculation. Gottschalk (2009a) provides a review of different approximations to Moliere theory and their accuracy.

1.1.1.3 Nuclear Interactions

Nuclear interactions between incident protons and the nucleus can be classified into three categories: elastic, inelastic and non-elastic. Elastic interactions occur when a proton and the target nucleus interact and all the kinetic energy is conserved between these two bodies (this is exclusive of Coulomb scattering). The target nucleus after this interaction remains in the ground state. By contrast, inelastic interactions do not conserve kinetic energy between the two bodies, because some of the kinetic energy of the incident proton is transferred to the target nucleus, elevating it to an excited state. Finally, non-elastic interactions with the target nucleus occur when the kinetic energy is not conserved between the two bodies and part of the incident energy is used to overcome binding energy in the target nucleus. This results in secondary particle production. Possible secondary particles include protons, neutrons, alphas, other heavy

fragments, gamma rays, and the residual recoil nucleus of the target. An example of each interaction type is listed in Table 1.1

Table 1.1: Example proton nuclear interactions (Gottschalk 2009b).

Interaction type	Example reaction
Elastic	$p + {}^{16}O \rightarrow p + {}^{16}O$
Inelastic	$p + {}^{16}O \rightarrow p + {}^{16}O^{*}$
Non-elastic	$p + {}^{16}O \rightarrow p + p + {}^{15}N$

In summary, the physics of protons interacting with matter can be broken up into three main categories: inelastic Coulomb interactions with orbital electrons that are responsible for the majority of the energy loss of the protons; elastic Coulomb interactions with the nucleus that are responsible for the majority of lateral deflections of the protons; inelastic interactions with nucleus that are responsible for energy loss, scatter, fluence loss and secondary particle production.

1.1.2 Basic Principles of Proton Radiation Therapy

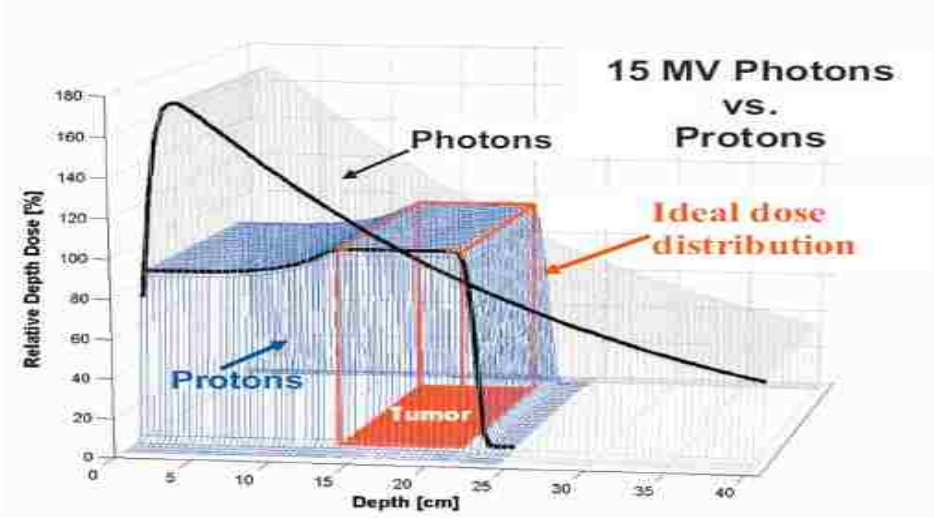

Figure 1.4: Dose distribution comparison between photons and protons. This highlights two key advantages of protons; finite range and target conformity with one beam. Figure from Smith (2009a).

Consider a tumor located at depth (Figure 1.4). The goal is to kill the tumor with a given dose (energy per unit mass), while also minimizing the dose delivered to the normal, healthy tissue. For deep seated tumors this has been accomplished in the past with high energy x-ray beams of 4-20 MV. X-rays or photons deposit energy in the patient by producing secondary electrons in the patient, which in turn, excite and ionize more electrons. This causes a buildup in dose until there is equilibrium between the number of electrons being produced and the number of them stopping (e.g. charged particle equilibrium). After charged particle equilibrium is established, dose decreases with depth as photon fluence is exponentially attenuated. Since the maximum dose is delivered near the skin, deep-seated tumors must be treated with multiple beams to avoid over dosing regions proximal to the tumor. This increases the integral dose to the patient and more normal tissues are treated.

In contrast, proton beams if the appropriate energy (100-250 MeV) can reach the target while depositing less dose proximal to the target and insignificant dose to tissues distal to the target (Figure 1.4). The peak of monoenergetic proton beam is called a pristine Bragg peak; however multiple peaks of beams with different energies summed together with the proper weighting are typically used to create a spread out Bragg peak (SOBP) that covers the target in depth (Figure 1.5).

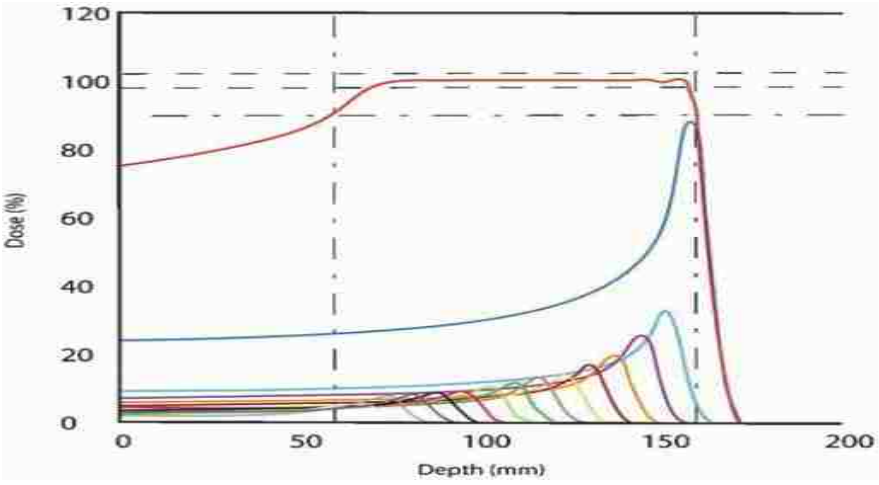

Figure 1.5: The addition of multiple pristine peaks adds up to a spread out Bragg peak that covers the target while still sparing everything behind it. Figure from Kahn (2010).

. Unlike the target shown in Figure 1.5, tumors are not often at a uniform depth with constant thickness and in a homogenous medium. Imagine something a little more realistic, a non-uniform tumor with a critical structure behind it and heterogeneous tissue in front of it (Figure 1.6). The goal is to deliver the dose to the target volume and spare as much healthy tissue as possible while taking particular care in avoiding critical structures. With proton therapy there are two modality options to accomplish this, passively scattered proton therapy and scanned beam proton therapy. In both cases the proton beam starts out as a very narrow pencil beam that needs to be either spread out or scanned to cover the target.

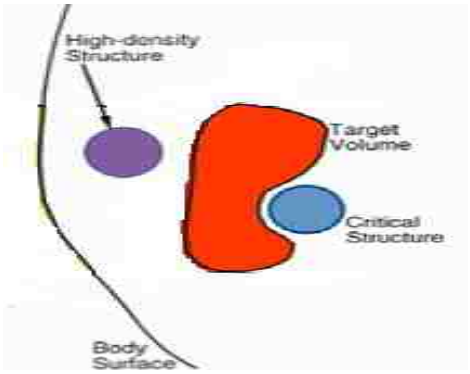

Figure 1.6: Image of a patient geometry. Figure adapted from Chu et al (1993).

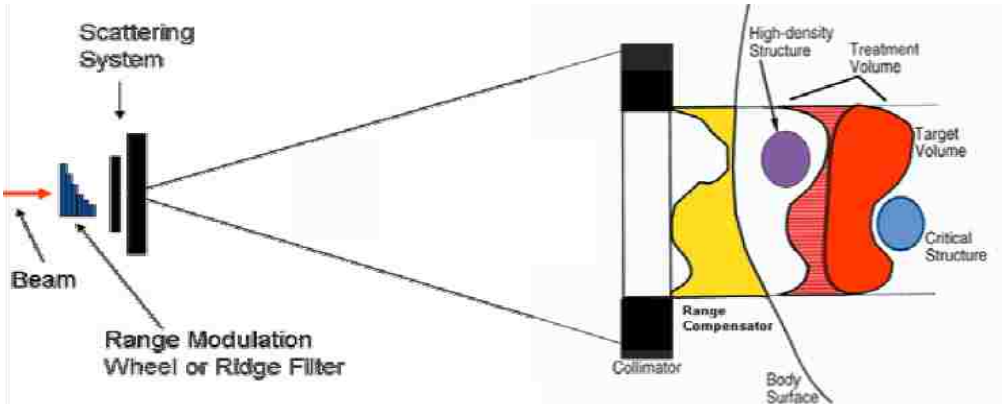

Figure 1.7: Schematic of a typical passive scattering system. Note the treatment volume conforms to the lateral and distal edges but does not conform to the proximal edge of the target volume. Figure from Chu et al (1993). Note the area in red is receiving 100% of the treatment dose.

In passive scattering a spread out Bragg peak is created by using a rotating range modulator wheel. The range modulator wheel has different thickness and width steps of a low z material.

The wheel is rotated in the beam to select the depth and intensity of each pristine peak to be added to make the SOBP. The range of each pristine peak is selected by the thickness of the step in the wheel, and the intensity of the peak is selected by the width of the step in the wheel. This insures that the spread of Bragg peak covers the full extent of the target, from the distal most edge to the proximal most edge.

Next the beam is laterally broadened using a dual foil scatter system. The first foil consists of high atomic number (Z) material and is used to spread the original small beam out to a larger Gaussian shape. A second composite low Z and high Z foil is used to flatten this beam. The high Z material is used in the middle to spread out the Gaussian core. The low Z material is used to produce the same amount of energy loss along the edges. This produces a flat uniform beam that can cover the tumor. A collimator near the patient is then used to conform this uniform beam laterally to the shape of the target volume.

To conform the dose to the distal edge of the target, a water equivalent range compensator is used (Urie et al. 1984). The compensator is designed with as little or as much water equivalent material as needed to make sure the distal edge of the spread out Bragg peak conforms to the distal edge of the target. Materials with low atomic number are desirable for a compensator because the goal is modulate the range of the protons not spread them out. Since scattering is dependent on Coulomb interaction with the nucleus and energy loss is dependent on Coulomb interaction with orbital electrons it is beneficial to use low atomic number materials to minimize scatter relative to the energy loss in the compensator.

Since energy loss is a function of electron density, heterogeneities have a significant effect on the range of the protons. Thus, one must be cognoscente of the path length of protons traveling to the target. The path length of a proton passing through different media is usually compared to the path length as if it was passing through water only. For instance, 250 MeV protons lose approximately 1.7 times the energy going through one cm of bone compared to one cm of water. A 250 MeV proton beam incident on a water phantom will have a range of

approximately 38 cm. If two centimeters of bone is inserted in the water phantom the range will be reduced to approximately 36.55 cm, because the two centimeters of bone is equivalent to approximately 3.45 cm of water. Therefore the bone causes a reduction in the range of 1.45 cm. It is very important to take this into account when designing the compensator and selecting the correct range modulator wheel to ensure the target volume is covered.

The largest drawback of the passive scattering system is that the dose is only conformed to the distal edge of the target volume and not to the proximal side of the target (Figure 1.7). Since the spread out Bragg peak is designed to cover the thickest part of the target volume conformity to the proximal side is lost on any part of the tumor that is thinner. This will lead to normal tissue upstream of the target being treated to the full treatment dose.

The use of multiple beams reduces doses to proximal tissues: For example, consider two apposed beams (Figure 1.8), for which case the dose distal to the tumor now increases. Essentially the non conformity of the proximal side of target volume is still occurring but since multiple beams are used the overdosed area receives a fraction of the treatment dose instead of the full treatment dose. This comes at the expense of raising the integral dose. Therefore it is a balancing act of the area receiving radiation vs. the amount of the radiation received outside the treatment volume. The use of multiple beam (>2) and their direction is optimized as part of the treatment planning process.

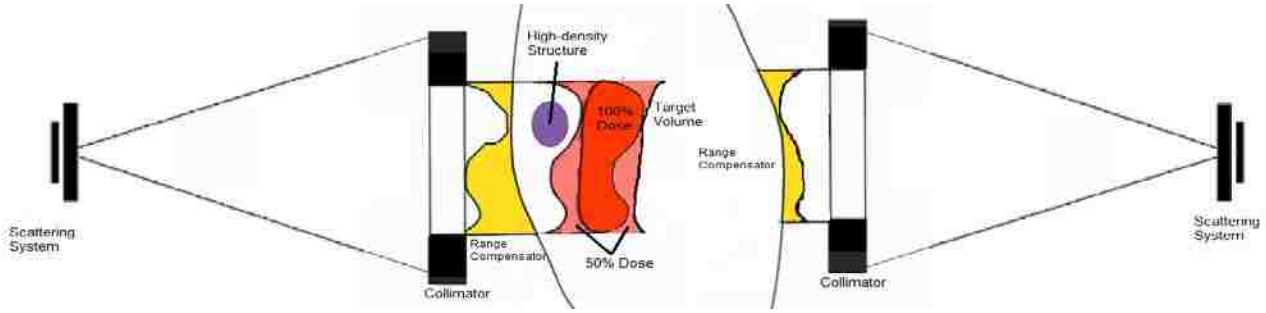

Figure 1.8: Schematic of a passively scattered two beam technique. The red area is receiving 100 percent of the treatment dose. The pink area outside would be receiving 50 percent of the treatment dose. In Figure1.5 both areas would correspond to 100 percent of the treatment dose. Note the absence of the critical structure on the right of the target volume. Structures around the target volume determine which technique is appropriate. Figure adapted from Chu et al (1993).

An alternative to passive scattering is pencil beam scanning (Figure 1.9). Pencil beam scanning systems use magnets to scan the narrow proton beam back and forth to cover the target instead of scattering it out to cover the target. To do this, the target is broken into spots layered with depth. At every layer the pencil beam energy is selected to match the range with that depth and the beam is scanned across the target. The process is repeated for the next layer and then the next until the tumor is covered. By doing this dose is conformed to the target on all sides of the target and the problem of excess dose on the proximal side of the target is taken care off.

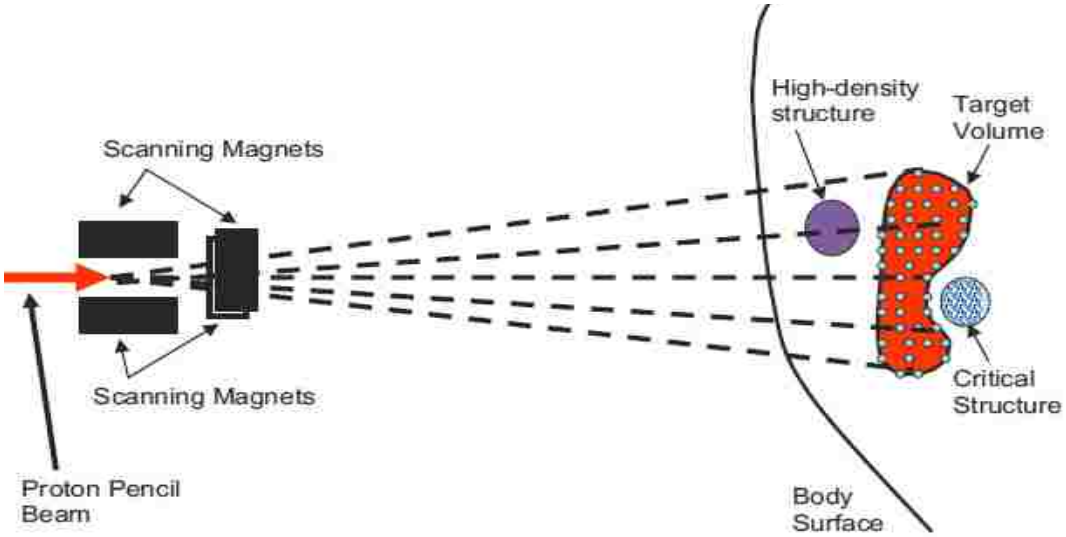

Figure 1.9: Schematic of typical proton pencil beam scanning beam system. The treatment volume is conformed on all sides of the target volume. Figure from Chu et al (1993).

1.1.3 Dose Calculation and Treatment Planning Systems

Regardless of the manufacturer or modality type in order to use protons clinically one must be able to plan the treatment of the patient. Treatment planning systems allow physicians to simulate multiple treatment scenarios for a given patient in order to arrive at a final treatment plan that maximizes the therapeutic ratio. To accomplish this goal, a treatment planning system requires the patient's anatomical data, contouring anatomy, beam selections, optimization, dose calculation, and dose analysis tools. The dose delivered to the target volume and surrounding tissues is calculated and visualized on the patient anatomical data. This must be an accurate

dose calculation. Several techniques of dose calculation for proton therapy have been reported: Monte Carlo methods, convolution algorithms, broad bream algorithms and pencil beam algorithms.

Monte Carlo methods for dose calculations of proton beams have been shown to be in very good agreement with measurement in previous works (Pedroni 2005, Soukup 2005, Titt 2008, and Zheng 2007). This has lead Monte Carlo techniques to become the gold standard in dose calculation for protons. The idea behind Monte Carlo methods is to track each proton individually and model the physics of each interaction with probability distributions. A table of stopping powers along with a correction for range straggling are used to model energy loss as the proton is transported. A probability distribution to model Coulomb scatter from scattering theory is used along with distributions for the different nuclear interactions described in section 1.1.1. The probabilities of nuclear interactions are taken from models or measured data. Knowing the energy of the proton and the probability distributions of the different interactions, a random sample is taken from those distributions to determine what happens to the proton. After each interaction, the amount of energy lost and the particle's displacement is tracked and the process is repeated until the proton is out of energy.

In general, Monte Carlo methods are much slower computationally than analytical methods. Although assumptions can be made to improve the computing speed; this comes at the expense of accuracy. As computing power continues to grow and become less expensive Monte Carlo methods may become more viable for clinical use; however, at present, Monte Carlo dose calculations are considered too slow for routine clinical use in proton therapy.

Convolution methods work as the name suggests; dose is determined from the convolution of fluence and a dose kernel. The dose kernel is the dose distribution from an infinitesimally wide proton beam incident on water. The dose of kernel itself is described by a central axis term and an off axis term stored in look up tables. These values can be derived from measurements or Monte Carlo simulations in water. The fluence is parameterized as a function

of depth using measurements in air downstream of all scattering devices in the beam. The total dose is then given by the convolution of all the infinitesimal kernels in the field and the proton fluence. This is shown in Eq. 5 from Schaffner (1998) and visually in Figure 1.10. Note that the kernel is a function of energy, which is controlled by the number of range shifter plates (N_{rs}). . In order to account for different materials in the beam, the water equivalent range (wer) is tracked similarly to the process used for the design of the compensator of passively scattered proton beam. For example in Figure 1.10 note the scaling of the range of the different beamlets traveling through different materials

$$D(x, y, z, N_{rs}) = \sum_{\bar{y}} \sum_{\bar{x}} \Phi(x - \bar{x}, y - \bar{y}, z, N_{rs}) K(\bar{x}, \bar{y}, wer(\bar{x}, \bar{y}, z), N_{rs}) \quad (5)$$

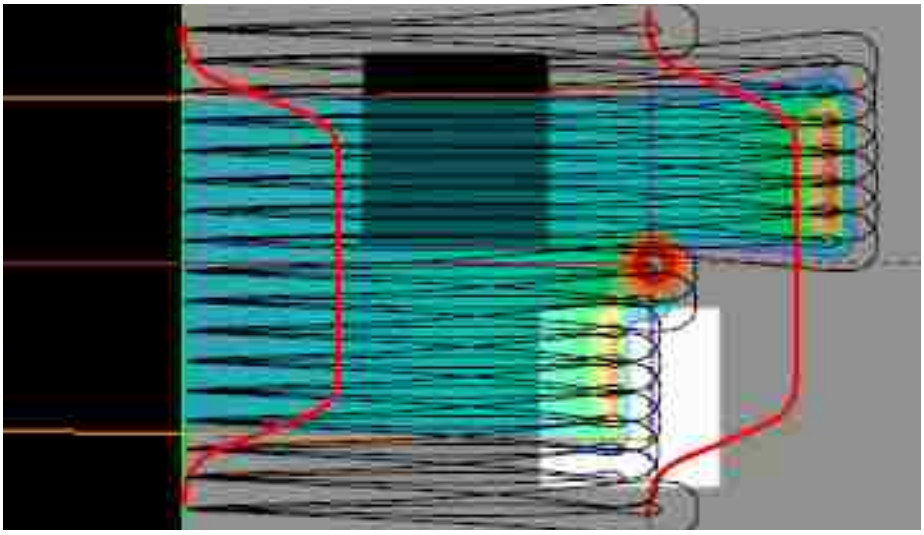

Figure 1.10: Example of a dose kernel convolution method. This describes a proton beam incident on a water phantom containing two heterogeneities (high density in white and low density in black). Fluence (profiles plotted in red at two depths) have been calculated for each depth and the beam has been split up into beamlets (seen in black). The ranges of the beamlets are scaled to account for the heterogeneities. The convolution of these two gives dose (seen in the color map). Figure from Schaffner (2007).

The convolution method provides a quick way to calculate dose, but there are a few drawbacks. The models of the dose kernels are all derived from water, whereas the true width of a dose kernel should be material dependent and dependent on the depth and size of the material as well. In this model only the central axis depth dose or range of the kernel is scaled. There is also a problem with the kernels near a material with sharp lateral edge. Whatever is

along the central axis of that kernel is used to determine the range of the entire kernel. This is called the central axis approximation. For example, if nearly half the kernel is in water but the center of the kernel is in air it assumes the range of the entire kernel is extended. In actuality, the kernel would be split, with nearly half having the nominal range in water, nearly half having the increased from going through air, and some small portion being in-between. This occurs whenever there is heterogeneity with a sharp lateral edge and causes the analytical model to underestimate dose (cold spot) in some areas and overestimate it (hot spot) in others. A good example of this can be seen in Figure 1.11 when a bone slab is placed in the field. Since the central axis is dictating the range of the entire kernel, the kernels near the sharp lateral edge suffer from the central axis approximation. When all the kernels are summed up one can see two cold spots and two hot spots behind the heterogeneity. Kernels on the bone slab side have a reduced range and conversely the kernels on the water side of slab have the nominal range in water. These assumptions are wrong for kernels near the edge and cause the hot and cold spots.

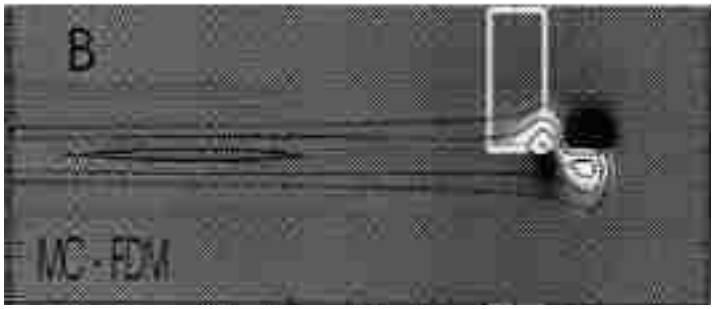

Figure 1.11: Dose distribution calculated with dose kernel convolution model. A subtraction of Monte Carlo simulated dose distribution and the calculated distribution is overlaid. Areas in white represent a cold spot with a magnitude >10% of the maximum dose and similarly the black represents a hot spot of >10% of the maximum dose. Figure from Schaffner (1998).

A pencil beam algorithm splits the field into infinitesimal segments called pencil beams. A pencil beam is defined as the charge particles passing through that infinitesimal area (Figure 1.12). In practice this area is represented by a pixel of finite size (~0.5 x 0.5 – 2 x 2 mm^2) and there is a discrete sum of N pencil beams. The dose from each pencil beam is described by a central axis term (CAX) and an off axis term (fluence). It is important to note that pencil beam

algorithms also use the central axis approximation and it also assumes that a material at a depth Z along the central axis of a pencil beam is laterally infinite. The total distribution is given by summing up the dose of all the individual pencil beams (Eq. 6).

$$D_i(X,Y,Z) = D_\infty(0,0,Z) \cdot F(X,Y,Z) \quad (6)$$

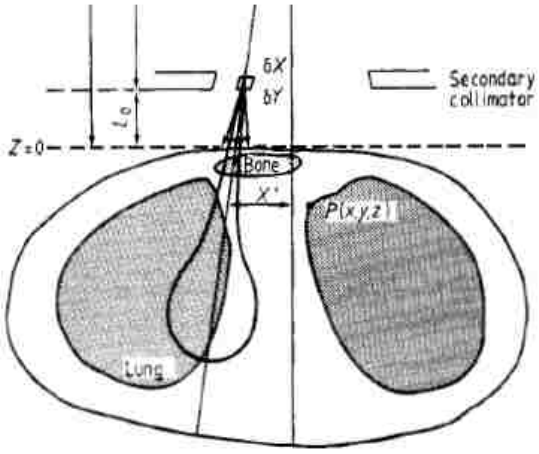

Figure 1.12: Example of a single pencil beam in a field. The total dose from the field would be the summation of all the pencil beams across the field. Figure from Hogstrom (1981).

The central axis term of each pencil beam may be given by a measured central axis depth dose profile, but can also be calculated from the energy loss equations. However, use of measured data is advantageous as it intrinsically includes energy loss, range straggling, and fluence losses due to nuclear interactions. The central axis term is typically acquired from a large field (measured or Monte Carlo calculated), which is corrected to an infinitely broad beam with side scatter equilibrium. This ensures that the central axis is only modeling energy loss and the off axis term is modeling scattering. The off axis term is derived from scattering theory of charge particles. As mentioned in section1.1.1, the Gaussian distribution is a good approximation of the proton scatter distribution and is easily integrable. The width of the distribution is determined from scattering theory as a function of depth.

With these two terms one can calculate dose as function of off axis position (X,Y) and depth Z from a single pencil beam of width Δx by Δy centered at (x_i,y_i) (Eq. 7). The summation of N pencil beams gives the total dose (Eq. 8).

$$D_i(X,Y,Z) = D_\infty(0,0,Z) \int_{x_i-\frac{\Delta x}{2}}^{x_i+\frac{\Delta x}{2}} \frac{1}{\sqrt{2\pi}\sigma_x(Z)} exp\left[\frac{-[(X-x')^2}{2\sigma_x(Z)^2}\right] dx' \times \int_{y_i-\frac{\Delta y}{2}}^{y_i+\frac{\Delta y}{2}} \frac{1}{\sqrt{2\pi}\sigma_y(Z)} exp\left[\frac{-[(Y-y')^2}{2\sigma_y(Z)^2}\right] dy' \quad (7)$$

$$D_{tot}(X,Y,Z) = \sum_{i=1}^{N} D_i(X,Y,Z) \quad (8)$$

Pencil beam algorithms are similar to convolution algorithms but differ in how heterogeneities are handled. While both types of algorithms are limited by the central axis approximation, the off axis and central axis terms of the PBA are material dependent, unlike convolution methods where only the central axis term is material dependent. In cases where there are laterally infinite heterogeneities, pencil beam algorithms correctly account for changes in range and scatter where the dose kernel convolution method would account for only the former.

There are two commercial proton treatment planning systems available in the United States: the first is a dose kernel convolution method based on the work of Schaffner (1998) (Eclipse, Varian Medical Systems, Palo Alto, CA); the second uses two different pencil beam algorithms (Xio, Elekta, Ltd., Stockholm, Sweden); a pencil beam algorithm based Hong *et al.* (1996) for passively scattered beams, and a pencil beam algorithm based on Soukup *et al.* (2005) for scanned beams. These algorithms have performed well, however improvements to their multiple Coulomb scatter models and nuclear models of these algorithms is possible. The details of these improvements will be discussed in greater detail when discussing the methods of this work. Recently, our group has begun developing a Proton PBA in an effort to make these improvements.

1.1.4 Testing the PBA in Water (Chapman 2012)

The accuracy of our PBA was evaluated by comparing dose distributions in water phantoms with predictions from Monte Carlo simulations by Chapman (2012). This was done for proton beam energies of 50, 100, 150, 200, and 250 MeV, and field sizes of 4x4 and 10x10 cm^2. Results were compared for flat water phantoms, step water phantoms, and beams of oblique incidence on flat water phantoms. Each distribution was calculated on a 1x1 mm^2 grid and compared between the two calculation methods. All distributions were normalized to the maximum dose in a flat water phantom of the given energy and field size. A 2% dose difference or 1 mm distance to agreement criteria was used to test all points out to a 1% dose cut off. Sample results are shown in Figure 1.13. For all forty geometries tested, the dose distribution calculated by the PBA had greater than 99 percent of points within 2% or 1mm of Monte Carlo simulated dose distributions. The reader is referred to Chapman (2012) for a more detailed discussion of the previous results.

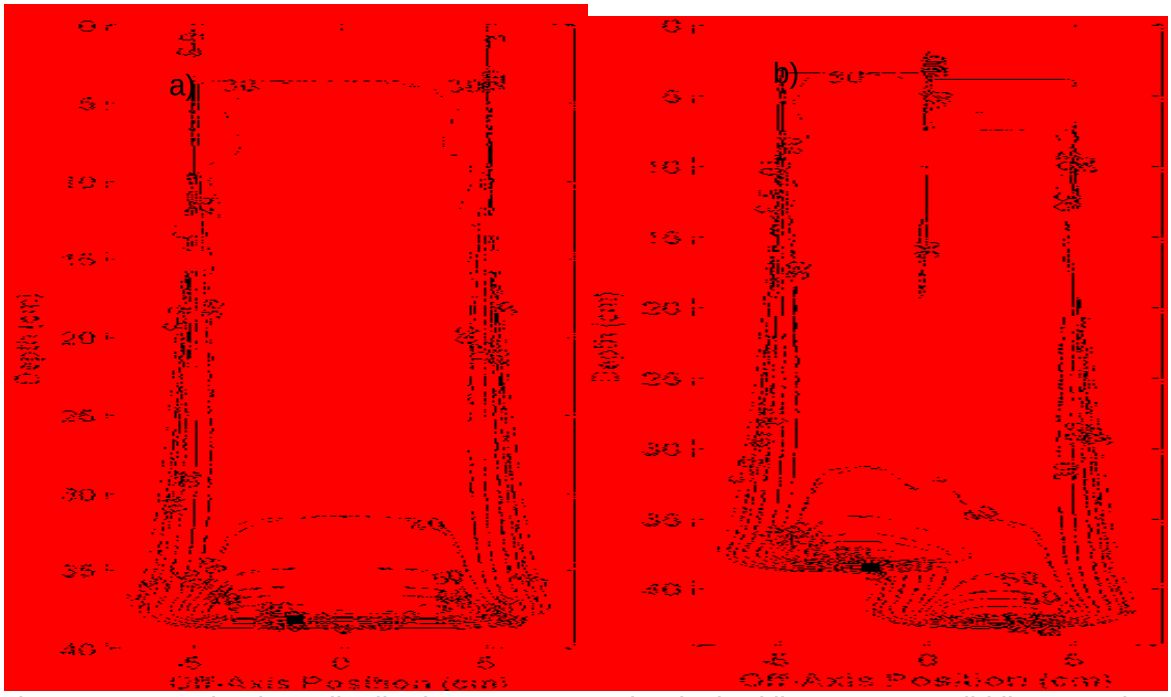

Figure 1.13: 2D isodose distributions, Monte Carlo: dashed lines. PBA: solid lines. Points not meeting the 2% or 1 mm criteria where marked with a red pixel. a) 250 MeV 10x10 cm^2 flat water phantom. b) 250 MeV 10x10 cm^2 water phantom with a 4 cm step. >99% of points are passing in both distributions with a few failure points in the low dose low area on the edge of the field. Figures from Chapman (2012).

1.2 Motivation for Research

While PBA calculation agreed well with Monte Carlo simulations, the algorithm only calculated dose in water. While water is a good approximation to human tissue, patients also consist of low density materials (air), high density materials (bone), and everything in between (soft tissue, fat, muscle, etc.). Since these heterogeneities can influence scattering and energy loss, they must be accounted for in order for the PBA to be used clinically.

Additionally, agreement between the PBA and Monte Carlo simulations in water was poorer in very low dose regions (<5% isodose). This observation may indicate a deficiency in the nuclear halo term used to calculate the dose form non-elastic and single scatter events. This can be particularly important when calculating the dose from a scanned pencil beam.

To address these issues, this work was undertaken with the following objectives: adapt the PBA for calculation in heterogeneous media, improve the nuclear halo model, and determine the accuracy of the PBA by comparing PBA dose calculations to Monte Carlo simulations.

1.3 Hypothesis and Specific Aims

The hypothesis of this work was that a pencil beam algorithm will predict dose to a heterogeneous phantom (simulating human tissues) delivered by a uniform parallel monoenergetic proton beam within 2% dose difference or 1 mm distance to agreement of Monte Carlo simulated dose distribution of the same geometry. Phantoms including bone and air heterogeneities of different sizes at different depths were studied for four energies (100, 150, 200, and 250 MeV) and two field sizes (4x4 and 10x10 cm^2). This hypothesis will be tested by the following specific aims: (1) modify the PBA to account for heterogeneities, (2) improve the accuracy of the nuclear halo model in the PBA, and (3) evaluate the accuracy of the pencil beam algorithm.

Chapter 2: Methods

2.1 Design of our PBA

Our group originally developed a PBA to calculate dose from a monoenergetic and monodirectional proton beam to a water phantom (Chapman 2012). The general implementation of the pencil beam algorithms follows the work by Hogstrom (1981) for electron beams.

In this work it was assumed that all (Y,Z) planes of the phantoms were the same as the (X,0,Z) plane. This was done to simplify the calculations and for convenience. Dose calculations were performed along the (X,0,Z) plane and it was assumed the pencil beams were infinite in the Y direction. Therefore,

$$D_i(X,0,Z) = D_\infty(0,0,Z) \int_{x_i-\frac{\Delta x}{2}}^{x_i+\frac{\Delta x}{2}} \frac{1}{\sqrt{2\pi}\sigma_x(Z)} exp\left[\frac{-[(X-x')^2]}{2\sigma_x(Z)^2}\right] dx' \times \int_{-\infty}^{+\infty} \frac{1}{\sqrt{2\pi}\sigma_y(Z)} exp\left[\frac{-[(0-y')^2]}{2\sigma_y(Z)^2}\right] dy' \quad (9)$$

The integral of the Gaussian along the Y direction in equation 9 from -∞ to +∞ equals 1. Thus the three dimensional calculation can be reduced to two dimensions.

$$D_{tot}(X,0,Z) = \sum_{i=1}^{N} D_i(X,0,Z) = \sum_{i=1}^{N} D_\infty(0,0,Z) \int_{x_i-\frac{\Delta x}{2}}^{x_i+\frac{\Delta x}{2}} \frac{1}{\sqrt{2\pi}\sigma_x(Z)} exp\left[\frac{-[(X-x')^2]}{2\sigma_x(Z)^2}\right] dx' \times 1 = D_{tot}(X,Z) \quad (10)$$

The dose was divided up into two terms: a central axis term and an off axis term just like in Equation 6 except with the assumptions made in equations 9 & 10. The central axis term was taken from the central axis depth dose of Monte Carlo simulated protons beams. Unlike the Hong algorithm, the off axis was divided in two terms: a primary term to model multiple Coulomb scatter and a nuclear halo term to model single and plural Coulomb scatter, along with inelastic

and non-elastic nuclear scatter. Two term calculations have shown improvements in the accuracy of pencil beam algorithms over single term calculations (Chapman 2012, Soukup 2005, and Pedroni 2005.)

The first off axis term was derived from first principles and used Fermi Eyges transport theory to determine the root mean square (rms) width of the Gaussian versus depth. Fermi Eyges scattering theory required an input scattering power, T, which is the rate of increase of the mean square multiple Coulomb scattering angle given by

$$T = \frac{d < \theta_{mcs}^2 >}{dx} \tag{11}$$

Gottschalk (2010) has previously shown that the Gaussian approximation to Moliere scattering theory using the differential Moliere scattering power most closely reproduces the full Moliere distribution (within ~3%), which when compared to 39 independent measurements showed a mean deviation of -0.3% with a rms width of 3%. The differential Moliere scattering power is easily calculated on the fly and has been shown by Gottschalk (2010) to be more accurate then what is currently being used in commercially available algorithms that are based on work by Hong (1996) or Soukup (2005). The Hong algorithm uses the Highland formalism and the Soukup algorithm gives the user the option of using the Fermi Rossi, Lynch, or Highland formalism. In his review, Gottschalk (2010) determined the Highland formalism was the most accurate of these three (within ~7% of Moliere) but not as accurate as differential Moliere formalism. This improved accuracy and the ease of implementation was the key motivation to the use of the differential Moliere scattering power.

The differential Moliere scattering power (note the factor of 2 accounts for equation 11 not being the “projected” angle, as was the convention of Gottschalk 2010) is given by

$$T_{dM} = 2 \cdot f_{dM} \cdot \left(\frac{E_s}{pv}\right)^2 \frac{1}{X_s} \tag{12}$$

where Es is the Fermi term and is given by

$$E_s = \left(\frac{2\pi}{\alpha}\right)^{\frac{1}{2}} m_e c^2 \tag{13}$$

X_s is the scattering length, a group of constants from Gottschalk's scattering power derivation, and is given by

$$\frac{1}{X_s} = \rho\alpha N r_e^2 \frac{Z^2}{A}\left\{2\, ln\left(33219(AZ)^{-\frac{1}{3}}\right) - 1\right\} \tag{14}$$

f_{dM} is the single scatter correction term and is given by

$$f_{dM} = 0.5244 + 0.1975\ln\left(1 - \left(\frac{pv}{p_1 v_1}\right)^2\right) + 0.232\ln(pv) - 0.0098\ln(pv)\ln\left(1 - \left(\frac{pv}{p_1 v_1}\right)^2\right) \tag{15}$$

where α is the fine structure constant (7.297 x 10^{-4}), $m_e c^2$ is the rest mass of an electron (0.511 MeV), ρ is the density of the target, N is Avogadro's number (6.022 x 10^{23}), r_e is the classical radius of the electron (2.818 x 10^{-15} m), Z is the atomic number of the target, A is the atomic mass of the target, p is the local momentum of the particle, v is the local velocity of the particle, p_1 is the incident momentum of the particle, and v_1 is the incident velocity of the particle.

The differential Moliere scattering power was implemented into Fermi Eyges scattering theory in the calculation of the i^{th} scattering moments (a_i) given by

$$a_i(Z) = \frac{1}{2}\int_0^Z T_{dM} \cdot (Z - Z')^i dZ' \tag{16}$$

Thus the rms width of Gaussian due to multiple Coulomb scatter is given by

$$\sigma_p(Z) = \sqrt{a_2(Z) =} \sqrt{\frac{1}{2}\int_0^Z T_{dM} \cdot (Z - Z')^2 dZ'} \tag{17}$$

The Z-Z' dependence in Eq. 17 reveals that the rms width is not only a function of depth but is also dependent on scatter events upstream. This dependence is particularly important in dealing with heterogeneities, because scattering is not only locally affected by a heterogeneity but everything down stream is affected as well. This upstream dependence was the key motivation for using Fermi Eyges scattering theory in our PBA. Note that in order to increase

the speed of the dose calculations, equation 17 was evaluated using the recursion relation shown by Hogstrom (1987) where

$$a_2^{i,j} = a_2^{i,j-1} + 2\Delta z\, a_1^{i,j-1} + (\Delta z)^2\, a_0^{i,j-1} + \frac{(\Delta z)^3}{6} T_{dM}\left(E_{i,j}\right)$$

$$a_1^{i,j} = a_1^{i,j-1} + \Delta z\, a_0^{i,j-1} + \frac{(\Delta z)^2}{4} T_{dM}\left(E_{i,j}\right) \qquad (18)$$

$$a_0^{i,j} = a_0^{i,j-1} + \frac{\Delta z}{2} T_{dM}\left(E_{i,j}\right)$$

$$a_2^{i,1} = a_1^{i,1} = a_0^{i,1}, and\ \Delta z = z_j - z_{j-1}.$$

The second term of the off axis component of our PBA was called the nuclear halo term, following the nomenclature by Soukup (2005) and Pedroni (2005). This term was intended to model things in the off axis distribution of protons scattering not modeled by the multiple Coulomb Scatter (MCS) Gaussian core. These other contributions of proton scatter fall off slower further off axis than the Gaussian core. This is due to a combination of events such as single scattering (>θ_{mcs}) or any head on nuclear interaction (>>θ_{mcs}). According to Pedroni (2005), if this is not accounted for errors of 5-10% can occur. The second term was used in conjunction with the primary Gaussian predicted from scattering theory. The width of the second Gaussian was given by the convolution of a nuclear Gaussian of width (σ_N) and the primary Gaussian of width (σ_p). The convolution of these two Gaussians results in a Gaussian of width $\sqrt{\sigma_p^2 + \sigma_N^2}$. The total dose from a pencil beam was then given by a weighted sum of the primary pencil beam and a nuclear pencil beam given by

$$D_i(X,Z) = (1 - W_N(Z))D_\infty(0,Z)F_p + W_N(Z)D_\infty(0,Z)F_N \qquad (19)$$

Where W_N is a weighting factor ($0 \le W_N \le 1$) and thus the dose from a single pencil beam is

$$D_i(X,Z) = (1 - W_N(Z))D_\infty(0,Z) \cdot \int_{x_i - \frac{\Delta x}{2}}^{x_i + \frac{\Delta x}{2}} \frac{1}{\sqrt{2\pi}\sigma_p} \cdot exp\left[\frac{-[(X - x')^2]}{2{\sigma_p}^2}\right] dx'$$

$$+ (W_N(Z))D_\infty(0,Z) \cdot \int_{x_i - \frac{\Delta x}{2}}^{x_i + \frac{\Delta x}{2}} \frac{1}{\sqrt{2\pi\left(\sigma_p^2 + \sigma_N^2\right)}} \cdot exp\left[\frac{-[(X - x')^2]}{2\left(\sigma_p^2 + \sigma_N^2\right)}\right] dx' \qquad (20)$$

Note that W_N, σ_p, and σ_N are depth-dependent parameters. W_N and σ_N were determined from curve fits to cross field profiles from Monte Carlo simulations of proton pencil beam distributions in water. This was done for all the energies used in the PBA (100, 150, 200, and 250 MeV).

To commission the algorithm, Monte Carlo simulations were done for 50, 100, 150, 200, 250 MeV proton beams with 0 .1, 2, 4, 10 cm field sizes. These simulations were used as surrogates for measurements. The Monte Carlo code modeled range straggling and contributions to the depth dose from secondary particles created by nuclear interactions in water. The central axis depth dose, corrected for side scatter equilibrium, was used as input data of the PBA similar to work by Ciangaru (2005). In order to use the central axis depth dose commissioning data for the different field sizes (FS) they must be corrected for side scatter equilibrium. This insured that the depth dose modeled energy loss and the fluence modeled scattering. Methods from Hogstrom (1981) were adapted to do this and the rationale used is as follows.

The central axis dose of a proton beam of field size FS is given by

$$D_{FS}(0,Z) = D_{\infty}(0,Z)F(0,Z) \tag{21}$$

Rearranging, the central dose of an infinitely broad field is

$$D_{\infty}(0,Z) = \frac{D_{FS}(0,Z)}{F(0,Z)} \tag{22}$$

The fluence must be evaluated across the field. For the primary fluence this is given by

$$F_p(0,Z) = \int_{-\frac{FS}{2}}^{\frac{FS}{2}} \frac{1}{\sqrt{2\pi}\sigma_p} \cdot exp\left[\frac{[(x')^2}{2{\sigma_p}^2}\right] dx' = erf\left[\frac{FS}{2\sqrt{2}\sigma_p}\right] \tag{23}$$

Similarly for the nuclear fluence

$$F_N(0,Z) = \int_{-\frac{\mathrm{FS}}{2}}^{\frac{\mathrm{FS}}{2}} \frac{1}{\sqrt{2\pi\left(\sigma_p^2 + \sigma_N^2\right)}} \cdot exp\left[\frac{(x')^2}{2\left(\sigma_p^2 + \sigma_N^2\right)}\right] dx' = erf\left[\frac{FS}{2\sqrt{2\left[\sigma_p^2 + \sigma_N^2\right]}}\right] \tag{24}$$

By substituting the results of equations 23 and 24 and evaluating all the integrals in equation 20 the equation for the dose from the ith pencil beam centered at x_i becomes

$$D_i(X,Z) = \frac{(1 - W_N(Z))D_{FS}(0,Z)}{erf\left[\frac{FS}{2\sqrt{2}\sigma_p^w}\right]} \cdot \left[erf\left[\frac{x_i + \frac{\Delta x}{2} - x}{\sqrt{2}\,\sigma_P}\right] - erf\left[\frac{x_i - \frac{\Delta x}{2} - x}{\sqrt{2}\,\sigma_P}\right]\right]$$

$$+ \frac{(W_N(Z))D_{FS}(0,Z)}{erf\left[\frac{FS}{2\sqrt{2\left[\sigma_p^{w\,2} + \sigma_N^2\right]}}\right]} \cdot \left[erf\left[\frac{x_i + \frac{\Delta x}{2} - x}{\sqrt{2\,[\sigma_P^2 + \sigma_{N1}^2]}}\right] - erf\left[\frac{x_i - \frac{\Delta x}{2} - x}{\sqrt{2\,[\sigma_P^2 + \sigma_{N1}^2]}}\right]\right] \quad (25)$$

For a field consisting of N pencil beams the total dose is given by equation 10, the summation of D_i from i = 1 to N. Note that in the side scatter equilibrium correction term σ_p^w is used to explicitly state that the rms width σ_p^w is determined for an all water phantom. This is necessary because the input data used is measured or simulated in a water phantom. The rms width σ_p^w is used to correct the input data and should not to be confused with the rms width of the primary pencil beam σ_p, which is material dependent.

2.2 Specific Aim 1: Modify the PBA to Account for Heterogeneities.

A pencil beam algorithm splits the dose delivered by a field into smaller contributions called pencil beams. The dose from a pencil beam is split into two terms: the central axis term and the off axis term. In order to correctly account for heterogeneities both of these terms must account for changes in material. Before discussing how each term was modified to account for different materials some other details on how the algorithm works must be discussed.

2.2.1 Dose Calculation Grid and Ray Trace

To start every calculation, the x-z plane was divided into a 1 x 1 mm^2 grid. Each pixel was assigned a CT number corresponding to a different material (similar to a treatment planning system). The CT number of a material is the scaled relative difference between the linear attenuation of a material to that of water: It is dependent on the energy of the CT scan. The CT number of a material is generally given in Hounsfield units, with water having a CT number of 0,

air having a value of -1000, and hard bone having a value of approximately +600. Since this work examined only stylized geometries, pixels were simply created in MATLAB using arbitrary reference CT numbers. The stopping powers and elemental compositions of all the different materials used in this study were stored in look up tables.

After the material composition and stopping power of each pixel was defined and the incident energy of the proton beam was selected, a ray trace was performed to determine the energy loss in each pixel. In this work, all the protons incident on a given pixel are traveling in an orthogonal direction relative to the edge of the pixel, therefore the energy $E(Z_i)$ of the beam entering each pixel at a depth Z_i was determined from the energy of the beam entering the previous pixel $E(Z_{i-1})$, stopping power (dE/dZ) of the previous pixel located at Z_{i-1}, and the pixel thickness (ΔZ):

$$E(Z_i) = E(Z_{i-1}) - \left[\left(\frac{dE}{dZ}\right)_{material}\right]_{E(Z_{i-1})} \cdot \Delta Z \tag{26}$$

Where $\left[\left(\frac{dE}{dZ}\right)_{material}\right]_{E(Z_{i-1})}$ is the stopping power for the material from Z_{i-1} to Z_i at energy $E(Z_{i-1})$.

The materials used were air, compact bone, and water. The stopping powers tabulated by Berger et al (2005) were used for all of these materials and were accessed on the PSTAR database located at http://physics.nist.gov/PhysRefData/Star/Text/PSTAR.html. All stopping powers were recorded with a 0.5 MeV energy step from 300 MeV to .5 MeV for Water, Air, and Compact Bone.

The water equivalent depth or effective depth (Z_{eff}) for each pixel was also calculated and stored, where Z_{eff} is the depth in water that would produce the same energy loss as a given pixel at depth Z_i and was calculated by:

$$Z_{eff}(Z_i) = Z_{eff}(Z_{i-1}) + \Delta Z \cdot \left[\left[\frac{dE}{dZ}\right]_{water}^{material}\right]_{E(Z_{i-1})} \tag{27}$$

Where $\left[\left[\frac{dE}{dZ}\right]_{water}^{material}\right]_{E(Z_{i-1})}$ is the ratio of the stopping power for the material from z_i to z_{i-1} to that of water at $E(z_{i-1})$.

Once the proton energy, effective depth, and stopping power were determined for all the pixels, the effects of heterogeneities on the central and off axis terms in the pencil beam calculation could be accounted for.

2.2.2 Central Axis Term

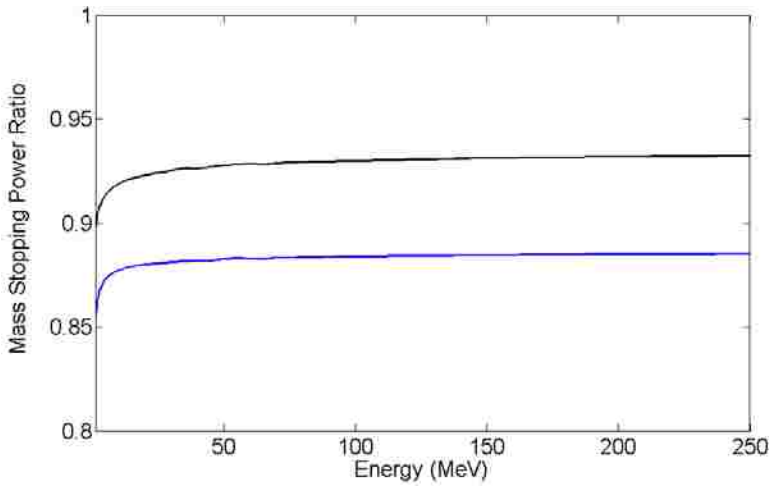

Figure 2.1: The mass stopping power ratios relative to water of compact bone (black) and air (blue) plotted against proton energy. Data from Berger (2005).

To account for differences in energy deposition due to the presence of heterogeneities, the central axis term, which was determined in water at Z_{eff}, was scaled by the ratio of mass stopping powers in a material to that of water. The mass stopping power of a material is the stopping power (dE/dZ) divided by the density of a material (ρ). Thus equation 28 gives the central axis dose accounting for changes in material in depth. The ratio of mass stopping powers of compact bone and air relative to water are plotted in Figure 2.1.

$$D(0,Z)_{material} = D(0,Z_{eff})_{water} \cdot \left[\frac{1}{\rho}\frac{dE}{dZ}\right]_{water}^{material} \quad (28)$$

2.2.3 Off Axis Term

The PBA fluence consisted of a primary term along with a nuclear halo term to describe the off axis distribution of a pencil beam with depth. No corrections to the nuclear halo fluence terms were done to account for heterogeneities.

The primary term utilized the differential Moliere scattering power within the Fermi-Eyges scattering theory formalism to determine the spread of each pencil beam with depth. Within the differential Moliere scattering power equation shown in equation 12 is a material-dependent term called the scattering length given in equation 14. The calculation of scattering length for compounds follows the Bragg additivity rule

$$\frac{1}{\rho X_s} = \sum_i w_i \left(\frac{1}{\rho X_s}\right)_i, \tag{29}$$

where the weight fraction of a certain element i in the compound is given by w_i. The scattering length was calculated for air, water, and compact bone for this work using the chemical compositions shown in Table 2.1

Table 2.1: Chemical compositions used in this study.

Compounds	**Density ρ (g/cm^3)**	**Elemental Make Up By Atomic Number**	**Weight By Fraction w_i**
Water	1	1 8	0.111907 0 .888093
Air	.0012	6 7 8 18	0.000125 0.755267 0.231781 0.012827
Compact Bone	1.85	1 6 7 8 12 15 16 20	0.06000 0.31400 0.03100 0.36900 0.00100 0.07000 0.00200 0.15200

2.3 Specific Aim 2: Improving the Nuclear Model

2.3.1 Preliminary Results Suggest a Deficiency and a Proposed Solution

While the PBA model of Chapman (2012), which included a Gaussian halo model, showed greater than 99% of points were within 2 percent or 1 mm distance to agreement, there was evidence of sub-optimal modeling in low dose regions. In these regions, the prediction of dose was dominated by the secondary nuclear halo term. Small inaccuracies in the halo term modeling low dose regions of a pencil beam will be amplified as many pencil beams are summed up. For example, in Figure 2.1 in the low dose low gradient region near the field edges at X= ± 2cm there were failing pixels. The PBA underestimates the dose outside of X= ± 2cm for all depths. Even though these errors are relatively insignificant in a monoenergetic 4 x 4 cm^2 field, they can be very import when modeling pencil beam scanning modalities with numerous spots.

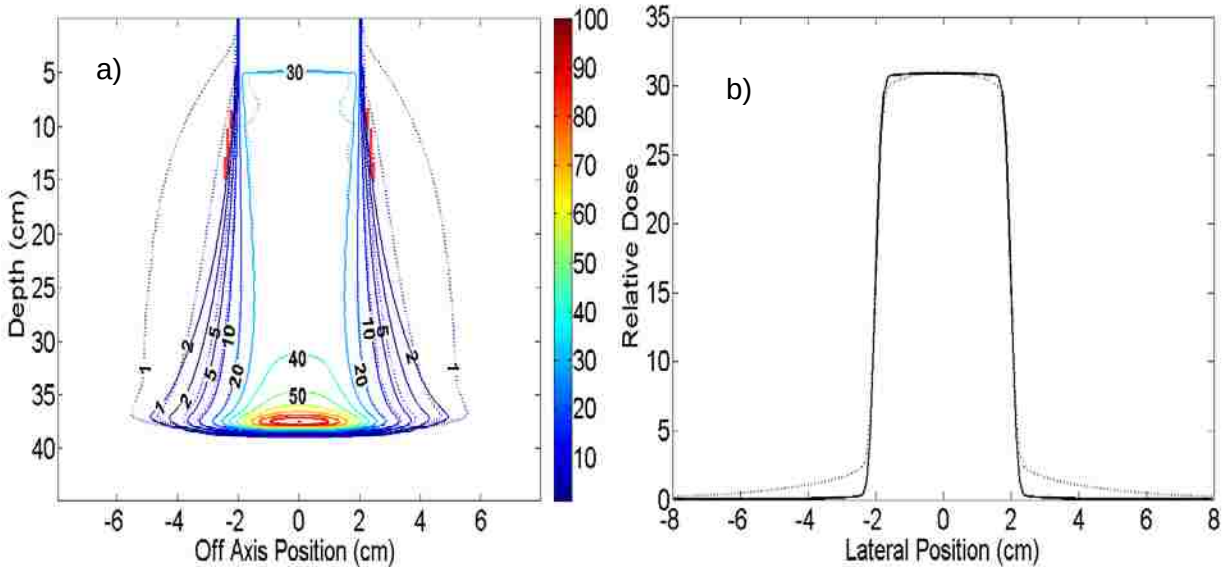

Figure 2.2: 250 MeV 4x4 cm^2 proton beam incident on a water phantom. a) 2D dose distribution contour: Monte Carlo data (dashed lines) and PBA data (solid lines) using Chapman's model (Chapman 2011). The color bar indicates relative dose percentage. Note the PBA underestimates the 1 and 2 percent isodose lines. b) Lateral profile at a depth of Z = 12.55 cm, where the Monte Carlo data (dashed) falls off slower than the PBA (solid) in the low dose regions near the field edge.

To better understand the dose component in this region of interest, a 4 x 4 cm^2 proton beam was simulated with and without including the dose from secondary protons. As shown in Figure 2.2, secondary protons scattered at large angles were responsible for this low dose region outside the field edge (5%-1% isodose). When the dose from the secondary protons was not included the low dose regions outside of field edge were greatly reduced and resembled the PBA data. The dose delivered from just the secondary protons falls off much slower than an erf function (integration of a Gaussian pencil beam) as seen in Figure 2.3 and could not be properly modeled using the Gaussian nuclear halo model (Chapman 2012).

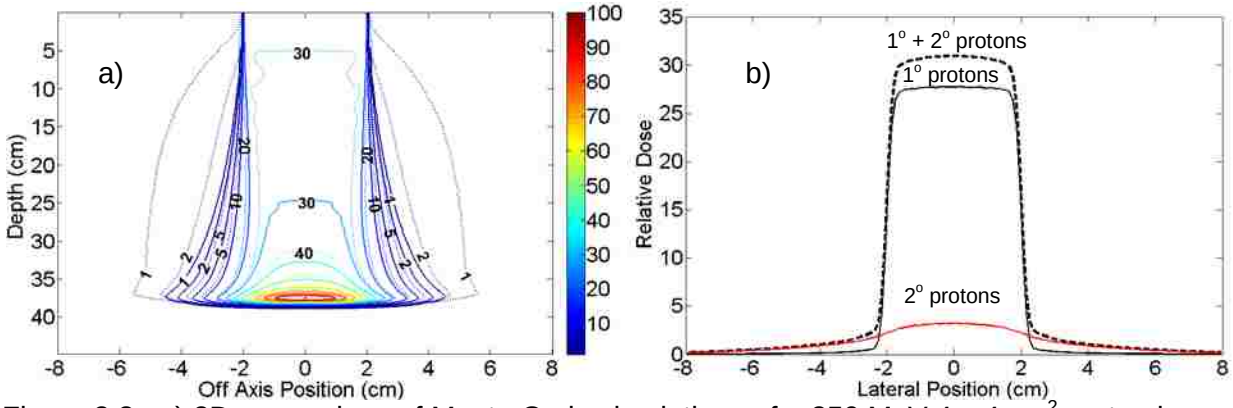

Figure 2.3: a) 2D comparison of Monte Carlo simulations of a 250 MeV 4 x 4 cm^2 proton beam incident on a water phantom with (dashed lines) and without (solid lines) tracking energy deposition from secondary protons. Figure b) Lateral profile recorded at Z = 12.55 cm. A reduction of dose beyond the field edge is evident when energy deposited from secondary protons was excluded. The difference (red line) in the two curves is the secondary proton dose component.

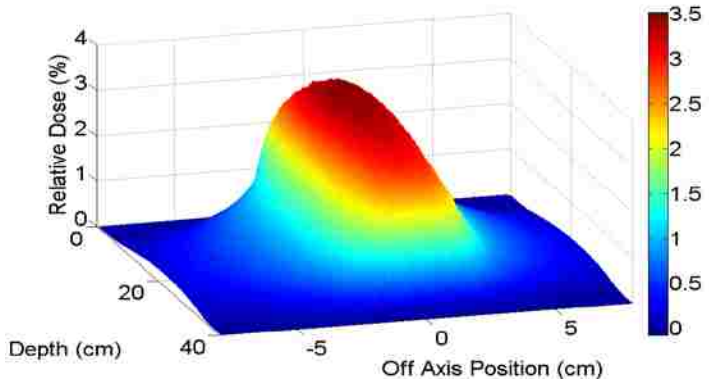

Figure 2.4: 3D surface plot of the relative dose delivered by secondary protons from a 250 MeV 4x4 cm^2 proton beam in a water phantom. Dose was normalized to the maximum dose in water from both primary and secondary protons. The primary Gaussian calculated from scattering theory will not predict the off axis dose from secondary particles as they fall of much slower than a Gaussian off axis.

To better understand the halo model, properties of a pencil beam were studied. Comparison of the PBA and simulated dose distributions of a 1x1 mm^2 pencil beam in water, for which PBA fit parameters were derived also indicated suboptimal agreement in the low dose region outside of the 0.25% isodose contour. From Figure 2.4 one can see after the 0.25% isodose line the model under predicts the dose compared to the Monte Carlo data. When summing up many pencil beams this error compounds leading to the regions of failure present in Figure 2.1 and generally poor agreement in low dose regions (≤10% isodose) near and past the field edge.

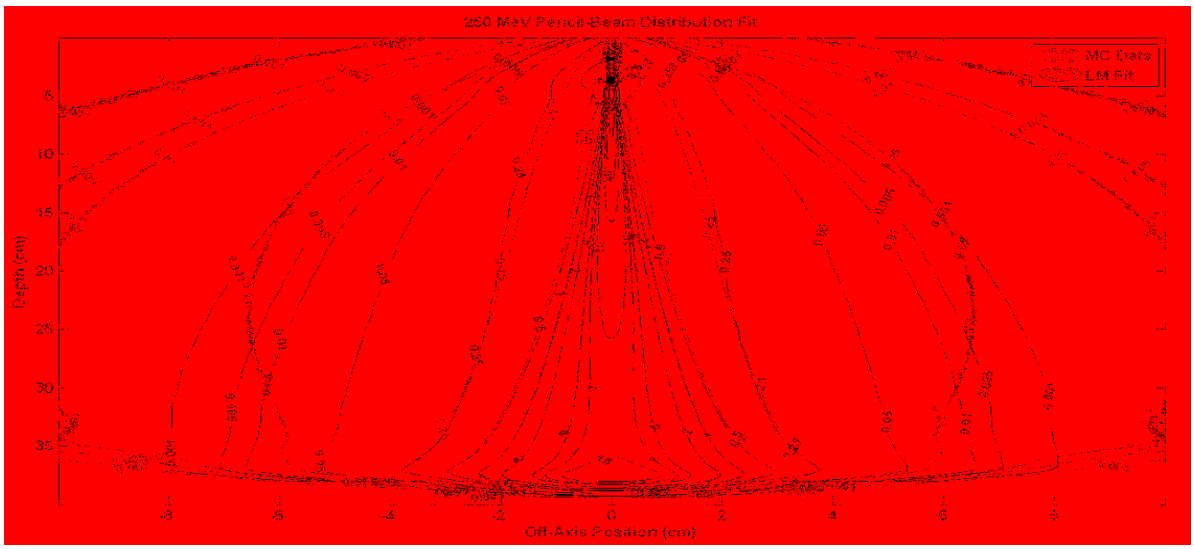

Figure 2.5: 250 MeV 1 x 1 mm^2 proton pencil beam dose distribution in water. MC (blue lines) data and curve fit (black) data using the calculated primary Gaussian and fitted second Gaussian. It is clear that model under-predicts the low dose (≤0.25% isodose) region.

A cross field profile through the distribution in Figure 2.4 at a depth of 12.49 cm is shown in Figure 2.6. The primary and halo components are shown separately. From examining the fit, the result was good agreement in the high dose and transitional regions but an underestimation in the low dose region as seen in Figure 2.6. This indicated the model was accounting for MCS and single scatter events but failing to account for the very large angle scattering from non-elastic interactions. An additional Cauchy-Lorentz term was added to the halo term. The Cauchy-Lorentz distribution centered at x=0 is shown in Figure 2.7 and is given by

$$P(x) = \frac{1}{\pi}\frac{\sigma}{x^2 + \sigma^2} \tag{30}$$

It was chosen because at large distances off axis, it falls off slower than a Gaussian and is integrable in closed form. This additional term allowed the algorithm to improve matching in the low dose region, while continuing to match in the primary high dose region and the transition region while (Figure 2.7).

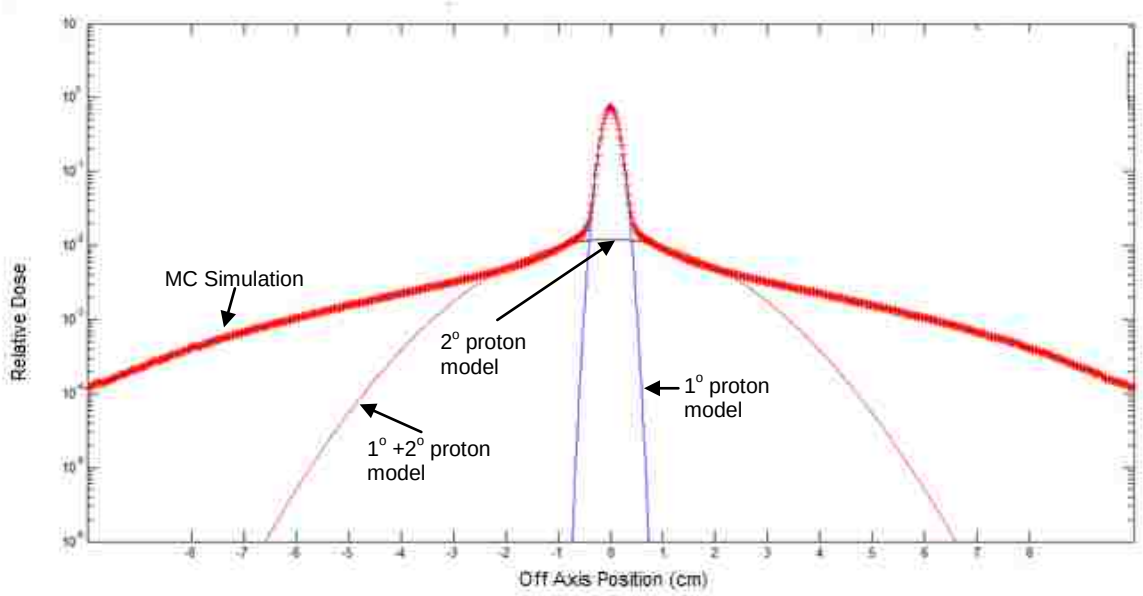

Figure 2.6: Cross field profile at a depth of 12.49 cm of a 250 MeV 1 x 1 mm^2 proton pencil beam dose distribution in water. The Monte Carlo data (red crosses) is plotted with the curve fit (solid red). One can see the individual components of the fit: the primary Gaussian plotted in blue and the secondary plotted in black. Most of secondary Gaussian is covered up by the total curve fit in solid red. However it is clear the fit is failing to match the data at large distances off axis. In the central region (-2 to 2 cm) there is good agreement and the curve fit (solid red) is obscured by the data (red crosses). The data displayed is from Chapman (2012).

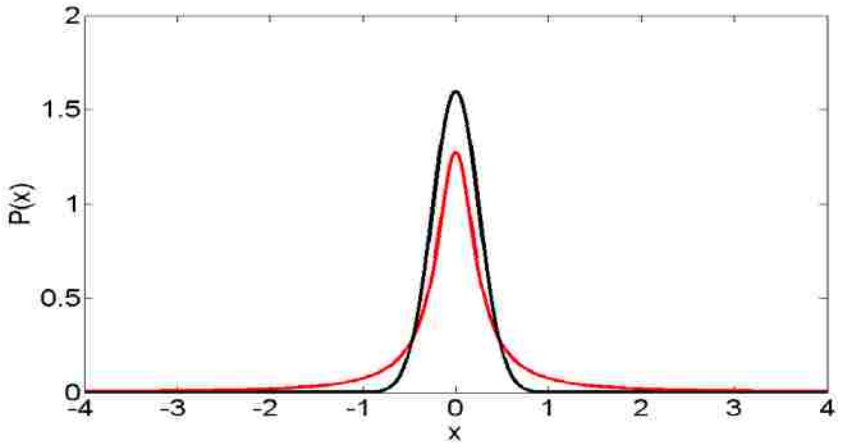

Figure 2.7: Cauchy-Lorentz (red) and Gaussian (black) probability distributions graphed as a function of x. Each distribution is normalized to have unit area with σ = 0.25. At approximately x≥ ±0.5 the Cauchy Lorentz distribution decreases at a slower rate than the Gaussian distribution.

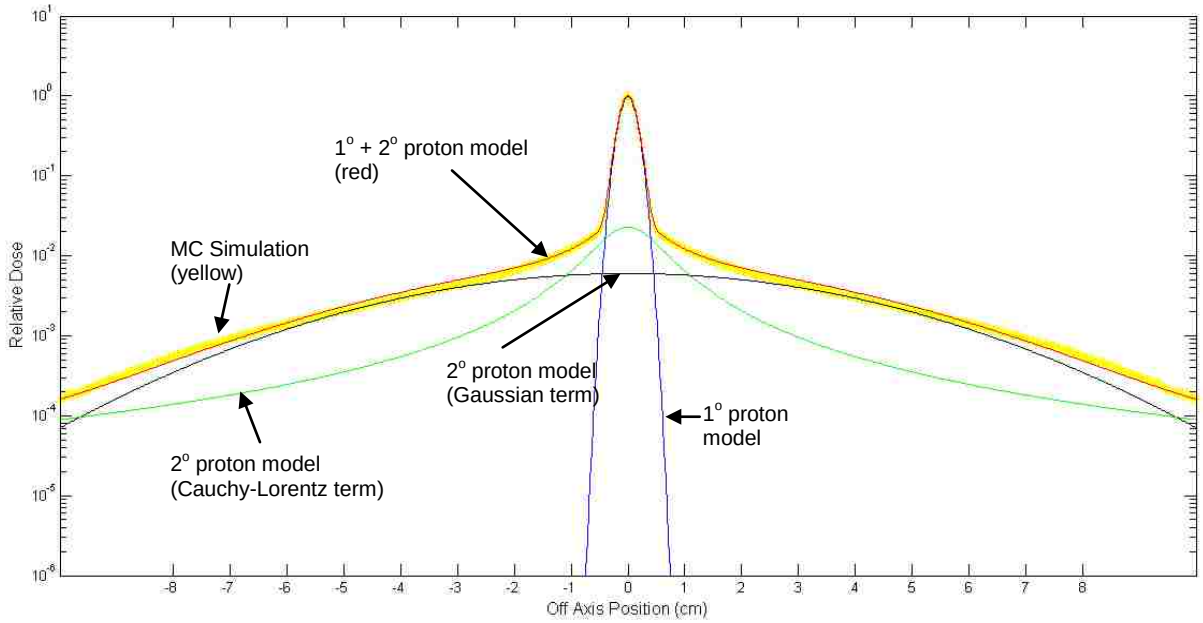

Figure 2.8: The same cross field profile as in Figure 2.6. However the Cauchy Lorentz term (solid green) was used in conjunction with the calculated primary term (solid blue) and a second Gaussian (solid black). The curve fit (solid red) gave much better agreement with the Monte Carlo data (yellow crosses).

2.3.2 Implementation of the Cauchy Lorentz Distribution in the PBA

The Cauchy Lorentz distribution was used in combination with the primary and secondary Gaussians and was fit to the simulated 250 MeV 1 x 1 mm^2 proton pencil beam dose distribution in water. The implementation of the Cauchy Lorentz distribution was accomplished by the following. The dose from a pencil beam was modeled using three terms instead of two. The primary dose D_p, the first halo term D_{N1}, and the secondary halo term D_{N2}.

$$D(X,Z) = D_P(X,Z) + D_{N1}(X,Z) + D_{N2}(X,Z) \tag{31}$$

D_{N2} is the dose from the Cauchy Lorentz term and for a single pencil beam centered at x_i is

$$D_{N2}(X,Z) = D_\infty(0,Z) \cdot W_{N2}(Z) \int_{x_i-\frac{\Delta x}{2}}^{x_i+\frac{\Delta x}{2}} \frac{1}{\pi} \frac{\sigma_{N2}}{((X-x')^2+\sigma_{N2}^2)} dx' \tag{32}$$

By substitution of u= X-x' the integral is evaluated

$$D_{N2}(X,Z) = D_\infty(0,Z) \cdot \frac{W_{N2}(Z)}{\pi} \cdot \left[\tan^{-1}\left[\frac{x_i+\frac{\Delta x}{2}-X}{\sigma_{N2}}\right] - \tan^{-1}\left[\frac{x_i-\frac{\Delta x}{2}-X}{\sigma_{N2}}\right]\right] \tag{33}$$

Equation 33 can be modified to use the central axis depth dose commissioning data for different field sizes (D_{FS}) instead of the depth dose of an infinitely broad beam D_∞ by substituting equation 33 into equation 22 and solving for

$$D_\infty(0,Z) = \frac{D_{FS}(0,Z)}{\frac{2}{\pi}\tan^{-1}\left[\frac{FS}{2\sigma_{N2}}\right]} \tag{34}$$

By substituting these results back into equations 31 and 33, the total dose from N pencil beams in a proton beam of field size FS is

$$\begin{aligned} D(X,Z) = {} & \frac{(1 - W_{N1}(Z) - W_{N2}(Z))}{2} \cdot \frac{D_{FS}(0,Z)}{erf\left[\frac{FS}{2\sqrt{2}\,\sigma_p^w}\right]} \cdot \sum_{i=1}^{N} erf\left[\frac{x_i + \frac{\Delta x}{2} - X}{\sqrt{2}\,\sigma_P}\right] - erf\left[\frac{x_i - \frac{\Delta x}{2} - X}{\sqrt{2}\,\sigma_P}\right] \\ & + \frac{W_{N1}(Z)}{2} \cdot \frac{D_{FS}(0,Z)}{erf\left[\frac{FS}{2\sqrt{2\left[\sigma_p^{w2} + \sigma_{N1}^2\right]}}\right]} \cdot \sum_{i=1}^{N} erf\left[\frac{x_i + \frac{\Delta x}{2} - X}{\sqrt{2\,[\sigma_P^2 + \sigma_{N1}^2]}}\right] - erf\left[\frac{x_i - \frac{\Delta x}{2} - X}{\sqrt{2\,[\sigma_P^2 + \sigma_{N1}^2]}}\right] \\ & + \frac{W_{N2}(Z)}{\pi} \cdot \frac{D_{FS}(0,Z)}{\frac{2}{\pi}\tan^{-1}\left[\frac{FS}{2\sigma_{N2}}\right]} \cdot \sum_{i=1}^{N} \left[\tan^{-1}\left[\frac{x_i + \frac{\Delta x}{2} - X}{\sigma_{N2}}\right] - \tan^{-1}\left[\frac{x_i - \frac{\Delta x}{2} - X}{\sigma_{N2}}\right]\right] \end{aligned} \tag{35}$$

Where W_{N1}, W_{N2}, σ_{N1}, and σ_{N2} as a function of depth in water (Z) are found from curve fits of Monte Carlo data from a simulation of a 1 x 1 mm^2 pencil beam in water and σ_p is calculated from scattering theory using equation 17.

2.3.3 Curve Fitting

With the implementation complete, a curve fitting process was done to commission the new nuclear halo terms: W_{N1}, W_{N2}, σ_{N1}, and σ_{N2}. For all proton energies used in this study, the Monte Carlo data from simulations of a 1 x 1 mm^2 pencil beam in water was fit to determine the halo terms. The Monte Carlo data was calculated using a 0.25 x 0.25 mm^2 grid spacing and covered several centimeters past the range and ±10 cm off axis. The simulations were run with 500 x 10^6 incident particles. The PBA dose equation (Eq. 35) was fit to the Monte Carlo data at

depths and W_{N1}, W_{N2}, σ_{N1}, and σ_{N2} were written to a text file. At a given depth, a non-linear least squares fit was completed and reviewed visually. The halo parameters were at times adjusted manually to improve visual agreement with high dose regions given more importance over lower dose regions. The curve fits were performed every 2.5 cm in depth, or every 100 pixels, for the first 75% of the range. For the remaining portion of the range, the fits were performed every 0.625 cm or every 25 pixels. Linear interpolation was used to find the halo parameters between these depths.

2.4 Specific Aim 3: Evaluate the Dosimetric Accuracy of the PBA

To evaluate the accuracy of the PBA, both Monte Carlo and PBA dose calculations were performed for water phantoms both without and with air and compact bone heterogeneities on a 1 mm x 1 mm grid. The points in the distributions greater than 1% dose were compared using a dose difference and distance to agreement criteria of 2% or 1 mm. The percentage of pixels passing the criteria was used as a metric for the accuracy of the PBA. Comparisons were conducted for four energies (100, 150, 200, and 250 MeV) and two field sizes (4 x 4 cm^2 and 10 x 10 cm^2).

The PBA was written in MATLAB and ran on a single processor. The HPC cluster Philip at Louisiana State University was used to complete the PBA calculations. Using Philip, multiple jobs were able to run simultaneously, taking on average between 30 minutes to 6 hours to complete depending on the incident proton energy. Long calculation times were the result of nested loops with files being read in and then interpolated. Matlab is not optimized for these styles of operations. Calculation speed was not a concern during this work; however computational optimization of the code can be completed to decrease computation times. For instance, current versions of code implemented in C have calculation times on the order of approximately 10-15 seconds.

2.4.1 Test Geometries

Three types of test geometries were used: homogeneous phantoms, phantoms containing laterally infinite slabs, and phantoms containing laterally finite slabs (Figure 2.9). Homogenous phantoms of compact bone and water phantoms, and laterally infinite and finite slabs containing air and compact bone at different depths in a water phantom were examined. Approximately 140 test dose calculations were performed with 30 different geometries, 4 proton energies, and two field sizes (Table 2.2).

Table 2.2: Test geometries used in this work. The dose from a 4 x 4 and 10 x 10 cm^2 was calculated for each of these geometries.

Depth of Slabs (cm)				
Proton Energy (MeV)	100	150	200	250
Homogenous Water	N/A	N/A	N/A	N/A
Homogenous Bone	N/A	N/A	N/A	N/A
Laterally Infinite Slabs				
2 cm Air	2	2,5	2,5,10,15	2,5,10,15,30
5 cm Air	0	0,10	0,10,15	0,10,15,25,30
2 cm Bone	2	2	2	2,30
5 cm Bone	0	0	0	0,30
Laterally Finite Slabs				
2 cm Air	0	0,10	0,10,15	0,10,15,25,30
2 cm Bone	2,5	2,5,10	2,5,10,15	2,5,10,15,30

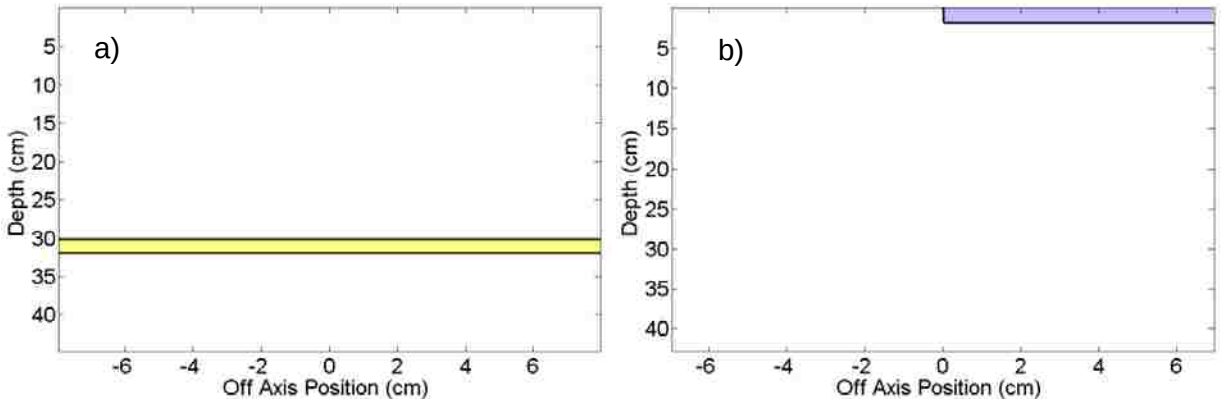

Figure 2.9: Example geometries: a) A laterally infinite 2 cm thick bone slab at 30 cm depth (yellow) in a water phantom. b) A laterally finite 2 cm thick air slab located at 0 cm depth (blue) inside a water phantom.

2.4.2 Monte Carlo Simulations

All Monte Carlo simulations utilized Monte Carlo N-Particle eXtended (version 2.7a, Los Alamos, NM), which is a general purpose code capable of transporting charge particles, neutrons, photons. MCNPX has shown great utility and accuracy in proton therapy applications (Zheng 2007, Herault 2007, and Newhauser 2005). The proton source was modeled as a parallel, monoenergetic source of uniform intensity. Energies of 100, 150, 200, and 250 MeV were used with field sizes of 4 x 4 cm^2 and 10 x10 cm^2. Energy deposition from any particle per volume (MeV/ cm^3) in a given voxel was tallied using a type 3 mesh tally and then divided by the density of the voxel to find absorbed dose (MeV/g). Mesh tallies bins were placed such that the edge of the tally grid began at the surface of the water phantom. For simulations containing air slabs these tallies had to be shifted laterally and downstream by half of a tally to accommodate correct transport along the edges of the slabs. The tally dimensions in X, Y, and Z were 1 mm, 20 cm, and 1 mm respectively.

Only protons (primary and secondary) were transported; dose deposited from all other particles was deposited locally. Following protons, neutrons are the second most abundant secondary particles and do not deposit energy locally, accounting for a total dose of approximately 0.3% of the prescription dose (Taddei 2008). To confirm that this error was insignificant, Monte Carlo simulations were performed to determine the dose delivered by all other particles (neutrons, photons, alphas, deuterons, and other heavy ions) besides protons if assumed to be deposited locally (Figure 2.9a). At 250 MeV, the maximum dose delivered from particles assumed to be deposited locally was 0.38% of the maximum dose from all particles and was at most 1.25% of the local dose value. The difference in dose transporting neutrons and photons versus assuming local deposition was very small (<0.2% of the maximum dose) and can be seen in Figure 2.9b. This error is further reduced for the lower energies due to the reduced number of neutrons and photons produced.

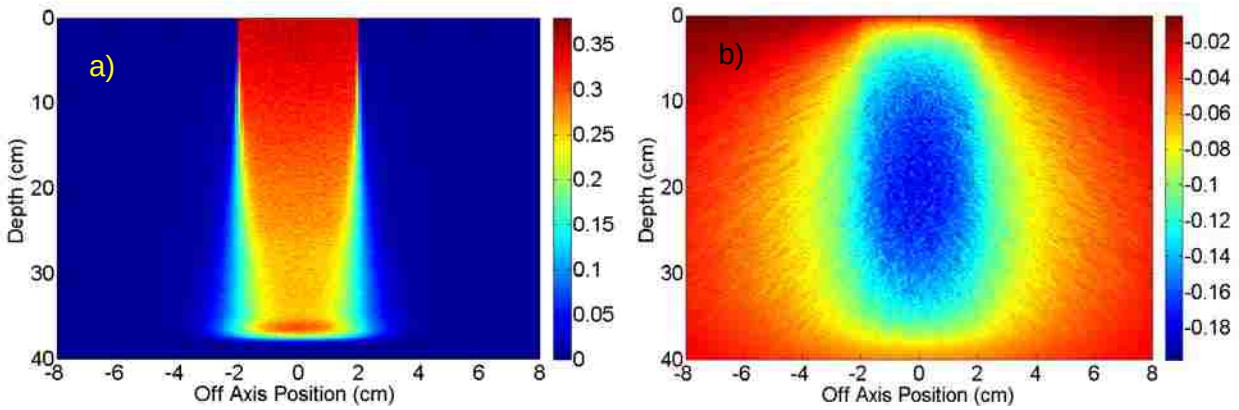

Figure 2.10: a) 2D dose distribution of dose delivered by all secondary particles other than secondary protons assumed to be deposited locally form a 250 MeV 4 x4 cm^2 proton field incident of water. b) 2D dose difference distribution for the same field. The dose (%) is displayed in the color bar and is normalized to the maximum dose delivered in water by all particles. The maximum dose was 0.38% of the maximum dose delivered by all particles in water. Neutrons and photons produce a fraction of this dose and will carry it out of the field as illustrated in b). The dose distribution was simulated assuming photons and neutrons are deposited locally and then subtracted from the same distribution with neutrons and photons being transported. One will note the loss of dose in the field from neutrons and photons transported out of the field. This effect was at most a 0.2% reduction in dose relative to the maximum dose.

MCNPX uses a combination of tabular data and the Bertini intranuclear cascade model for modeling non-elastic interactions, including creation and transport of secondary protons (MCPNX 2011). MCNPX models energy loss using stopping powers along with a correction for energy straggling. Stopping power tables are discretely sampled over a range between the maximum energy and a cut off energy set by the user. In this study the maximum energy was set to the incident energy of proton and the cut off energy was set to 1 MeV. The energy interval that the sampling stopping powers are sampled from is equal to 91.7% of the energy at the current step. Thus the end of range has much finer energy resolution. MCNPX accounts for range strangling by using the Valivov model for charge particle straggling (MCNPX 2011).

In MCNPX as the protons are transported through the energy grid there are a number of sub steps per energy step. The energy loss and distance traveled are estimated and range straggling and multiple Coulomb scattering distributions are sampled from at each sub step. The type of material determines the number of sub steps, with low Z materials having less sub steps than high Z materials. The default number of sub steps was used in all simulations.

All Monte Carlo simulations were run in parallel on the High Performance Computing (HPC) cluster Tezpur at Louisiana State University. The simulations were run with the appropriate number of histories such that the statistical uncertainty was under 1% for all dose points. This varied depending on the incident energy, field size, and tally size but was generally between 50 x 10^6 and 200 x 10^6 histories. The time to complete simulations varied widely. A short job, such as 100 MeV 4 x 4 cm^2 proton beam incident on a compact bone phantom, took approximately 10 minutes on 64 processors. For longer jobs, such as the ones used to find the nuclear halo parameters, the computation time was much longer. For instance, a 250 MeV 1 x 1 mm^2 proton beam incident on a water phantom with dose being recorded on a 0.25 x 0.25 mm^2 grid over 40 cm in depth and from -10 to 10 cm laterally took 72 hours running on 128 processors.

2.4.3 Comparison Metrics

PBA and Monte Carlo dose distributions were compared following the methodology used by Chapman (2012), where all dose points calculated from a proton beam of a field size were normalized to the maximum dose delivered in a flat water phantom from a proton beam of the same field size. The Monte Carlo dose grid was cropped and/or interpolated to match the PBA dose grid. The dose difference at each point was then taken as the Monte Carlo dose was subtracted from the PBA dose.

Distance to agreement (DTA) was calculated using a routine written by Mancuso (2011) that was adapted from work by Ju et al (2008), whereby each point in the PBA matrix was compared to the same point in the Monte Carlo matrix. If the values were equal, the DTA was zero. Otherwise the DTA was taken as the shortest distance from the point to a contour of the Monte Carlo dose value. Only pixels having Monte Carlo dose points greater than 1% of the maximum dose in a flat water phantom were compared. Pixels showing either less than 2% dose difference or 1 mm DTA were taken as passing criteria.

Chapter 3: Results and Discussion

3.1 Improved Nuclear Halo Model

3.1.1 Curve Fit Results

Figure 3.1 shows the 250 MeV 1 x 1 mm^2 cross-field profiles of the curve fit results at four different depths. Figure 3.2 shows the full 2D distribution comparison between PBA using the curve fit parameters and Monte Carlo. After including the Cauchy Lorentz term, the PBA showed improved dosimetric agreement with Monte Carlo over the previous version (Figure 2.6).

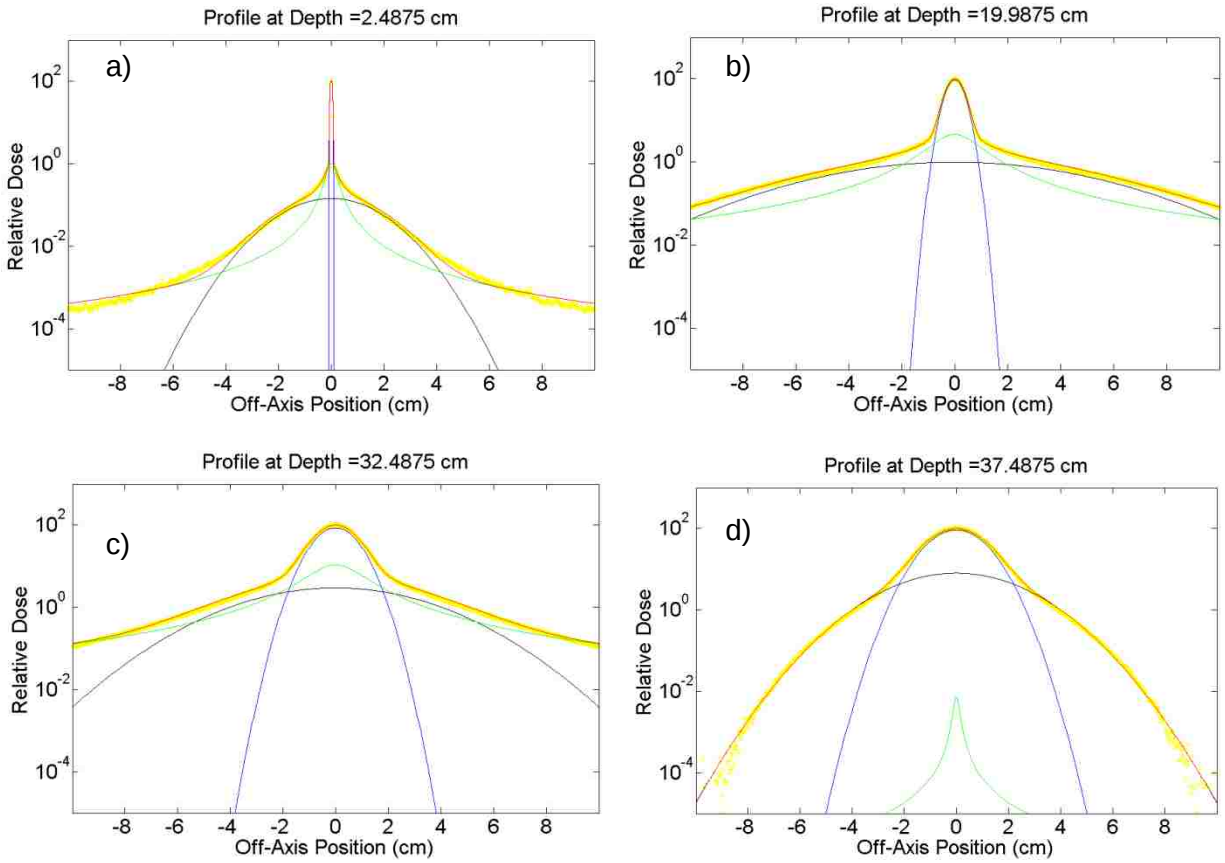

Figure 3.1: Representative cross-field profiles used in the curve fitting process for the 250 MeV proton data. The Monte Carlo data (yellow markers) is plotted along with the curve fit (red line). The individual components of the fit can be seen as well, the primary Gaussian (blue), secondary Gaussian (black), and the Cauchy Lorentz (green). Improved agreement was noted in the low-dose off-axis regions relative to the previous version of the PBA (Chapman 2012).

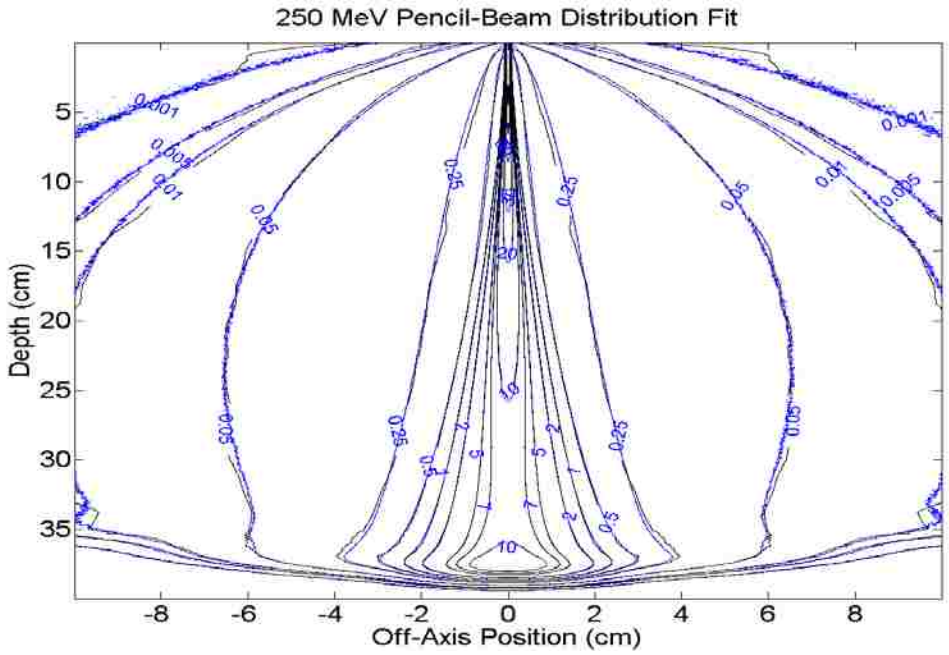

Figure 3.2: 2D distribution of the 250 MeV 1 x 1 mm^2 pencil beam. The Monte Carlo data (blue) is plotted with the curve fit (black).

Figure 3.3 show cross field profiles at two different depths for a 150 and 200 MeV 1 x 1 mm^2 beam. There was a very sharp drop off in dose in the low dose region of the Monte Carlo data. This could not be modeled due to the structure of the Cauchy Lorentz distribution (parameterization, not physically based), however since this occurred far off axis in the very low dose region it should not be a significant error. This error would also have been seen in the 250 MeV data if the dose grid extended further off axis.

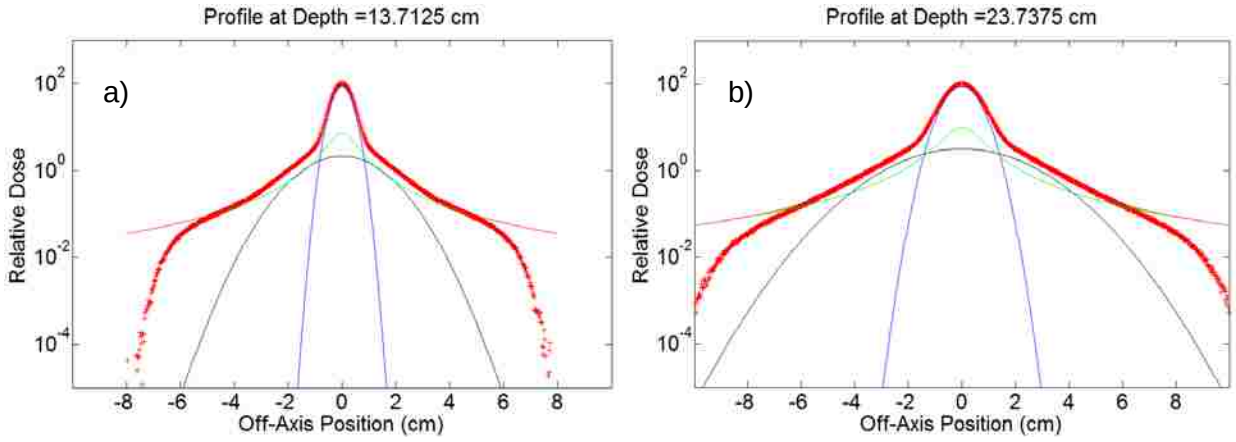

Figure 3.3: Representative cross field profiles used in the curve fitting process for the (a) 150 and (b) 200 MeV proton data. Note the sharp lateral fall off not being modeled by the fit. However this shouldn't have a significant effect on overall pencil beam dose calculation.

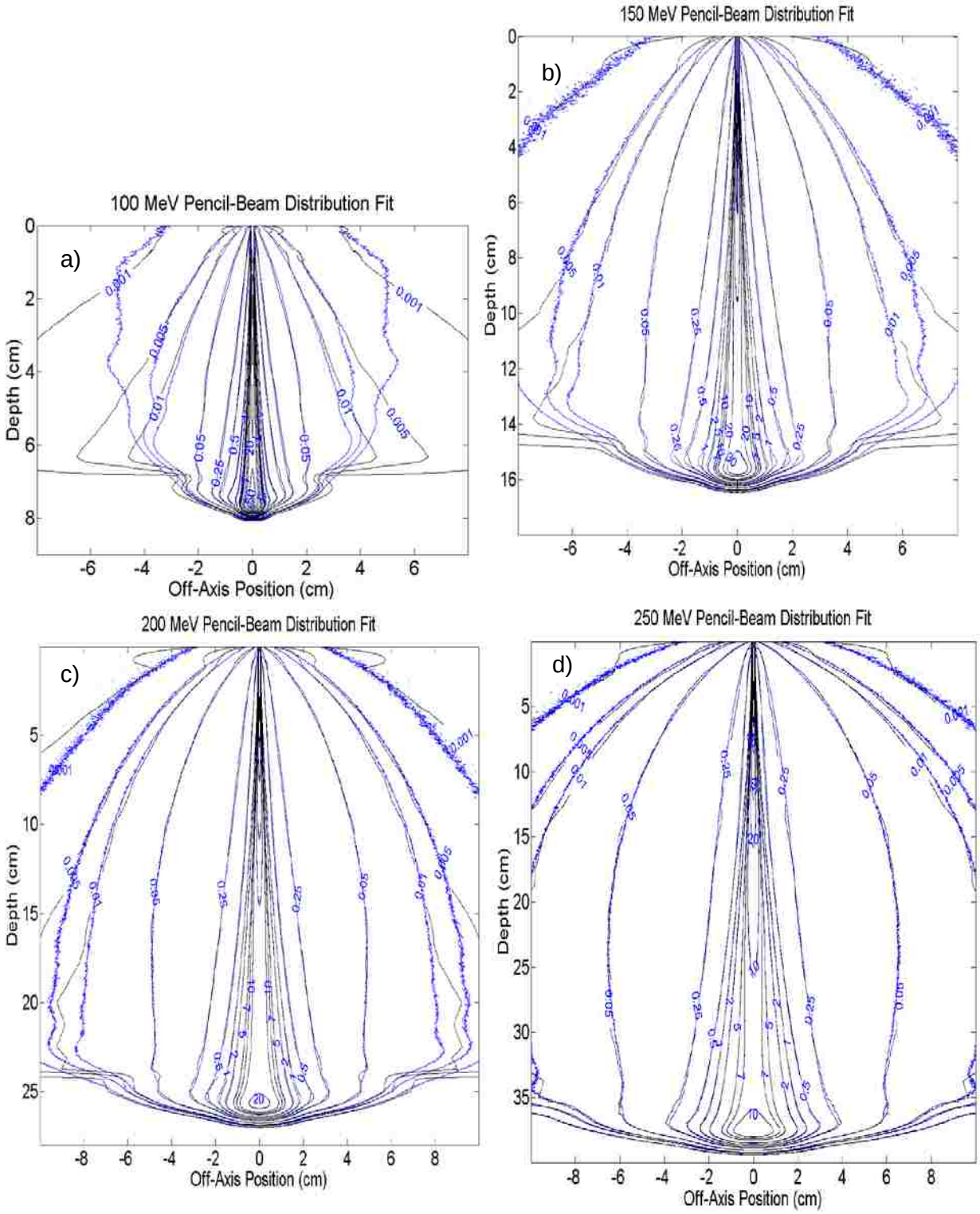

Figure 3.4: 2D distributions of the 100 (a), 150 (b), 200 (c), and 250 (d) MeV 1 x 1 mm^2 pencil beam distribution. Monte Carlo data (blue) is plotted with the PBA (black). The deviation at very low isodose lines off axis is apparent in figures a), b), and c) but should have insignificant effect on the overall dose calculation.

Figure 3.4 shows 2D distributions constructed after determining all of the halo parameters as a function of the depth for all four energies used. It is visually apparent the new three term fit improved agreement over all regions of the pencil beam dose distributions for all energies compared to the two term fit. The fit parameters (W_{N1}, W_{N2}, σ_{N1}, and σ_{N2}), i.e. the relative weights and widths of the two halo distributions, as a function of depth in water are shown in Figure 3.5.

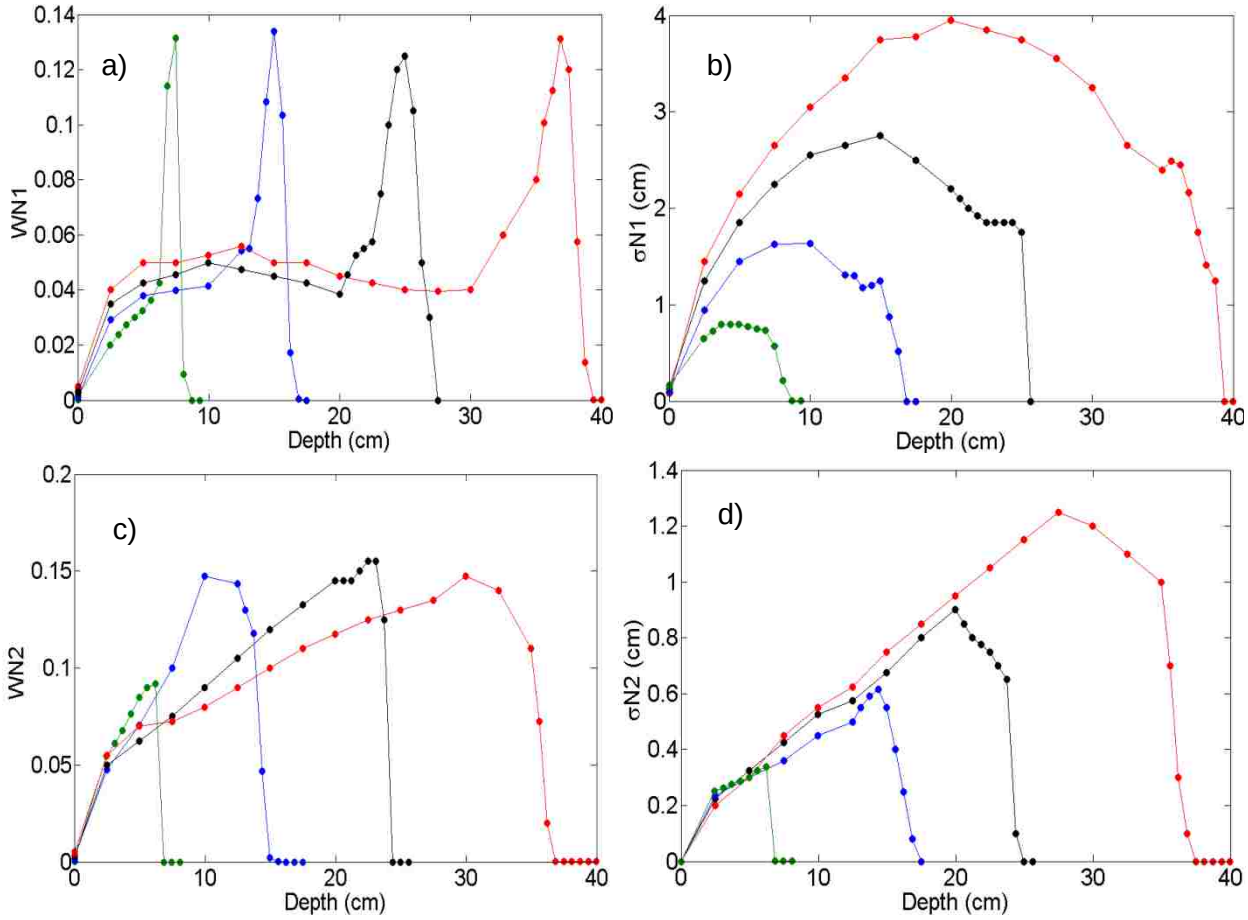

Figure 3.5: Fitted halo parameters as a function of depth plotted for each energy (100 MeV in green, 150 MeV in blue, 200 MeV in black, and 250 MeV in red): a) The weighting factor WN1, b) the rms width of the second Gaussian σ_{N1}, c) the weighting factor of the Cauchy Lorentz WN2, and d) The σ_{N2} value of the Cauchy Lorentz distribution. (note that σ_{N2} is not the rms width; it is the half width at half maximum). The depths where a fit was completed are designated with markers. For depths in between these points linear interpolation was used.

One disadvantage of the curve fit method used in this work was that the two nuclear terms were an entirely empirical correction used to model single scatter, inelastic, and non elastic nuclear events, which are not accounted for in the theoretical calculation of the primary

Gaussian term. In theory, these events should be modeled in a more physical manner; however, they were not separately treated in this work. The two secondary nuclear pencil beams simply accounted for the differences between the primary Gaussian and all other interactions.

3.2 Isodose Comparisons

Isodose distributions calculated with the PBA were compared to those simulated using Monte Carlo. All of the distributions were normalized to the maximum dose in a flat water phantom and the 1, 2, 5, 10, 20, 30, 40, 50, 60, 70, 80, 90, and 100 percent isodose lines were contoured. The test geometries were broken down into the subsections consisting of homogeneous water phantoms, homogeneous compact bone phantoms, water phantoms containing laterally infinite compact bone slabs, water phantoms containing laterally infinite air slabs, water phantoms containing laterally finite compact bone slabs, and water phantoms containing laterally finite air slabs. In the interest of brevity, only representative samples of the results are presented in this section. A display of all results can be seen in the Appendices A and B.

3.2.1 Homogenous Phantoms

Figure 3.6 shows the 2D dose distribution comparisons of Monte Carlo and PBA for a 10 x 10 cm^2 250 MeV beam incident on a water phantom for (a) the previous 2-term PBA and (b) current 3-term PBA. The 2-term PBA showed better than 99.0% of points within 2% or 1 mm of Monte Carlo for all flat water phantom simulations, where as the present 3-term PBA showed 100% of points within 2% or 1 mm. Even though the number of points passing was nearly the same, inspection of the isodose lines revealed better agreement in low (≤ 5% isodose) dose regions. The previous 2-term model matched Monte Carlo simulations out to the 5% isodose and showed a improvement over previous single Gaussian models (Hong 1996 and Ciangaru 2005). However, outside of the 5% isodose, the PBA consistently underestimated the dose compared to Monte Carlo data. By contrast, the new model showed agreement to the 1%

isodose line. For all field sizes and energies, the 3-term PBA calculated dose within 2% or 1 mm data of Monte Carlo for 100% of points tested. Comparison of Monte Carlo and PBA calculations are also provided for a 250 MeV 4 x 4 cm^2 field, 200 MeV 4 x 4 cm^2 field,150 MeV 4 x 4 cm^2 field, and a 100 MeV 4 x 4 cm^2 field incident on a water phantom can be seen in Figure 3.7.

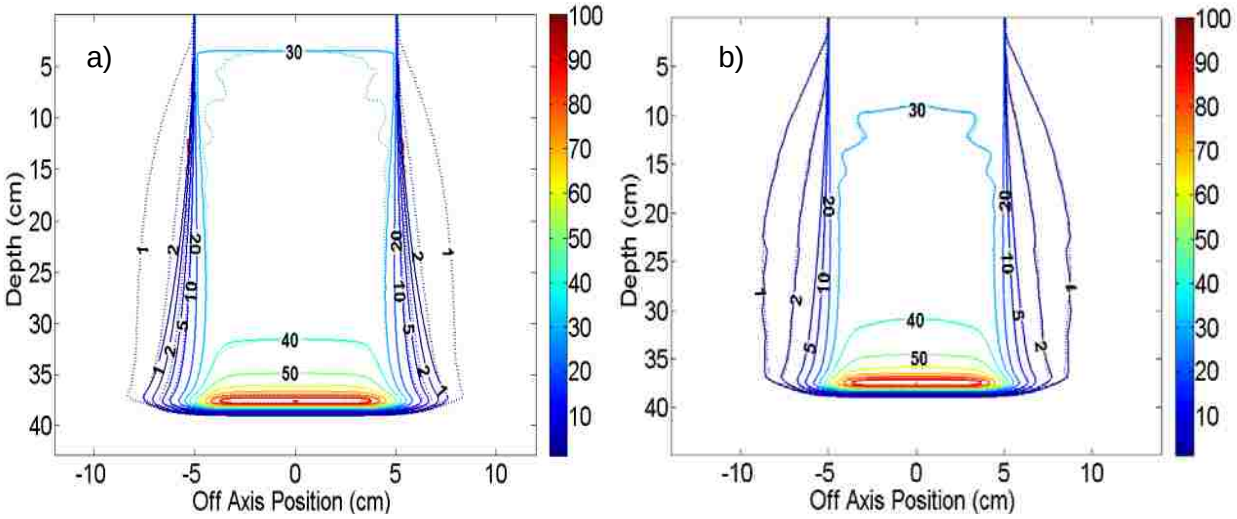

Figure 3.6: Isodose comparisons between Monte Carlo (dashed lines) and PBA (solid lines) in a homogenous water phantom for a 250 MeV 10 x 10 cm^2 field. In figure a) the PBA data was produced using a two Gaussian model. In figure b) PBA data was produced using the new three term model. The pass rates were 99.9% and 100% for a) and b), respectively, but one can see visually the superior agreement in the low dose region achieved in b) with the use of the three termed model.

For the homogenous compact bone phantom, at least 99.5% of PBA dose points were within 2% or 1 mm of Monte Carlo simulations for all field sizes and energies. The results for the 200 MeV 10 x 10 cm^2 field are shown in Figure 3.8 and are representative of the results with other fields sizes and energies. The PBA overestimated (~1-2 cm DTA) the lateral spread of the one and two percent isodose lines. This occurred because the parameters for the PBA nuclear halo terms were determined in water. Since compact bone has a larger linear stopping power, secondary protons created upstream travel less distance, causing significantly less spread in the low dose isodose lines. However, this difference is not of clinical significance and the dose points in these regions were within the 2% or 1mm criteria.

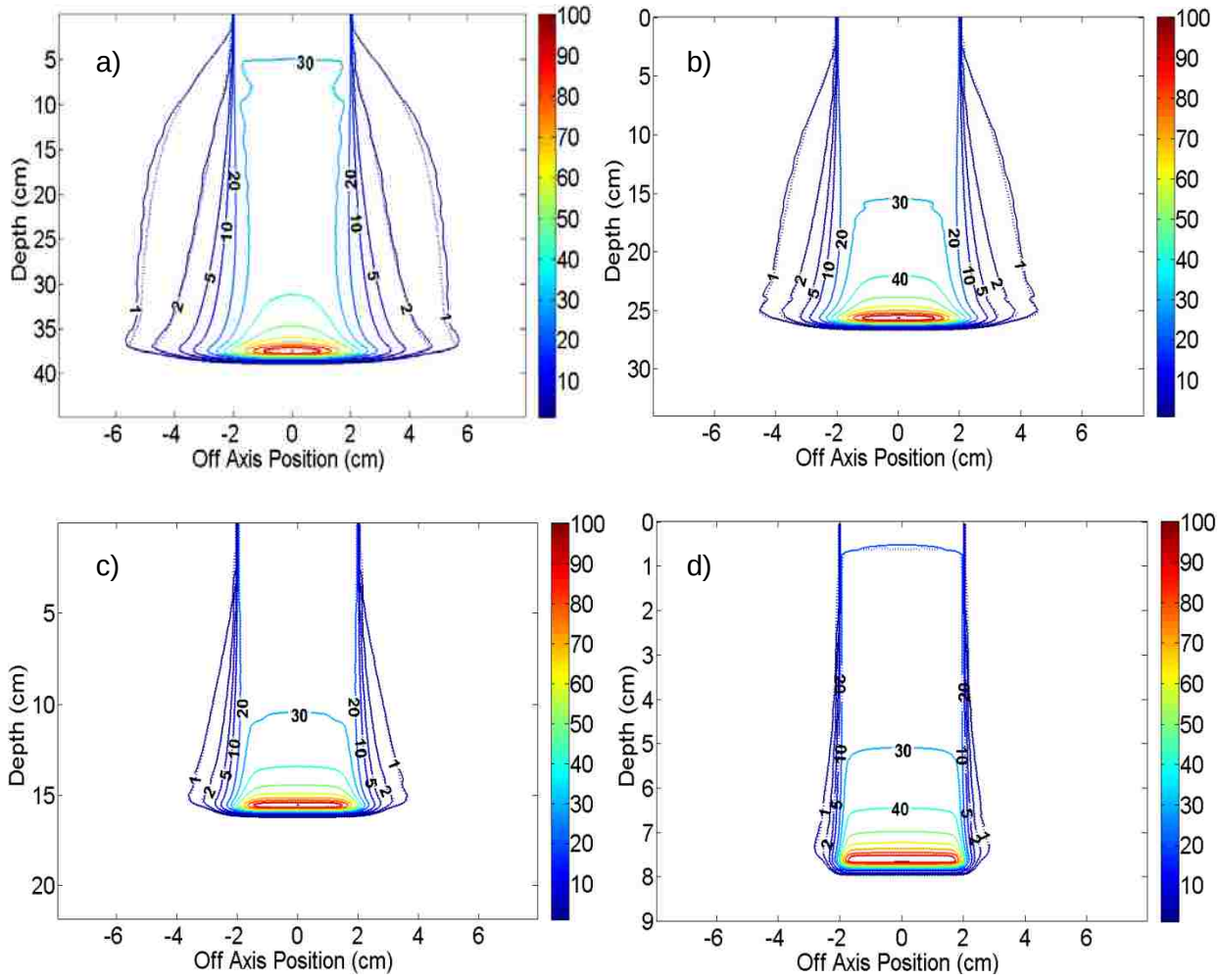

Figure 3.7: Some representative isodose comparisons between Monte Carlo (dashed lines) and PBA (solid lines) in a homogenous water phantom. a) 250 MeV 4 x 4 cm^2 field, b) 200 MeV 4 x 4 cm^2 field, c) 150 MeV 4 x 4 cm^2 field, d) 100 MeV 4 x 4 cm^2 field . There was excellent agreement out to the 1% isodose for all field sizes and energies.

The PBA underestimated the dose in the Bragg peak in the compact bone phantom by 2.5-6% (Figure 3.8b). Ciangaru (2005) reported similar discrepancies (~1-10%) for a humorous bone phantom. There are several factors that could have contributed to this. First, MCNPX explicitly performs material dependent transport of secondary protons, while the PBA accounts for their transport via curve fits done in water but has no material dependence. The Monte Carlo output file indicated there was a reduction in the number of secondary particles produced from non-elastic interactions in compact bone compared to water. The PBA did not model this. Second, while the range straggling correction in MCNPX depends on material, the PBA

incorporates range straggling that is included in the input data, which, in this was work, was acquired in water. Since this input data used depth dose curves simulated in water it did not account for this material dependence, which could have led to differences in the Bragg peak dose. Finally, the PBA and MCNPX use different stopping power energy binning. MCNPX binned the stopping powers used based on a percentage of the energy, while the PBA used a fixed 0.5 MeV energy step. These slight differences in how energy loss is modeled could produce differences in Bragg peak dose between PBA and Monte Carlo calculations. All of these differences may have led to slight differences in Bragg peak between the Monte Carlo data and the PBA.

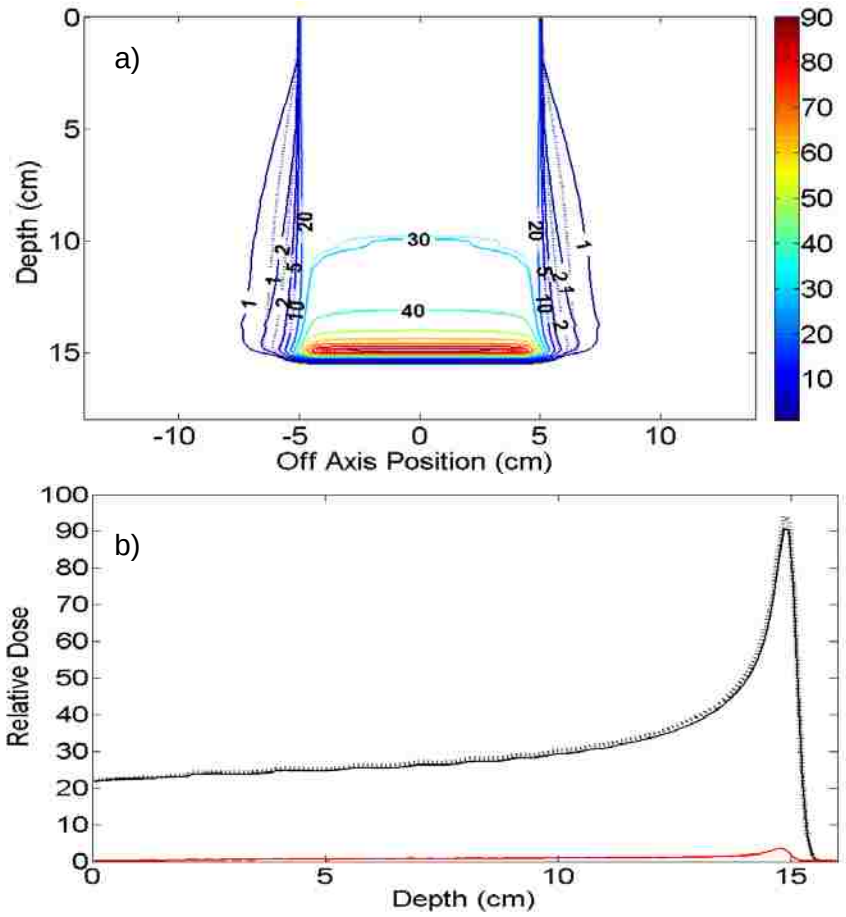

Figure 3.8: (a) Isodose comparison and (b) percent depth dose comparison between Monte Carlo (dashed lines) and PBA (solid lines) in a homogenous compact bone phantom for a 200 MeV 10 x 10 cm^2 field. There was an overestimation (~1%) of the low dose off axis region and an underestimation (~3.75%) in the Bragg peak. In figure b) the red line is the absolute difference between the PBA and Monte Carlo.

To summarize the results for uniform density phantoms, for all energies and field sizes, the PBA was able to calculate dose within 2% or 1 mm of Monte Carlo for 100% of the dose calculation points tested in a homogeneous water phantom. 97.91% or greater of the PBA dose calculation points were within the criteria of Monte Carlo for calculations in the homogenous compact bone phantom. A summary of percentage of points within 2% or 1 mm of Monte Carlo can be seen in Table 3.1. There was an overestimation (~1%) of low dose off axis regions and underestimation (~2-6%) of the Bragg peak dose in the compact bone phantom. These errors were so small that several field size and energy combinations still had a pass rate of 100%. Given the excellent agreement in the homogeneous water phantom and that patients are made of mostly water, not compact bone, these relatively small errors are likely of little clinical significance.

Table 3.1: Summary of the percentage of points within 2% or 1 mm of Monte Carlo for uniform phantoms.

Percentage of Pixels Within 2% or 1 mm:					
Field Size (cm^2)	**4x4**		**10x10**		
Energy (MeV)	**Water Phantom**	**Compact Bone Phantom**	**Water Phantom**	**Compact Bone Phantom**	
100	100	100	100	100	
150	100	99.31	100	99.67	
200	100	99.43	100	99.85	
250	100	97.91	100	100	

3.2.2 Laterally Infinite Slabs

Geometries consisting of a water phantom with a 2 cm or 5 cm thick laterally infinite compact bone slab placed at different depths were examined. Figure 3.9 shows the isodose comparisons between Monte Carlo (dashed lines) and PBA (solid lines) in a water phantom containing a 2 cm or 5 cm thick compact bone slab located at different depths. For these geometries, the PBA

was able to calculate dose with at least 99.18% of points within 2% or 1 mm of Monte Carlo calculations for all field sizes and energies considered here.

The PBA overestimated the low dose region distal to the proximal edge of the bone slab. These 2-10 mm DTA values in the 1% and 2% isodose lines can be most clearly seen in Figure 3.9c & d. This was due to the lack of material dependence in the halo terms. Since these errors are small and in a very low dose area likely they are not clinically significant.

Figure 3.10 shows a depth dose profile and cross field profile through the Bragg peak for a 250 MeV 10 x 10 cm^2 field incident on a water phantom with a 5 cm thick bone slab located at 30 cm depth. The cross field profile shows excellent agreement (< 0.5 mm DTA) in the penumbral region, whereas other works have shown discrepancies of approximately 1 to 2 mm for similar energy and geometries (Ciangaru 2005, Szymanowski 2002). The depth dose profile shows that the PBA underestimates the maximum dose in the Bragg peak (~1-4%) but the overall agreement is very good. By the same logic used in the compact bone phantom results, the differences in Bragg peak dose was mostly likely due to slight differences in stopping powers, their energy binning, the lack of a material dependent range straggling correction, and changes in the production of secondary particles from non-elastic nuclear interactions not being modeled by the PBA. The underestimation of the dose after the bone slab is probably of little clinical importance since most treatments will not treat through compact bone thicker than 5 cm.

Small differences in the location (~±1 mm) of the Bragg peak maximum dose between the PBA and Monte Carlo were seen and were most likely due to 1 mm x 1 mm resolution of the calculation and differences in stopping powers and their energy binning. Differences in the location of maximum dose of the Bragg peak caused large dose differences in some simulations, but since the points passed the 1 mm DTA criteria, there was no significant regions of failure. Our range prediction fell within typical uncertainties as reported by Schaffner (1998), where typical uncertainties in range were reported to be between 1-3 mm. A full summary of the pass rate results can be seen in Table 3.2.

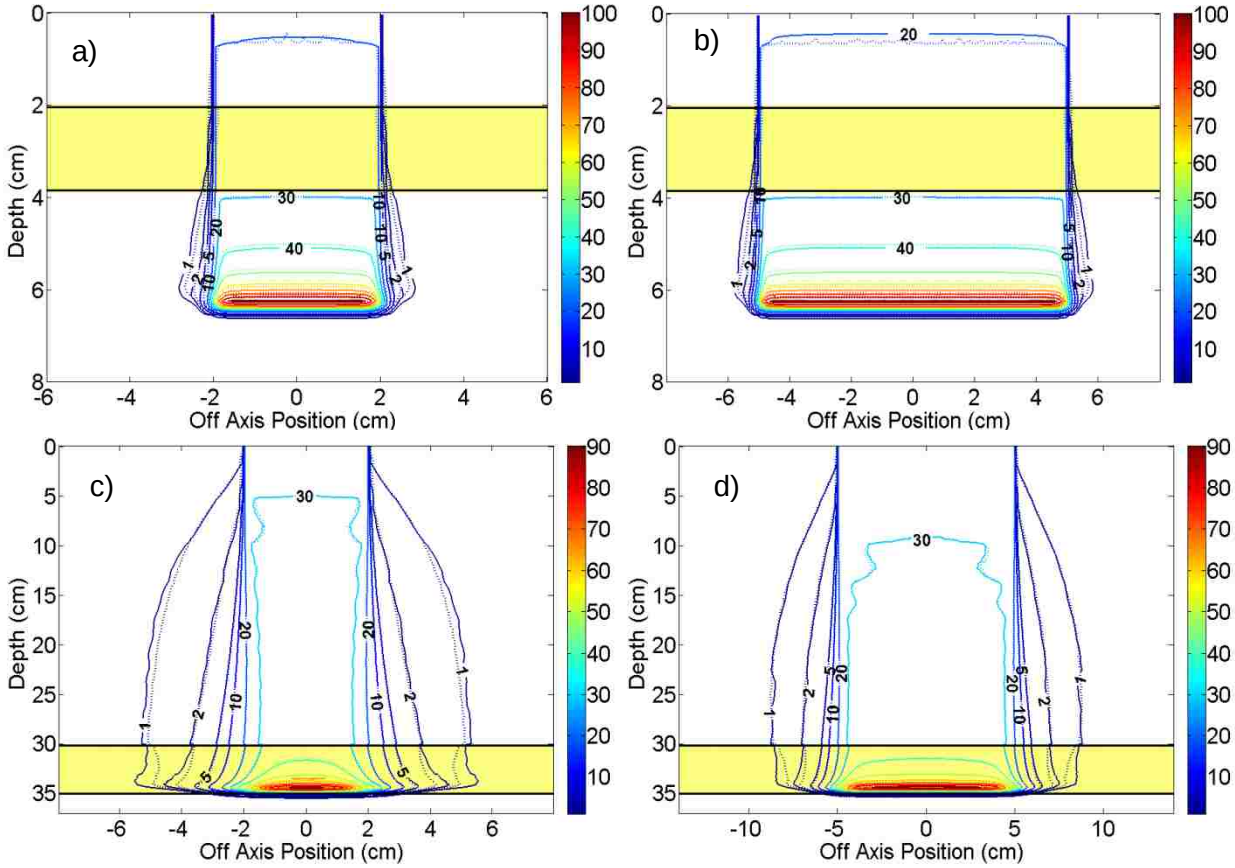

Figure 3.9: Some representative isodose comparisons between Monte Carlo (dashed lines) and PBA (solid lines) in a water phantom containing a 2 cm or 5 cm thick compact bone slab (shown in yellow) located at different depths (zslab). a) 100 MeV 4 x 4 cm^2 field: (zslab: 2 cm, Pass rate: 100%. b) 100 MeV 10 x 10 cm^2 field: (zslab: 2 cm, Pass rate: 100%). c) 250 MeV 4 x 4 cm^2 field: (zslab: 30 cm, Pass rate: 99.47%). d) 250 MeV 10 x 10 cm^2 field: (zslab: 30 cm, Pass rate: 99.79%). In all of the figures the small percentage of failing pixels are located in the Bragg peak.

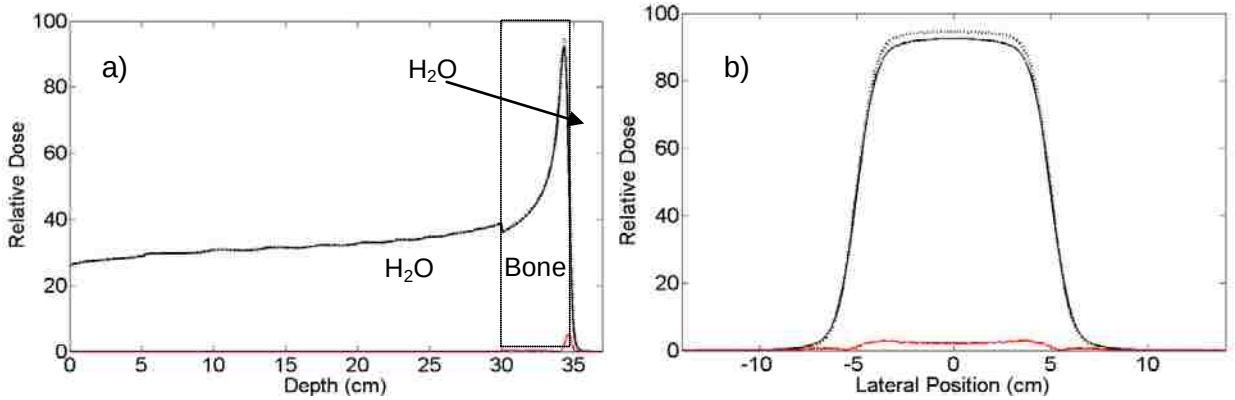

Figure 3.10: a) Central axis percent depth dose comparison for the geometry in Figure 3.9d between Monte Carlo (dashed line) and PBA (solid line) The pba underestimates the maximum dose by approximately 4%. One will note the abrupt drop in the depth dose at the proximal edge of the bone slab (Z = 30 cm). This is due to the mass stopping power ratio of bone to water being approximately 0.93. b) Lateral profile through the Bragg peak at z = 34.35 cm. There was good agreement in the penumbra but an underestimation of the maximum dose. In

both panels the absolute value of the difference between the Monte Carlo and PBA is plotted in red.

Geometries consisting of a water phantom with a 2 cm or 5 cm thick laterally infinite air slab placed at different depths were examined. Figure 3.11 shows the isodose comparisons between Monte Carlo (dashed lines) and PBA (solid lines) in a water phantom containing a 5 cm thick air slab located at different depths. For laterally infinite air slab geometries, the PBA was able to calculate dose with at least 93.2% of points within 2% or 1 mm of Monte Carlo calculations for all field sizes and energies.

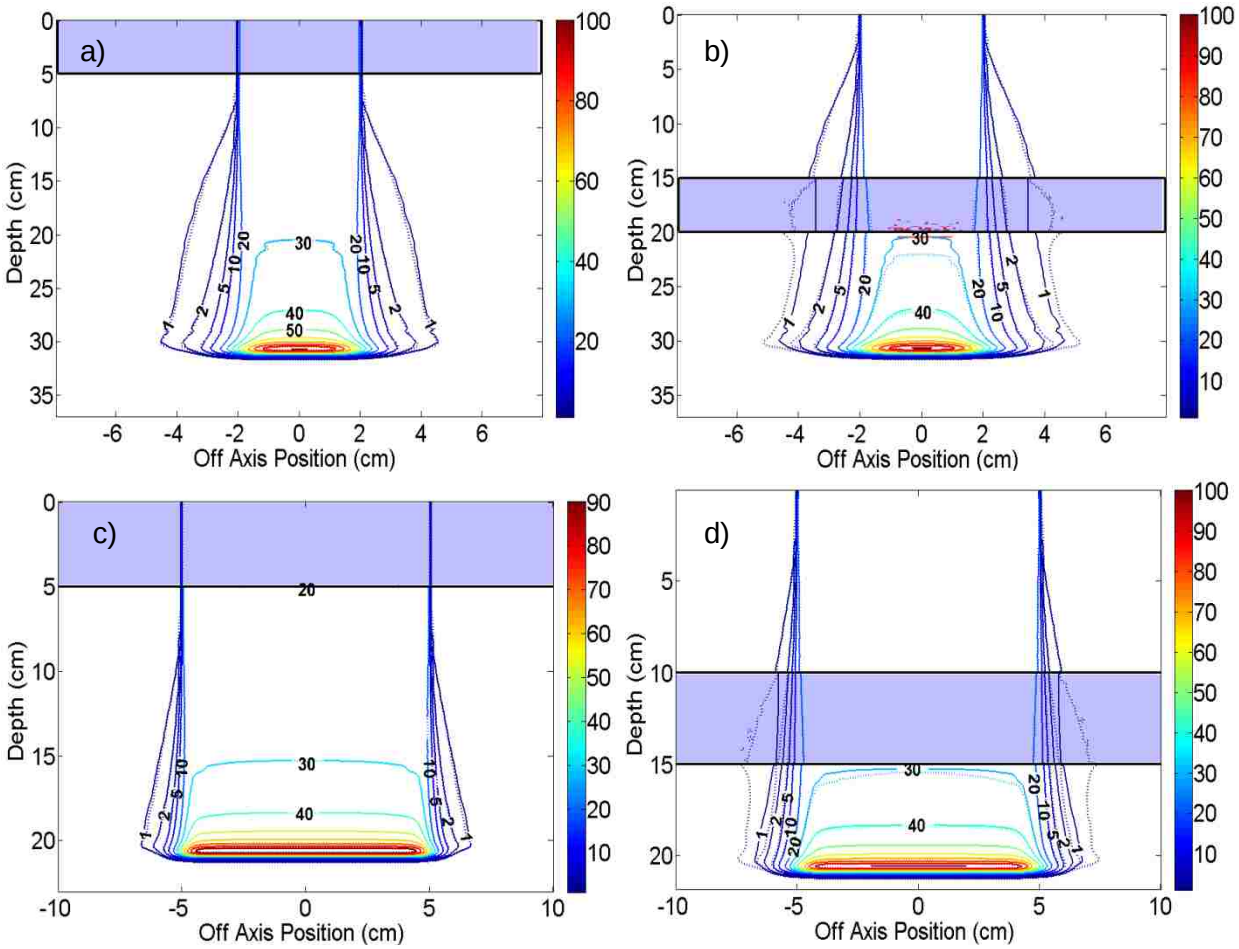

Figure 3.11: Some representative isodose comparisons between Monte Carlo (dashed lines) and PBA (solid lines) in a water phantom containing 5 cm air slab located at different depths (zslab) shown in blue. The maximum dose difference (Max DD) and mean dose difference (Mean DD) are reported. a) 200 MeV 4 x 4 cm^2 field: (zslab: 0 cm, Pass rate: 100%, Max DD: 1.54%, Mean DD: 0.10%). b) 200 MeV 4 x 4 cm^2 field: (zslab: 15 cm, Pass rate: 99.69%, Max DD: 3.24%, Mean DD: 0.42%). c) 150 MeV 10 x 10 cm^2 field: (zslab: 0 cm, Pass rate: 100%, Max DD: 2.06%, Mean DD: 0.12%). d) 150 MeV 10 x 10 cm^2 field: (zslab: 10 cm, Pass rate: 100%, Max DD: 2.64%, Mean DD: 0.34%). The red pixels indicate points failing the criteria.

Figure 3.12 shows the 2D isodose comparison for a 4 x 4 cm^2 beam incident on a water phantom with a 5 cm thick air slab at 30 cm depth. Figure 3.13 shows a depth dose curve for the same geometry. Figure 3.14 shows the 2D dose difference between the PBA and Monte Carlo. The PBA overestimated the maximum dose in the phantoms containing air slabs. In all cases, the depth dose curves for simulations containing an air slab, there was the abrupt drop in the depth dose at the proximal edge of the air slab due to the mass stopping power ratio of air to water being approximately 0.89 (Figure 3.13). However one can see, the Monte Carlo depth dose starts to decrease with depth while going through the air slab and the PBA depth dose curve does not. This was a small effect (~1-2%) for the 2 cm thick air slab and was even less of an effect for slabs located at shallow depths, however for certain geometries this effect became more apparent. Distal to the air slab the PBA overestimates the dose along the central axis by 3 to 7%; causing a large region of failure, approximately 7% of the area tested.

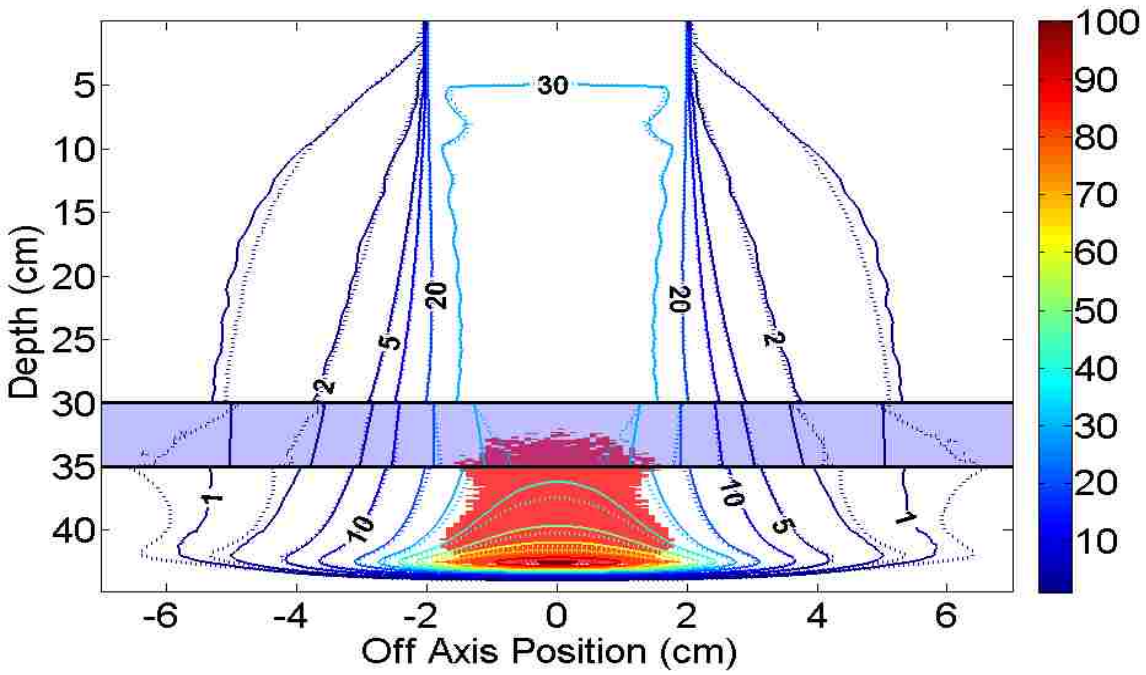

Figure 3.12 Isodose comparison between Monte Carlo simulation (dash lines) and PBA calculation (solid lines) for a 250 MeV 4x4 cm^2 beam incident on a water phantom with a 5 cm laterally infinite air slab (blue) located at 30 cm depth. The pass rate was 93.2% with a maximum difference of 6.90% and mean difference of 3.03% in the failing regions (shown by red pixels). There was good agreement off axis but an overestimation along the central axis after the air slab.

The overestimation in dose distal to the air slab was most likely due to the changes in the secondary proton fluence not modeled by the PBA; specifically the loss of charge particle and side scatter equilibrium of secondary protons going through the air slab. This effect decreased with increasing field size because of the larger contribution to the central axis due to scatter off axis for larger field sizes. Smaller field sizes were more sensitive to the abrupt changes in scatter and secondary particle production caused by the 5 cm air slab than larger field sizes, because fewer particles scatter into the central axis. Figure 3.15 shows the 2D isodose comparison for a 10 x 10 cm^2 beam incident on a water phantom with a 5cm thick air slab at 30 cm depth. This loss of side scatter equilibrium of secondary particles was greatly reduced in the 10 x 10 cm^2 calculation. The PBA calculation was able to calculate 100% of the points within 2% or 1 mm of Monte Carlo for a 10 x 10 cm^2 compared to 93.2% for the 4 x 4 cm^2 case. The underestimation distal to the Bragg peak was reduced to ~ 2% vs. ~7%. This error was also reduced in lower energy calculations where secondary particle production, secondary particle energy, and lateral displacement were reduced.

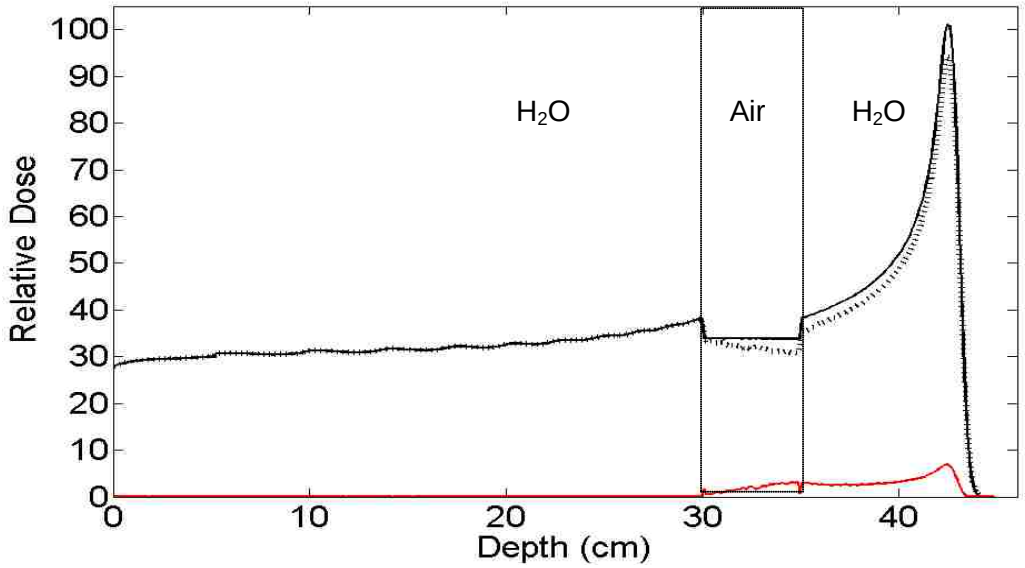

Figure 3.13: Percent depth dose comparison between Monte Carlo (dashed line) and PBA (solid line) for a 250 MeV 4x4 cm^2 beam incident on a water phantom with a 5 cm laterally infinite air slab located at 30 cm depth. The absolute difference between the two can be seen in red. The PBA overestimates the dose by approximately 2-6 % after the beginning of the air slab. This occurred because the PBA did not model the loss of side scatter equilibrium of the secondary particles produced above the slab or the lack of production of secondary particles in the slab.

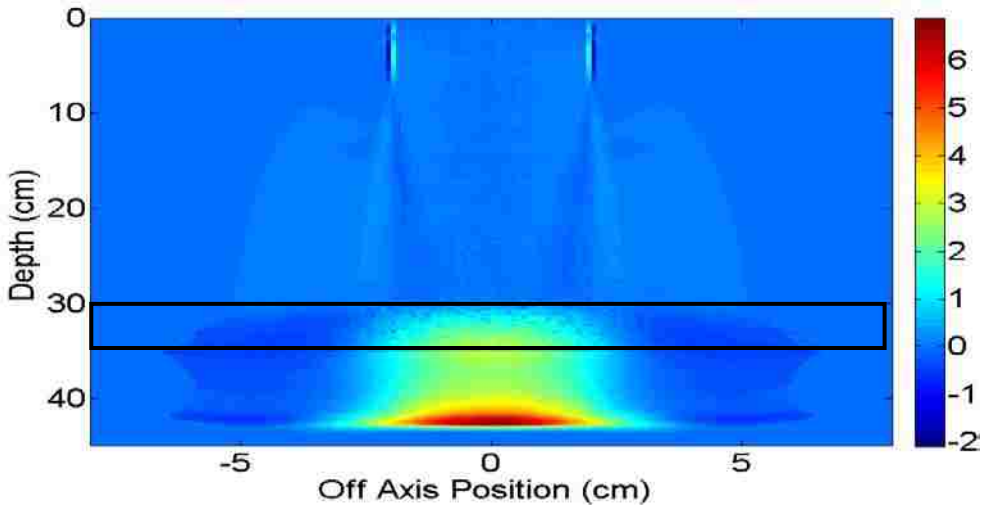

Figure 3.14: The 2D Monte Carlo dose distribution subtracted from the 2D PBA dose distribution for the geometry in Figure 3.12. One can see the gradual increase in the overestimation of the PBA after entering the air slab at 30 cm in depth (outlined in black). There is also an underestimation in the low dose off axis region due to the lack of material dependence in the nuclear halo model.

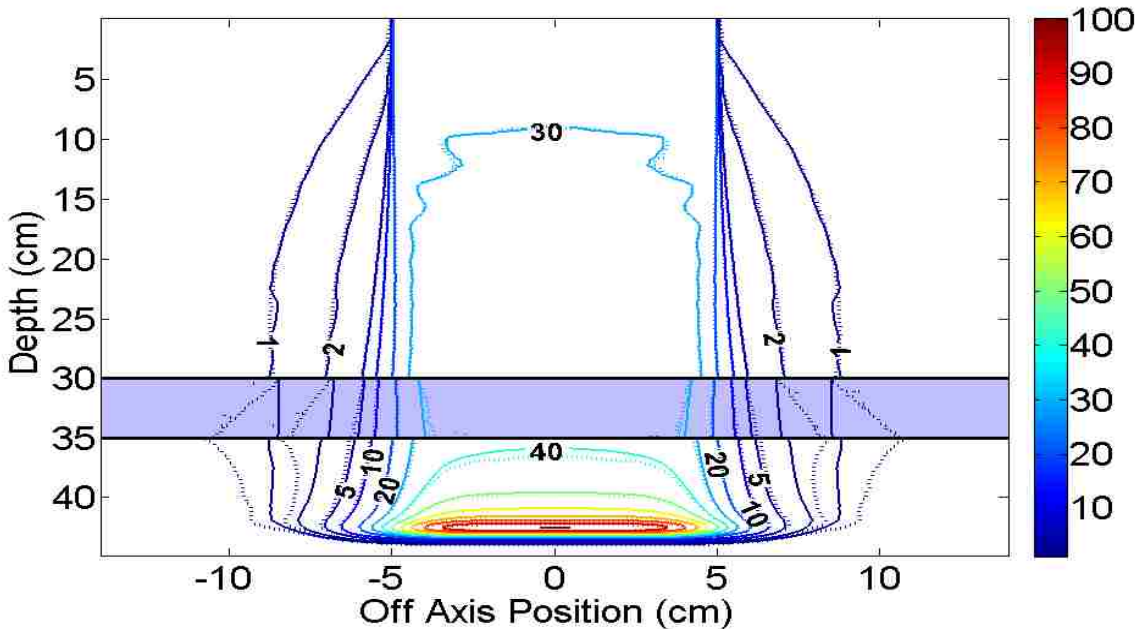

Figure 3.15: Isodose comparison between Monte Carlo simulation (dash lines) and PBA calculation (solid lines) for a 250 MeV 10x10 cm^2 beam incident on a water phantom with a 5 cm laterally infinite air slab located at 30 cm depth. The pass rate was 99.99% with a maximum difference of 2.07% and mean difference of 2.04%. The underestimation distal to the air slab seen in the 4 x 4 cm^2 simulation was still present but the magnitude was reduced significantly.

Table 3.3 provides a full summary of the percentage of pixels within the 2% dose difference or 1 mm distance to agreement. The vast majority of the geometries studied had pass rates greater than 99% and showed good agreement with Monte Carlo. Even though in the majority

of circumstances the PBA performed extremely well, it should be noted for high energy (250 MeV) and small field size (< 4x4 cm^2) beams treating sites with large (> 5 cm thick) air heterogeneities located in the last 75% of the range, the PBA's overestimation of dose distal to the air slab could lead to errors on the order of 7%. This could be of considerable clinical significance in the treatment of lung tumors for instance.

Table 3.2: : Summary of results of the percentage of PBA calculated dose points within 2% or 1 mm of Monte Carlo for water phantoms containing laterally infinite compact bone slabs.

Percentage of Pixels Within 2% or 1 mm:									
2 cm Compact Bone Slab									
		100 MeV		**150 MeV**		**200 MeV**		**250 MeV**	
		FS (cm^2)		**FS (cm^2)**		**FS (cm^2)**		**FS (cm^2)**	
Depth (cm)		**4x4**	**10x10**	**4x4**	**10x10**	**4x4**	**10x10**	**4x4**	**10x10**
2		100	100	100	100	100	100	100	100
30		n/a	n/a	n/a	n/a	n/a	n/a	99.18	100
5 cm Compact Bone Slab									
		100 MeV		**150 MeV**		**200 MeV**		**250 MeV**	
		FS (cm^2)		**FS (cm^2)**		**FS (cm^2)**		**FS (cm^2)**	
Depth (cm)		**4x4**	**10x10**	**4x4**	**10x10**	**4x4**	**10x10**	**4x4**	**10x10**
0		100	100	100	100	100	100	100	100
30		n/a	n/a	n/a	n/a	n/a	n/a	99.47	99.79

To summarize the results for phantoms containing laterally infinite slabs of compact bone or air, the PBA showed greater than 99% of dose calculation points were within 2% or 1 mm of Monte Carlo for all but 3 of the 70 geometries tested. In the three cases where a 250 MeV 4 x 4 cm^2 field was incident on a water phantom with a 5 cm thick air slab located at 15, 25, and 30 cm, the PBA failed to predict a loss of side scatter equilibrium of secondary protons along the central axis due to the air slab. This caused an overestimation of dose distal to the slab. For

larger air heterogeneities with smaller field sizes this error could be significant and could warrant future investigation. For all other cases the PBA showed excellent accuracy and great potential for future development into a clinical dose calculation algorithm.

Table 3.3: Summary of results of the percentage of PBA calculated dose points within 2% or 1 mm of Monte Carlo for water phantoms containing laterally infinite air slabs.

Percentage of Pixels Within 2% or 1 mm:								
2 cm Air Slab								
	100 MeV		**150 MeV**		**200 MeV**		**250 MeV**	
	FS (cm^2)		**FS (cm^2)**		**FS (cm^2)**		**FS (cm^2)**	
Depth (cm)	**4x4**	**10x10**	**4x4**	**10x10**	**4x4**	**10x10**	**4x4**	**10x10**
2	100	100	100	100	100	100	100	100
5	100	100	100	100	100	100	100	99.99
10	n/a	n/a	100	100	100	100	100	100
15	n/a	n/a	n/a	n/a	100	100	100	100
30	n/a	n/a	n/a	n/a	n/a	n/a	99.96	100
5cm Air Slab								
	100 MeV		**150 MeV**		**200 MeV**		**250 MeV**	
	FS (cm^2)		**FS (cm^2)**		**FS (cm^2)**		**FS (cm^2)**	
Depth (cm)	**4x4**	**10x10**	**4x4**	**10x10**	**4x4**	**10x10**	**4x4**	**10x10**
0	100	100	100	100	100	99.99	100	100
10	n/a	n/a	100	100	100	100	99.34	100
15	n/a	n/a	n/a	n/a	99.69	100	98.17	99.99
25	n/a	n/a	n/a	n/a	n/a	n/a	97.43	100
30	n/a	n/a	n/a	n/a	n/a	n/a	93.2	99.99

3.2.3 Laterally Finite Slabs

Geometries consisting of a water phantom with a 2 cm thick laterally finite air or compact bone slab placed at different depths were examined. For water phantoms containing a laterally finite 2 cm thick compact bone slab greater than 95.76% of PBA dose calculation points were within 2% or 1 mm of Monte Carlo. In all but one case, greater than 97.5% of dose calculation points were within the criteria of Monte Carlo. Failures were caused by the central axis approximation used in the PBA. The central axis approximation assumes, for a given pencil beam, whatever material is along the central axis is laterally infinite. Thus, the sharp lateral edge of the slab caused an error in the PBA were it did not in Monte Carlo. For slabs located in the first 50% of the range, 99% of dose calculation points were within the criteria of Monte Carlo. Because both scatter and energy deposition increase with depth, this error increased significantly when the slab was placed in the second half of proton range. The percentage of dose calculation points within 2% or 1 mm of Monte Carlo can be seen in Table 3.4.

The pass rates for the larger field size were consistently 1 to 2 percent higher than the smaller field size. This was simply due to having more dose points that were unaffected by the slab that helped obtain a higher pass rate. The error produced was of the same magnitude even though the pass rate was higher. The same can be said for the higher energies. For slabs placed at a depth corresponding to the same percentage of the range, the higher energy beams have a greater pass rate, because there were simply more dose points that were unaffected by the slab. In this case, the errors produced in the higher energy simulation were actually of greater magnitude, but they had the higher pass rate. These are two limitations of using pass rate as the only metric of accuracy of the PBA. To counteract this, dose difference plots, lateral profiles, and depth dose profiles were relied on more heavily than in the previous section.

For the 150 MeV proton beams, the compact bone slab was placed at 2, 5, and 10 cm depths. This corresponds to approximately 13, 32, and 64 percent of the range in water

respectively. The isodose comparisons for the two extremes can be seen in Figure 3.16. The pass rates dropped as the slab position increased in depth as expected. They were 99.95, 99.74, and 95.76 percent, respectively. The maximum errors also increased as the slab was placed in the second half of the range. They were 4.41, 4.25, and 14.25 percent, respectively. The same can be said for mean dose differences, which were 3.19, 2.68, and 5.48 percent. Any algorithm using the central axis approximation will display this general behavior. For instance, this trend is consistent with results from Schaffner (1998). Their results for a 1 x 1 cm^2 170 MeV beam incident on a similar geometry show the maximum dose difference is approximately10% when a 2 cm bone slab was place at the surface. This difference increased to approximately 27% when the slab was placed at 18 cm depth.

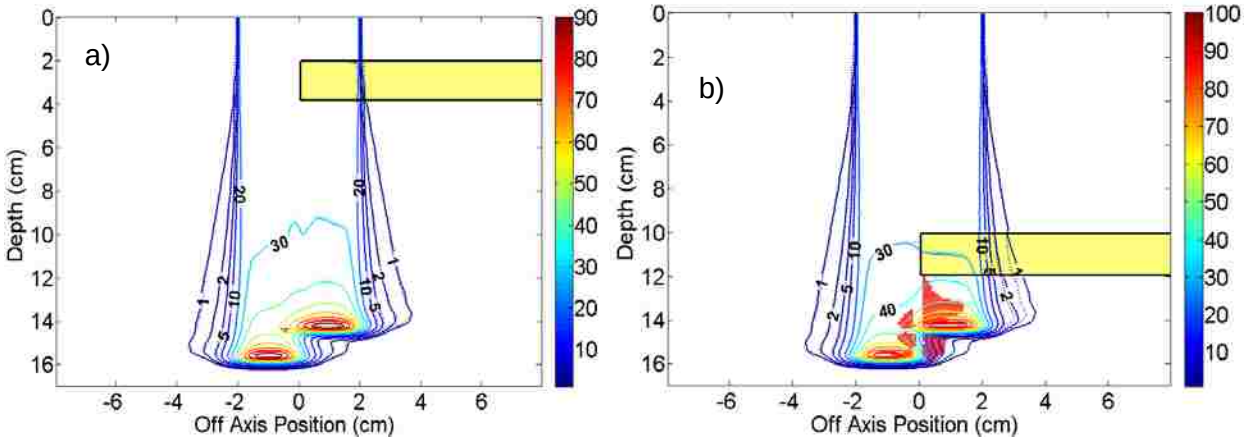

Figure 3.16: Isodose comparisons between Monte Carlo (dashed lines) and PBA (solid lines) in a water phantom containing 2 cm compact bone slab located at different depths (zslab). The maximum dose difference (Max DD) and mean dose difference in the failing region (Mean DD) were reported. a) 150 MeV 4 x 4 cm^2 field: (zslab: 2 cm, Pass rate: 100%, Max DD: 4.41%, Mean DD: 3.19%). b) 150 MeV 4 x 4 cm^2 field: (zslab: 10 cm, Pass rate: 99.69%, Max DD: 14.25%, Mean DD: 5.48%). Red pixels indicate a failing point.

All field sizes and energies exhibited the same behavior with the four areas of failure which grew as the slab was placed in the second half the range. These errors were all caused by the central axis approximation. The geometry shown in Figure 3.16b serves as a good example. Figure 3.17 shows the dose difference plot between the PBA and Monte Carlo for this geometry. The typical X shape caused by the central axis approximation discussed in section 1.1.3 is present. For pencil beams passing through the bone slab, the PBA assumes the slab is laterally

infinite. This causes an overestimation (hot spot) and an underestimation (cold spot) on the left side of the central axis by the PBA relative to Monte Carlo. Conversely pencil beams not passing through the bone, the PBA assumes the slab is not there, which causes a wide cold spot and a narrow hot spot on the right side of the central axis.

Dose distal to the bone slab increased slightly faster in the Monte Carlo than in the PBA. This was seen in the laterally infinite slab geometries as well. The PBA also predicted the maximum dose to be 1 mm distal of the Monte Carlo prediction. This caused a hot spot with a large dose difference that passed the DTA criteria. This 1 mm difference in the range of protons seemed to decrease the width of the hot spot on the left side caused by the central axis approximation. The mean dose difference in the failing region was 5.48% and the maximum dose difference in the failing region was 17.58%.

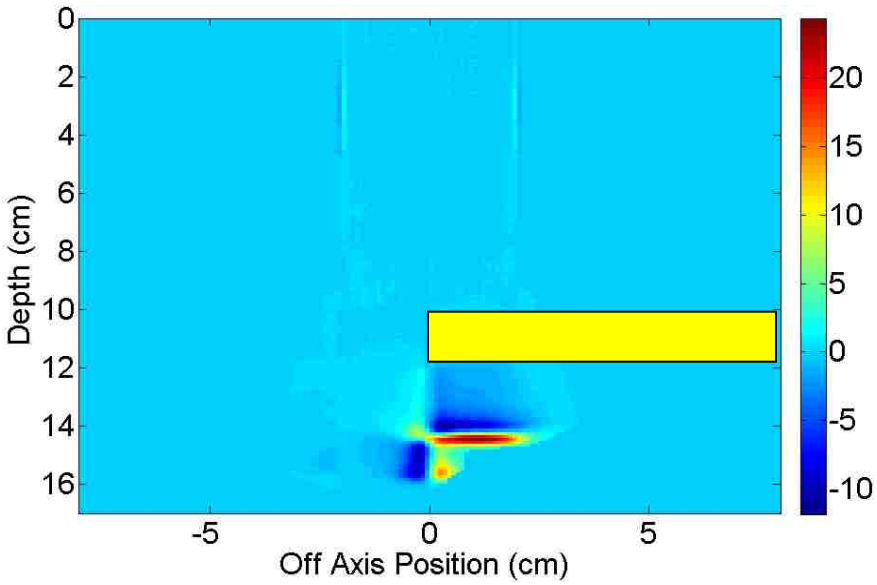

Figure 3.17 The 2D Monte Carlo dose distribution subtracted from the 2D PBA dose distribution for the geometry in Figure 3.16b. The color bar shows percentage of the maximum dose in a flat water phantom. This illustrates where the PBA overestimates the dose relative to Monte Carlo (hot spot shown in red) and underestimates the dose relative to Monte Carlo (cold spots shown in blue) created by the central axis approximation along with a slight difference in the range when going through compact bone which manifests itself as a hot spot distal to the bone slab.

Figure 3.18 shows lateral and depth dose profiles taken through the four regions with failing pixels. The profiles illustrate the problems with the PBA. First the central axis approximation will cause the hot and cold spots as just discussed. They are present in all four of the profiles.

Also there was a one pixel difference in the prediction of the range and energy deposition distal to the bone slab increased more rapidly in the Monte Carlo than in the PBA. This caused an additional hot spot in Figure 3.18a. As previously discussed this was most likely caused by differences in stopping power binning and the 1 mm pixel resolution. Regions not affected by the central axis approximation agreed with Monte Carlo as expected from the results in the previous sections.

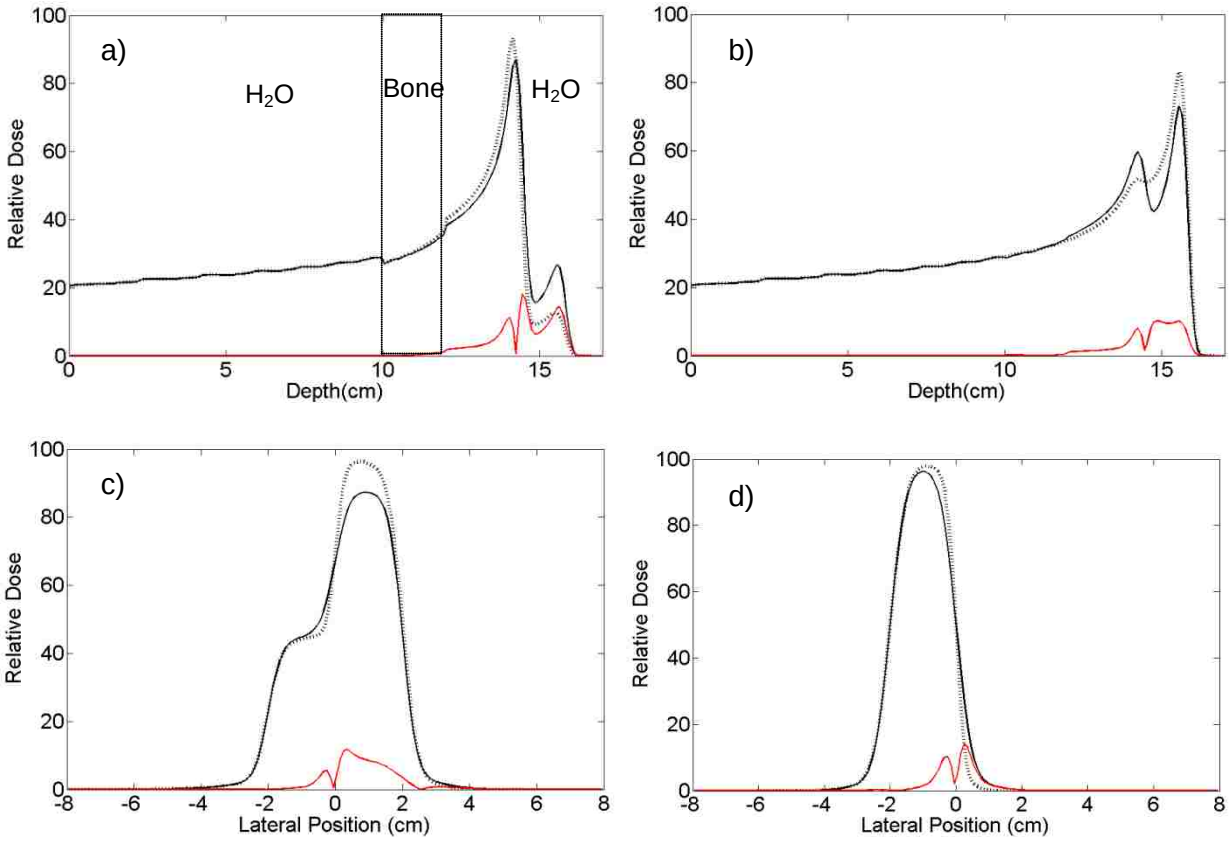

Figure 3.18: Profiles taken through the four failing regions of the geometry shown in Figure 3.16b. Figures a & b are depth dose profiles taken at X = 0.25 cm and – 0.25 cm respectively. Monte Carlo (dashed line) was plot with PBA (solid line). The absolute difference between the two was plotted as well (red line). In figure a) one can see three separate errors occurring: first a cold spot then two hot spots. The cold spot and second hot spot were formed from the central axis approximation. The first hot spot was caused by the one pixel difference in range when going through compact bone. In figure b) there was a hot spot then cold spot from the central axis approximation. Figures c) and d) are lateral profiles taken at Z = 14.05 cm and 15.55 cm respectively. Again one can see the hot (overestimation by the PBA) and cold (underestimation by the PBA) spots caused by the central axis approximation.

The error in the range wasn't seen in all simulations. For instance, in the 250 MeV 10 x10 cm^2 simulations, this error was not present. The 250 MeV 10 x10 cm^2 isodose comparisons are

shown in Figure 3.19 along with the 2D dose difference plot in Figure 3.20. Only the hot and cold spots due to the central axis approximation were present (see Figures 3.20 & 3.21). Figure 3.21 shows depth dose and lateral profiles for this geometry as well. The agreement is very similar to the results shown in Figure 3.18, except for the absence of the 1 mm discrepancy in range.

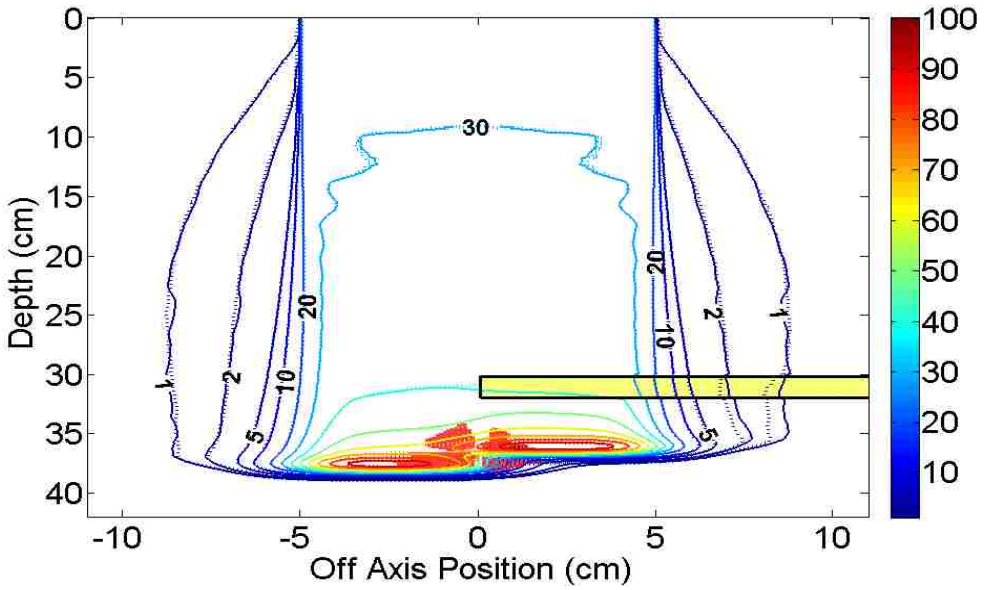

Figure 3.19: Isodose comparisons between Monte Carlo (dashed lines) and PBA (solid lines) for a 250 MeV 10 x10 cm^2 beam incident on a water phantom containing 2 cm compact bone slab (yellow) located at 30 cm. (Pass rate: 98.60%, Max DD: 19.88%, Mean DD: 7.25%).

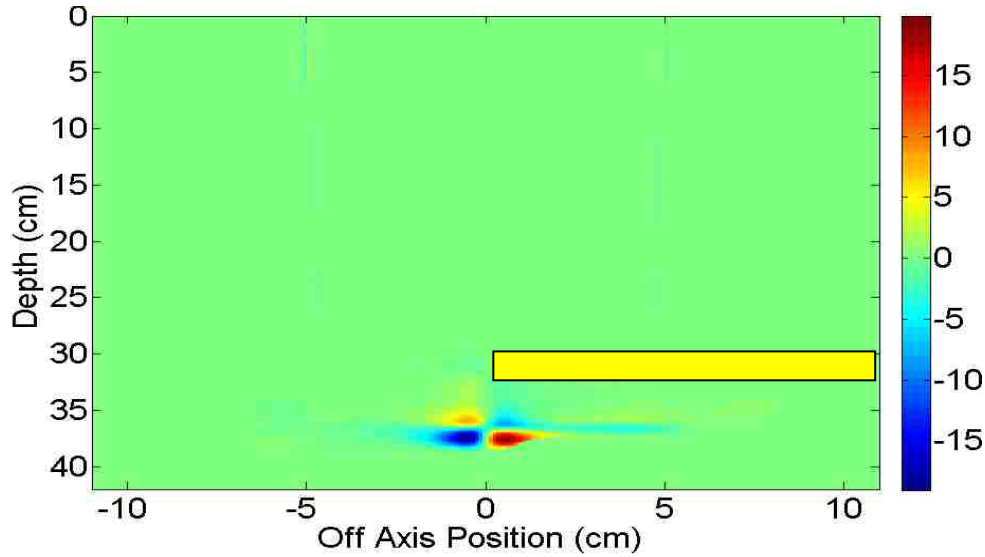

Figure 3.20: The 2D Monte Carlo dose distribution subtracted from the 2D PBA dose distribution for the geometry in Figure 3.19. This illustrates hot and cold spots created by the central axis approximation. Color bar shows the difference between MC and the PBA relative to the maximum dose in a flat water phantom.

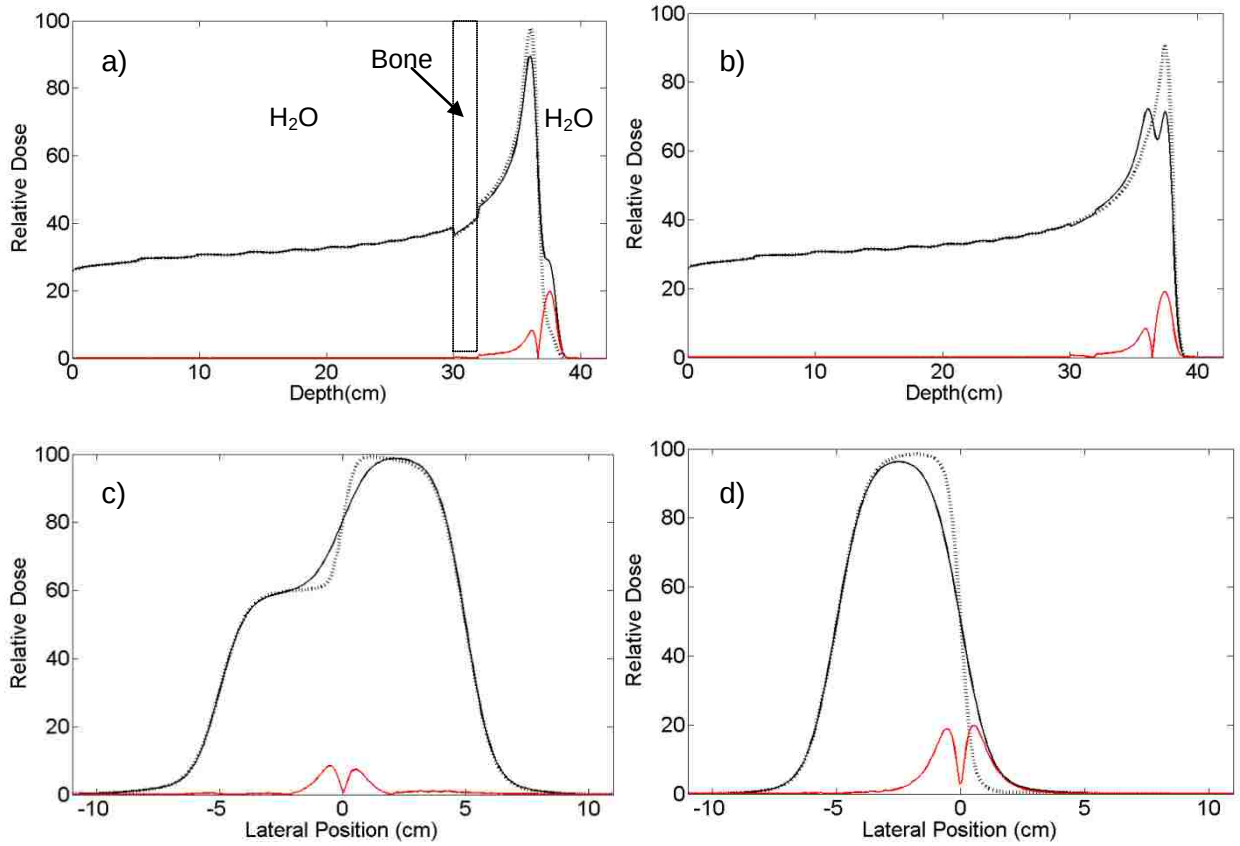

Figure 3.21: Profiles taken through the four failing regions of the geometry shown in Figure 3.19. Figures a) and b) are depth dose profiles taken at X = 0.55 cm and – 0.55 cm respectively. Figures c) and d) are lateral profiles taken at Z= 35.95 cm and 37.55 cm respectively. The Monte Carlo data (dashed lines) was plotted with the PBA data (solid lines). The absolute value of the difference between the two was plotted as well (red line). In all four profiles one can see the hot and cold spots caused by the central axis approximation.

To summarize, for water phantoms containing a 2 cm thick laterally finite compact bone slab at varying depths the PBA was unable to model perturbations due to the sharp lateral edge of the slab. This led to the appearance of two hot spots and two cold spots distal to the heterogeneity. The maximum errors caused by this were between ±4% and ±20% depending on the depth of the heterogeneity. The mean errors caused by this were between ±2% and ±10%. These errors could be of clinical significance and should be kept in mind when treating areas with sharp lateral edges in the beam. It should also be noted that when the compact bone slab was located in the first 50% of the range these errors were significantly reduced. Thus if it is possible one should try to avoid treating in areas sharp lateral edges located at deep depths.

For water phantoms containing a laterally finite 2 cm thick air slab greater than 96.15% of PBA dose calculation points were within 2% or 1 mm of Monte Carlo. For slabs located in the first 50% of the range the error from the central axis approximation was small (~1-3%) and 99% of dose calculation points were within the criteria of Monte Carlo. Similar to the compact bone slab results, this error increased significantly (~ 10-20%) when the slab was placed in the second half of the proton's range. The percentage of dose calculation points within 2% or 1 mm of Monte Carlo can be seen in Table 3.3.

Figure 3.22 shows the isodose comparison for a 250 MeV 10 x 10 cm^2 beam incident on a water phantom with a 2 cm thick laterally finite air slab located at 30 cm depth. Figure 3.23 shows the 2D dose difference distribution for this geometry. Similar to the compact bone simulation (Figure 3.19), these laterally finite slabs caused errors due to the central axis approximation. The errors look nearly identical to the ones caused by the bone slab (Figure 3.20) but the locations of the hot and cold spots are switched. The magnitudes of the errors are similar as well. The pass rate was slightly lower for the air slab at 97.96% compared to 98.60% for the bone. This was probably due to the presence of the regions of failure located at the edge of the air slab caused by the central axis approximation. This error was present in the compact bone simulations, but since the mass stopping power ratio is about 3-5% lower for air than compact bone, it caused a failure in this case, were it did not in compact bone. The maximum dose difference with the air slab present was 17.75% compared to 19.88% for bone and the mean dose difference in the failing region was 6.42% compared to 7.25%. This was most likely due to the air slab having a smaller effect on scatter than the compact bone slab. There was an overestimation of the dose in and after the laterally finite air slab, as seen in the laterally infinite air slabs in section 3.2.2. This was most likely due to perturbations of the secondary proton fluence caused by the air slab not modeled by the PBA.

Like the laterally finite compact bone geometries, geometries containing laterally finite air slabs displayed similar errors for all energies and field sizes with the magnitude of the errors

increasing with increasing depth of the heterogeneity. As field size increased, there was a decrease in the magnitude of the errors due to the increased number of pencil beams far off axis, where the central axis approximation was almost valid. For the larger field size, there were more of these pencil beams and this slightly decreased the magnitude of the error by 1-2%. For a heterogeneity located at a given percentage of the range, the errors generally increased with increasing energy as expected. This was due to higher energies having a larger lateral spread at a given percentage of their range. A full summary of the pass rate results can be seen in Table 3.4.

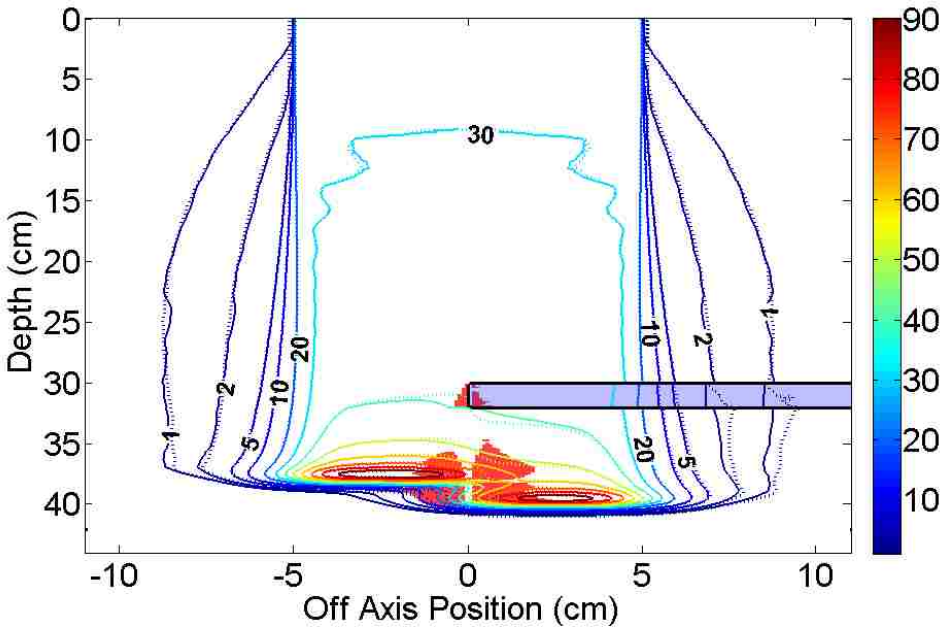

Figure 3.22: Isodose comparisons between Monte Carlo (dashed lines) and PBA (solid lines) for a 250 MeV 10 x10 cm^2 beam incident on a water phantom containing 2 cm air slab (blue) located at 30 cm. (Pass rate: 97.96%, Max DD: 17.75%, Mean DD: 6.42%). The red pixels indicate failing points.

To summarize, for water phantoms containing a 2 cm thick laterally finite air slab placed at varying depths, the PBA was unable to model perturbations due to the sharp lateral edge of the slab. This led to the appearance of two hot spots and two cold spots distal to the heterogeneity. The maximum errors caused by this were approximately between ±3% and ±19% depending on the depth of the heterogeneity. The mean errors caused by this were between ±1% and ±10%. These errors could be of clinical significance and should be kept in mind when treating areas

containing heterogeneities with sharp lateral edges in the beam. It should also be noted that when the air slab was located in the first 50% of the range these errors were significantly reduced. Thus, if it is possible one should try to avoid treating in areas sharp lateral edges located at deep depths.

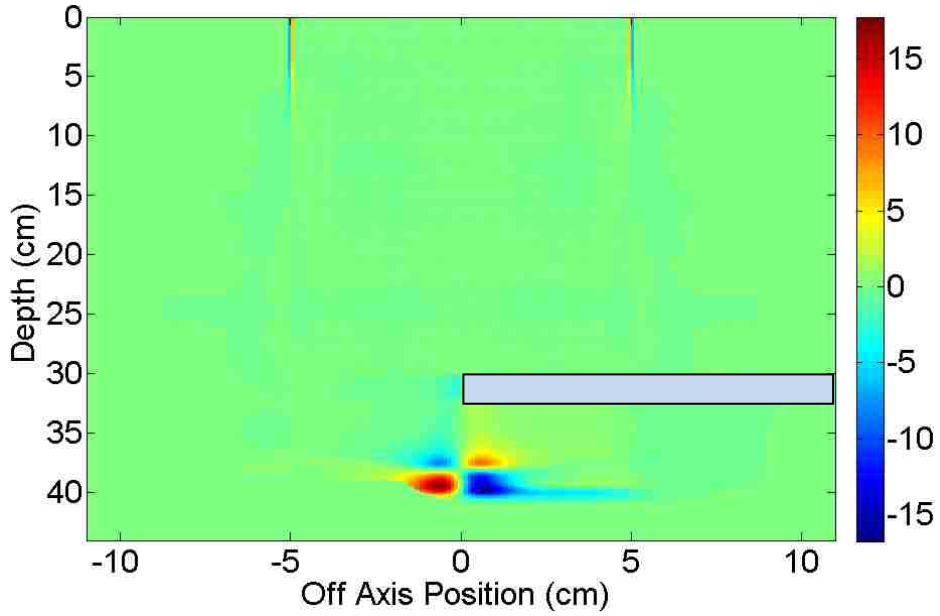

Figure 3.23: The 2D Monte Carlo dose distribution subtracted from the 2D PBA dose distribution for the geometry in Figure 3.22. This illustrates hot and cold spots created by the central axis approximation.

To summarize, for water phantoms containing a 2 cm thick laterally finite air slab placed at varying depths, the PBA was unable to model perturbations due to the sharp lateral edge of the slab. This led to the appearance of two hot spots and two cold spots distal to the heterogeneity. The maximum errors caused by this were approximately between ±3% and ±19% depending on the depth of the heterogeneity. The mean errors caused by this were between ±1% and ±10%. These errors could be of clinical significance and should be kept in mind when treating areas containing heterogeneities with sharp lateral edges in the beam. It should also be noted that when the air slab was located in the first 50% of the range these errors were significantly reduced. Thus, if it is possible one should try to avoid treating in areas sharp lateral edges located at deep depths.

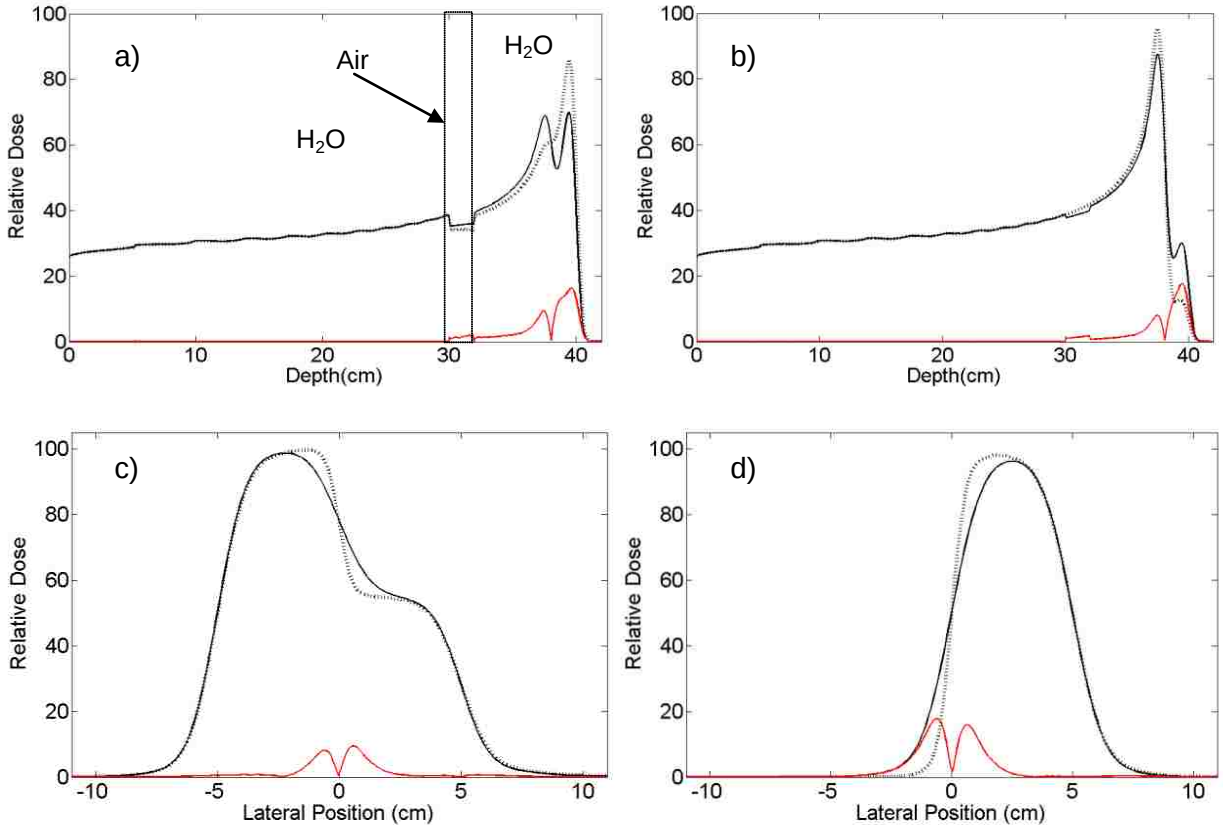

Figure 3.24: Profiles taken through the four failing H_2O regions of the geometry shown in Figure 3.19. Figures a and b are depth dose profiles taken at X = 0.55 cm and – 0.55 cm, respectively. Figures c and d are lateral profiles taken at Z= 37.45 cm and 39.45 cm, respectively. The Monte Carlo data (dashed lines) was plotted with the PBA data (solid lines). The absolute difference between the two was plotted as well (red line). In all four profiles one can see the hot and cold spots caused by the central axis approximation.

To summarize, for water phantoms containing a 2 cm thick laterally finite air slab placed at varying depths, the PBA was unable to model perturbations due to the sharp lateral edge of the slab. This led to the appearance of two hot spots and two cold spots distal to the heterogeneity. The maximum errors caused by this were approximately between ±3% and ±19% depending on the depth of the heterogeneity. The mean errors caused by this were between ±1% and ±10%. These errors could be of clinical significance and should be kept in mind when treating areas containing heterogeneities with sharp lateral edges in the beam. It should also be noted that when the air slab was located in the first 50% of the range these errors were significantly reduced. Thus, if it is possible one should try to avoid treating in areas sharp lateral edges located at deep depths.

Table 3.4: Summary of results of the percentage of PBA calculated dose points within 2% or 1 mm of Monte Carlo for water phantoms containing laterally infinite air and compact bone slabs.

Percentage of Pixels Within 2% or 1 mm:								
2 cm Compact Bone Slab								
	100 MeV		**150 MeV**		**200 MeV**		**250 MeV**	
	FS (cm^2)		**FS (cm^2)**		**FS (cm^2)**		**FS (cm^2)**	
Depth (cm)	**4x4**	**10x10**	**4x4**	**10x10**	**4x4**	**10x10**	**4x4**	**10x10**
2	99.85	99.93	99.95	99.97	99.83	99.91	100	100
5	98.93	99.56	99.74	99.89	99.85	99.91	99.81	99.88
10	n/a	n/a	95.76	98.24	99.39	99.62	99.80	99.84
15	n/a	n/a	n/a	n/a	97.61	98.66	99.37	99.79
30	n/a	n/a	n/a	n/a	n/a	n/a	97.61	98.60
2 cm Air Slab								
	100 MeV		**150 MeV**		**200 MeV**		**250 MeV**	
	FS (cm^2)		**FS (cm^2)**		**FS (cm^2)**		**FS (cm^2)**	
Depth (cm)	**4x4**	**10x10**	**4x4**	**10x10**	**4x4**	**10x10**	**4x4**	**10x10**
0	100	100	100	100	100	100	100	100
10	n/a	n/a	97.58	99.81	99.81	99.88	99.92	99.99
15	n/a	n/a	n/a	n/a	98.09	99.01	99.41	99.77
25	n/a	n/a	n/a	n/a	n/a	n/a	97.54	98.66
30	n/a	n/a	n/a	n/a	n/a	n/a	96.15	97.96

3.3 Summary of Results

Table 3.4 contains a summary of results from this study. The results of the 140 dose calculation comparisons were sorted into four groups: homogeneous water phantom, homogenous compact bone phantom, laterally infinite slab, and laterally finite slab data. The Last two groups were further split into subcategories based on what kind of heterogeneity was

present. For all of these groups, the mean pass rate, lowest pass rate, the maximum dose difference in the region of failure, and the mean dose difference in the region of failure of all the data sets in that group are reported. The dose difference values are relative to the maximum dose in a flat water phantom and were rounded up to the nearest half a percent.

Table 3.5: Summary of the results of this work. Note that the errors present in the laterally infinite slab geometries were also present in the laterally finite slab geometries. Note that (Total) is used to denote results containing both air and bone slabs.

Summary of Results										
Type of Heterogeneity		**Mean Percentage of Points within 2% of 1 mm**		**Minimum Percentage of Points within 2% or 1 mm**		**Maximum Dose Difference in Failing Region**		**Mean Dose Difference in Failing Regions**		**Cause of Errors**
Homogenous Water Phantoms		100%		100%		n/a		n/a		
Homogenous Compact Bone Phantom		99.5%		97.9%		±6.5%		±3%		Energy binning No material dependence in modeling non elastic collision
Laterally Infinite Slabs (Total)		99.8%		93.2%		±7%		±2.5%		Same as above
Air Slabs	**Bone Slabs**	99.7%	99.9%	93.2%	99.5%	±7%	±6%	±2.5%	±3%	
Laterally Finite Slabs (Total)		99.4%		95.8%		±21%		±5%		The central axis approximation
Air Slabs	**Bone Slabs**	99.2%	99.4%	96.2%	95.8%	±20%	±21%	±4.5%	±5%	

These results show the improvements made to the algorithm provide superior agreement in all areas for water phantoms when compared to single and two termed algorithms. When dealing with laterally infinite heterogeneities, the PBA accurately predicts the lateral penumbra where other algorithms struggle. However, at times the PBA under or overestimates the central axis dose. These are relatively small errors, typically on the order of 2-4%, may be overcome in the future by implementing material dependence in range straggling and secondary particle

production models. In the presence of laterally finite slabs the PBA struggles. This was expected as the central axis approximation is a known limitation of pencil beam algorithms and convolution algorithms. These results display similar characteristics with results in literature (Hong 1996, Schaffner 1998, Syzmanowski 2002, Soukup 2005, and Ciangaru 2005).

Chapter 4: Conclusions

4.1 Study Summary

The three specific aims of this work were each successfully completed. An existing PBA was adapted for calculations in heterogeneous media and improvements to the nuclear halo model were completed. PBA dose calculations were compared to Monte Carlo dose calculations in over 140 different geometries. The hypothesis of this work was that: *a pencil beam algorithm can predict dose to a phantom containing heterogeneities delivered by a uniform parallel mono energetic proton beam within 2% dose difference or 1 mm distance to agreement of Monte Carlo simulated dose distribution of the same geometry for at least 97% of dose calculation points and this can be done for test geometries including bone and air heterogeneities of different sizes placed at different depths, using four different energies (100, 150, 200, 250 MeV) and two field sizes (4 and 10 cm).* The hypothesis was found to be false. In four out of one hundred forty cases the PBA was not able to meet the 97% pass rate with the 2% or 1 mm criteria. In these cases the pass rates were 93.2%, 95.8%, 96.2%, and 96.7%.

4.1.1 Specific Aim 1: Modify the PBA to account for Heterogeneities.

The modification for calculation in heterogeneous media was accomplished through changes in the central axis term and the off axis terms of the PBA. The central axis term was modified by scaling the central axis depth dose input data at an effective depth by mass stopping power ratio. The PBA off axis distribution consisted of three terms. The primary term was a Gaussian calculated by using the differential Moliere scattering power within Fermi Eyges scattering theory. The primary term was material dependent by virtue of the material dependence in the scattering power and accounted for the position of the material by using Fermi Eyges scattering theory. The secondary term was Gaussian and the third term was based on the Cauchy

Lorentz distribution. Their widths and relative weights were determined from curve fits in water and therefore were not material dependent.

4.1.2 Specific Aim 2: Improve the Accuracy of the Nuclear Halo Model

The original halo model in the PBA consisted of a single Gaussian. It was found that it did not correctly model the off axis distribution of a proton pencil beam scattering in water. The addition of a third term based on the Cauchy Lorentz distribution was completed. The agreement in the low dose off axis region was improved greatly. Curve fits were performed to determine the relative weights and widths of the two halo terms for the four proton energies commissioned in the PBA.

4.1.3 Specific Aim 3: Evaluate the Accuracy of the Algorithm

The accuracy of the PBA was determined by performing 140 dose calculations using Monte Carlo methods and the PBA for four proton energies and two field sizes. This was done on phantoms containing different heterogeneities. It was found that at least 93% of PBA dose calculation points were within 2% of 1 mm distance to agreement of Monte Carlo. In all but four dose calculations at least 97% of the PBA dose calculations points were within the comparison criteria of Monte Carlo. Differences between the PBA and Monte Carlo were caused by differences in stopping powers, energy step size, the PBA's lack of material dependence in modeling non-elastic scatter, and the central axis approximation. These effects lead to errors ranging from approximately 2% to 21% of the maximum dose in a flat water phantom.

4.2 Recommendations to Improve the Algorithm and Possible Future Work

4.2.1 Extension of PBA to Patient Data

More realistic dose calculations will need to be conducted in the future. The development of a more realistic proton source and the use of spread out Bragg peaks or multiple beam spots to

deliver dose to more relevant treatment volumes will be needed when calculating dose on patient data. Development of a model of a passively scattered or scanned source will have to include energy and angular spread not included in this work. These developments could help determine the clinical relevance of some problems with PBA found in this work, such as how errors in individual pristine peaks of 3-6% translate when treating with a large spread out Bragg peak.

Key to future work is access to a proton facility, where a site specific proton source model could be produced. This would allow for the production of much more robust and realistic Monte Carlo and PBA models and would also allow for confirmation of the calculations with measurement.

If the PBA is going to continue to use Monte Carlo data as input, an update to MCNPX 2.7e or MCNP6 would allow for a more finely tuned Monte Carlo model and thus better input data. Improved control over energy step size and the number of sub steps could prove to solve some of the issues with differences in range seen in this work. Improvements in nuclear data tables would also allow for further refinements in the Monte Carlo model to made, such as more accurate transport of all secondary particles produced in non-elastic interactions.

4.2.2 The Nuclear Halo Correction

The current halo model parameters were determined from curve fits to Monte Carlo data. These parameters were stored as a function of depth and read in during the dose calculation and the proper parameters were determined by sampling these text files. This has proven to be somewhat time consuming and it could prove valuable to parameterize the halo terms as a function of depth. This may require a little smoothing of the fit parameters or perhaps a higher resolution fit, but once this was accomplished, it could prove very helpful in the future.

The current nuclear halo correction was shown to be very accurate in water. However, it was also shown to be vulnerable to changes in material. The PBA was unable to model changes in

the distribution of secondary protons due to changes in material, which proved to be a significant problem for small field size high energy beams. The development of a first principles model that can account for these material changes would be ideal. If this cannot be accomplished, a material dependent scaling method could be done in manner similar to what was done for the central axis. Scaling by the ratio of non elastic cross section in the material relative to water could also be used to help accommodate for the changes in dose from secondary particles that are due to changes in material.

4.2.3 Patient Calculation & TPS Integration

Finally once those tasks are accomplished the future integration of CT data based dose calculation would provide the test in the environment that the PBA would eventually be used in. At the end of the project the success of the algorithm will depend on how it dose when calculating dose to patients, not water cylinders containing rectangular bone and air slabs. All of these developments will bring the PBA closer and closer to full 3D dose calculations on CT data sets. Once this has been accomplished the true merit of PBA will be determined.

4.2.4 The Central Axis Approximation

The preliminary results in this work have revealed some of the underlying issues that will be faced in the future. The central axis approximation caused by far the largest errors in this work and was the only error that cannot be overcome with refinement in the PBA. In many cases this approximation may not have a large effect but it must be kept in mind just as it is when treating with electrons. Similar to work done by Shiu and Hogstrom (1991) and Boyd (2001) in electron transport, the development of a proton pencil beam redefinition algorithm (PBRA) should reduce the errors caused by this approximation.

References

Berger, M.J. "Monte Carlo calculation of the penetration and diffusion of fast charged particles." Meth. Comp. Phys., 1, (1963) 135-215.

Berger M.J., J.S. Coursey, M.A. Zucker and J. Chang. P-Star: Stopping-power and range tables for protons. Physics.nist.gov. Nation Institute of Standards and Technology; Oct 1998 Web.

Boyd, R. A., K. R. Hogstrom, and G. Starkschall, "Electron pencil-beam redefinition algorithm dose calculations in the presence of heterogeneities." Med. Phys. 28, (2001): 2096–2104.

Chadwick et al. "Nuclear Data for Neutron and Proton Radiotherapy and for Radiation Protection." *ICRU Report 63 (*2000).

Chapman, John. "Proton beam dose calculations for Homogeneous media." MS Thesis Louisiana State University, 2012. Print.

Chen N, Y-J. .High Gradient Dielectric Wall Accelerators. In: CHEN, Y.-J., ed. Muon Collider Design Workshop, 2008 Thomas Jefferson National Laboratory.

Chu W.T., B.A. Ludewigt, and T.R. Renner. "Instrumentation for treatment of cancer using proton and light-ion beams." Rev. Sci. Instrum., 64 (1993): 2055-2122.

Ciangarui, George, Jerimy C. Polf, Martin Bues, and Alfred Smith. "Benchmarking analytical calculations of proton doses in heterogeneous matter." Med. Phys. 32.12 (2005): 3511-3523. Print.

Fontenot, Jonas, A K Lee, W. D. Newhauser "Risk of Secondary Malignant Neoplasms From Proton Therapy and Intensity-Modulated X-Ray Therapy for Early-Stage Prostate Cancer" IJROBP, Vol 74, Issue 2, 1 June 2009, 616-622. Print

Gottschalk, Bernard, "On the scattering power of radiotherapy protons." Med. Phys.37(1) Jan (2010): 352-367.Print.

Gottschalk, Bernard, "Passive Beam Spreading in Proton Radiation Therapy." Unpublished book (2004). Available at http://physics.harvard.edu/~gottschalk.

Gottschalk, Bernard, A.M. Koehler, R.J. Schneider, J.M. Sisterson, and M.S. Wagner "Mulitple Coulomb scattering of 160 MeV protons.." Nuclear Instruments and Methods in Physics Research B74 (1993): 476-490. Print.

Gupta, Mukund "Calculation of radiation length in Materials." Cdsweb.cern.ch. European Organization for Nuclear Research; Jul 2010 Web.

Herault J, N Iborra, B Serrano, and P Chauvel. "Spread-out Bragg peak and monitor unit calculation with the Monte Carlo code MCNPX."Med. Phys. 34(2) (2007): 680-688. Print.

Hogstrom, Kenneth R, "Notes on the derivation of pencil beam dose distributions for therapeutic electron beams." (1991): 1-34.Print.

Hogstrom, Kenneth R, Micheal D Mills, and Peter R Almond. "Electron beam dose calculations." Phys.Med. Biol. 26.3 (1981): 445-459. Print.

Hong, Linda, Michael Goitein, Marta Bucciolini, Robert Comiskey, Bernard Gottschalk, Skip Rosenthal, Chris Serago, and Marcia Urie. "A pencil beam algorithm for proton dose calculations." Phys.Med. Biol. 41 (1996): 1305-1330. Print.

Kahn, Fiaz M. The Physics of Radiation Therapy Fourth Edition. Philadelphia, PA: Lippincott Williams & Wilkins, (2010). Print.

Mancuso, G. M. "Evaluation of Volumetric Modulated Arc Therapy (VMAT) Patient Specific Quality Assurance." MS Thesis Louisiana State University (2011). Available at http://etd.uis.lsu.edu/cgi-bin/ETD-browse/browse.

MCNPX, "MCNPX 2.7 user's manual" (2011). *Los Alamos National Laboratory,* Los Alamos, NM.

Newhauser, W, N Koch, S Hummel, M Ziegler, and U Titt. "Monte Carlo simulations of a nozzle for the treatment of ocular tumors with high-energy proton beams." Phys. Med. Biol. 50 (2005) 5229-5249. Print.

Pedroni, E, S Scheib, T Bohringer, A Coray, M Grossmann, S Lin, and A Lomax. "Experimental characterization and physical modeling of the dose distribution of scanned proton pencil beams." Phys.Med. Biol. 50 (2005): 541-561. Print.

PTCOG, 2012. Particle therapy facilities in operation. [Online] Available at: http://ptcog.web.psi.ch/ptcentres.html [Accessed 30 January 2010].

Schaffner, Barbara, Eros Pedroni, and Antony Lomax. "Dose calculation models for proton treatment planning using dynamic beam delivery system: an attempt to include heterogeneity effects in the analytical dose calculation." Phys.Med. Biol. 44 (1999) 27-41. Print.

Schaffner, Barbara. "Proton dose calculation algorithms and configuration data." PTCOG 46-Education workshop May 20, (2007).

Schaffner, Barbara and Eros Pedroni. " The precision of proton range calculations in proton radiotherapy treatment planning: experimental verification of the relation between CT-HU and proton stopping power." Phys.Med. Biol. 43 (1998) 1579-1592. Print.

Shiu A.S. and Hogstrom K.R. "Pencil-beam redefinition for electron dose distributions." Med. Phys., 18(1) (1991): 7-18.

Smith, Alfred. "Vision 20/20: Proton therapy." Med. Phys 36.2 (2009) 556-568. Print.

Smith, Alfred, Micheal Gillian, Martin Bues, X. Ronald Zhu, Kazumichi Suzkim Radhe Mohan, Shiao Woo, Andrew Lee, Ritsko Komaki, and James Cox. "The M.D. Anderson proton therapy system." Med. Phys 36.9 (2009) 4068-4083. Print.

Soukup, Martin, Matthias Fippel, and Markus Alber. "A pencil beam algorithm for intensity modulated proton therapy derived from Monte Carlo simulations." Phys.Med. Biol. 50 (2005): 5089-5104. Print.

Szymanowski, Hanitra and Uwe Oelfke "Two-dimensional pencil beam scaling: an improved proton dose algorithm for heterogeneous media" Phys.Med. Biol. 47 (2002): 3313-3330. Print.

Titt, U, N Sahoo, X Ding, Y Zheng, W D Newhauser, X R Zhu, J C Polf, M T Gillin and R Mohan. "Assessment of the accuracy of an MCNPX-based Monte Carlo simulation model for predicting three-dimensional absorbed dose distributions." Phys. Med. Biol. 53 (2008): 4455 print.

Turner, James E. Atoms, Radiation, and Radiation Protection Second Edition Weinheim, Germany: Wiley-VCH Verlag GmbH & Co, (2004). Print.

Turner, James E. "Interaction of ionizing radiation with matter." Health Physics 86.3 March (2004): 228-252. Print.

Zheng Y, Newhauser WD, Fontenot JD, Koch N, and Mohan R. "Monte Carlo simulation model of the M. D. Anderson Cancer Centers passively scattered proton therapy machine". J Nucl Matl 361, 289-297, (2007). Print.

Appendix A: Isodose Comparison Results

In this chapter all of the isodose comparisons of this work are displayed. The results are sorted by geometry type and energy. In each case, the 4 x 4 cm^2 results are displayed on the left side and the 10 x 10 cm^2 on the right. Each plot also has a tag number in the upper left hand of the graph. This number can be used to look up the geometry parameters, mean dose difference, max dose differences, and pass rate of that plot in Appendix B. In all of the plots the Monte Carlo dose distributions were contoured with the dashed lines and the PBA was contoured with solid lines. Each distribution was normalized to the maximum dose in a flat water phantom and the 1, 2, 5, 10, 20, 30, 40, 50, 60, 70, 80, 90, and 100 percent isodose lines were identified.

A1: Homogenous Water Phantom Results

100 MeV Results

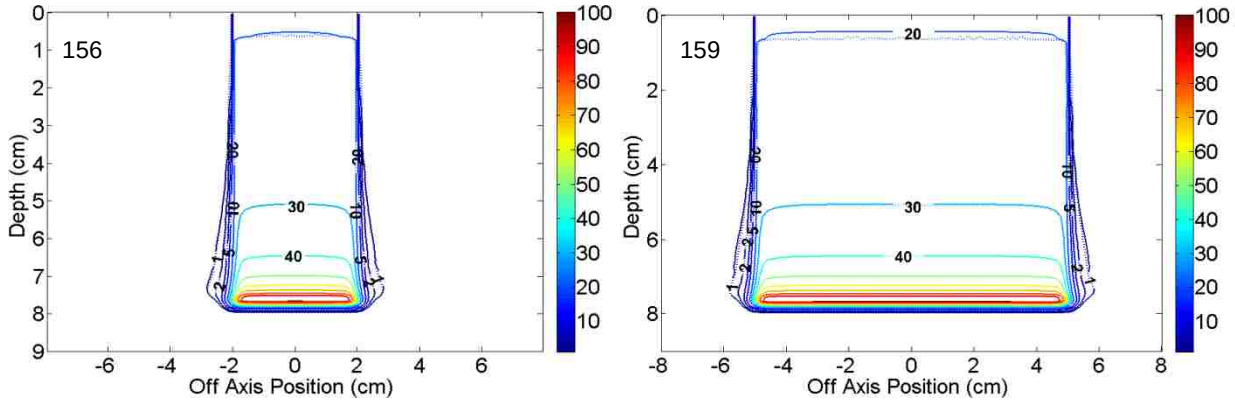

150 MeV Results

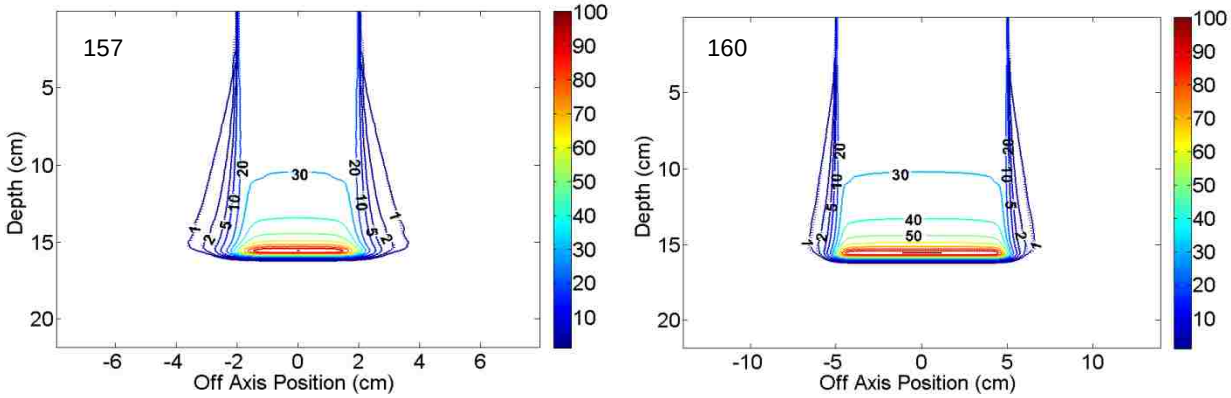

200 MeV Results

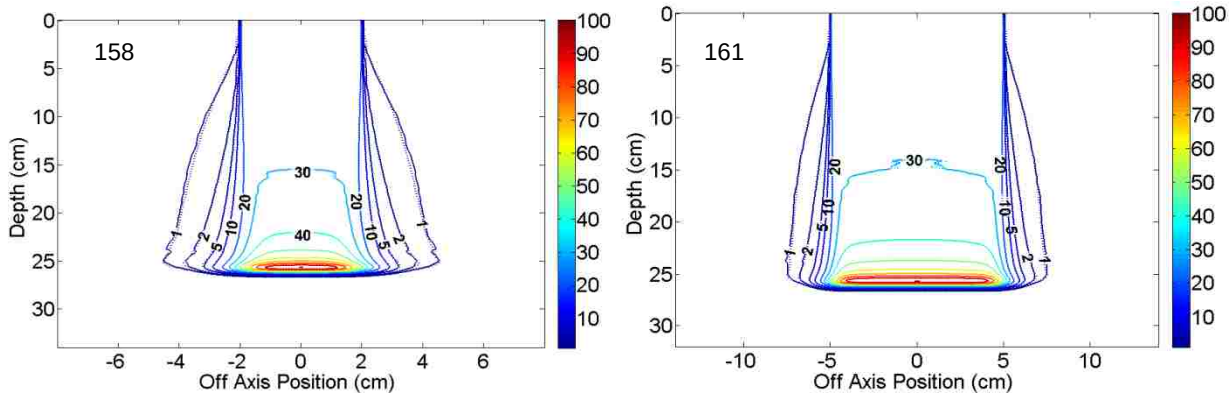

250 MeV Results

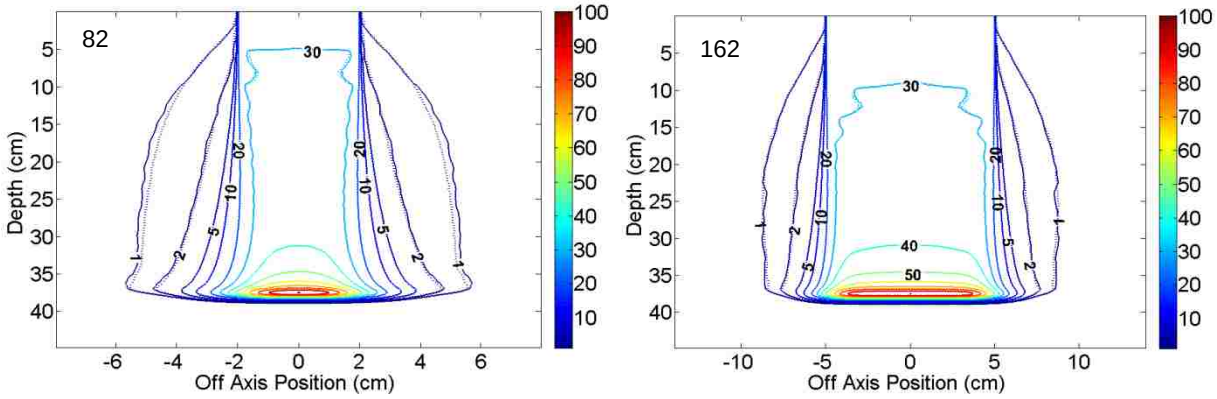

A2: Homogenous Compact Bone Phantom Results

100 MeV Results

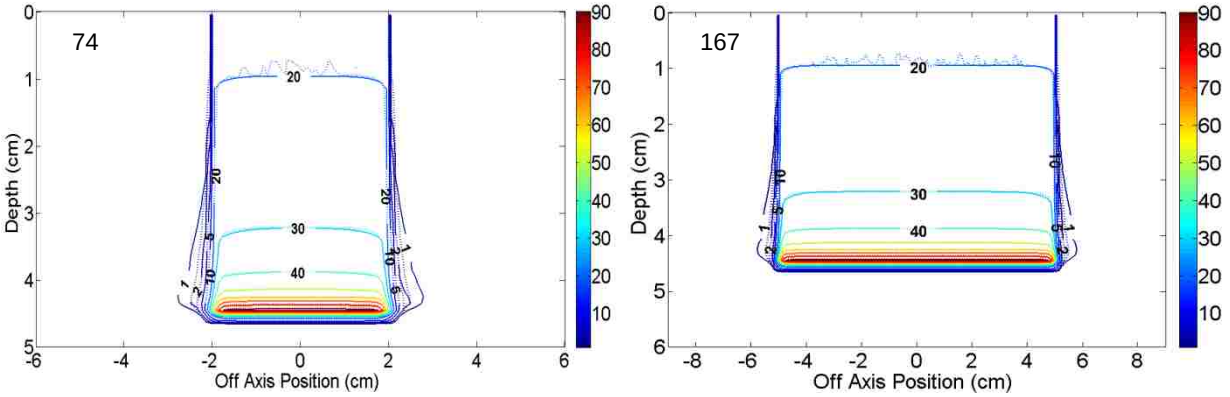

150 MeV Results

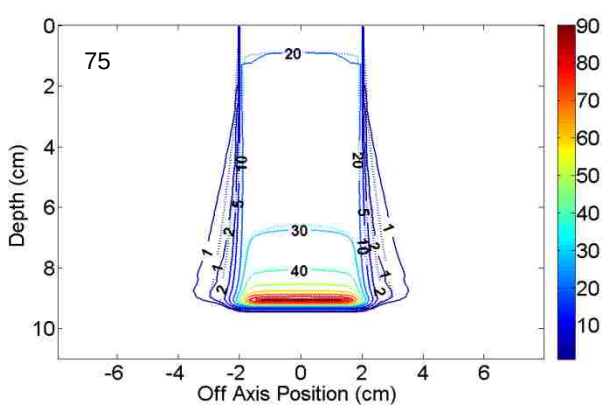

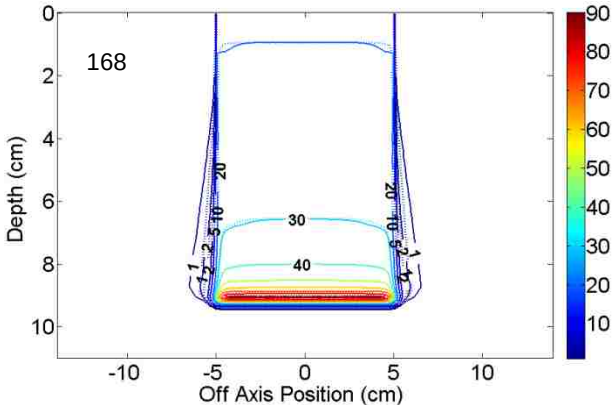

200 MeV Results

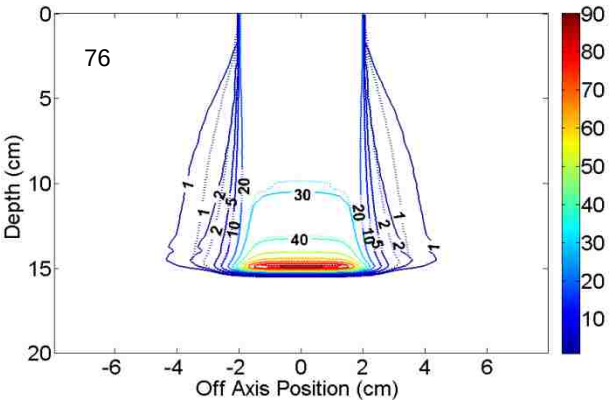

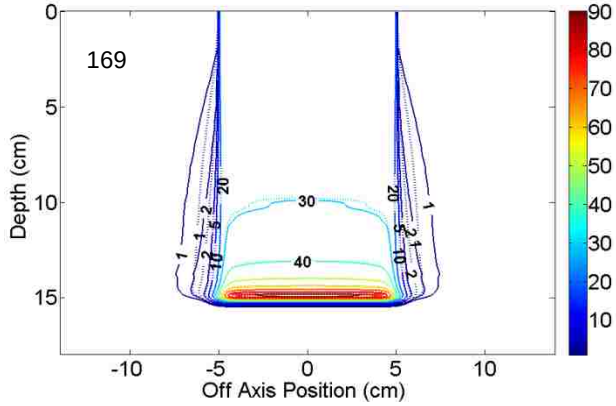

250 MeV Results

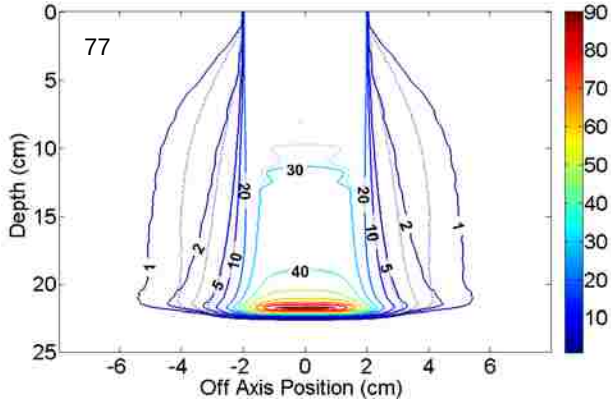

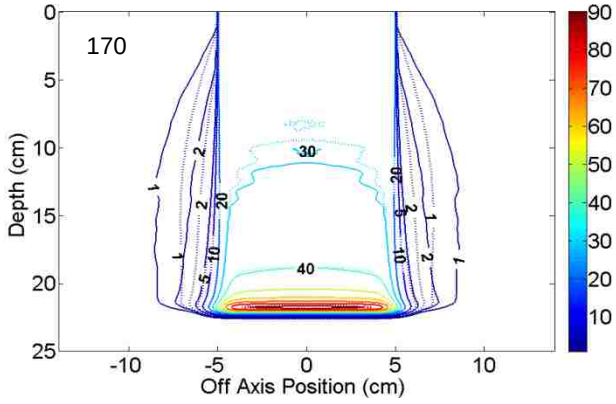

A3: Laterally Infinite Compact Bone Slab Results

100 MeV Results

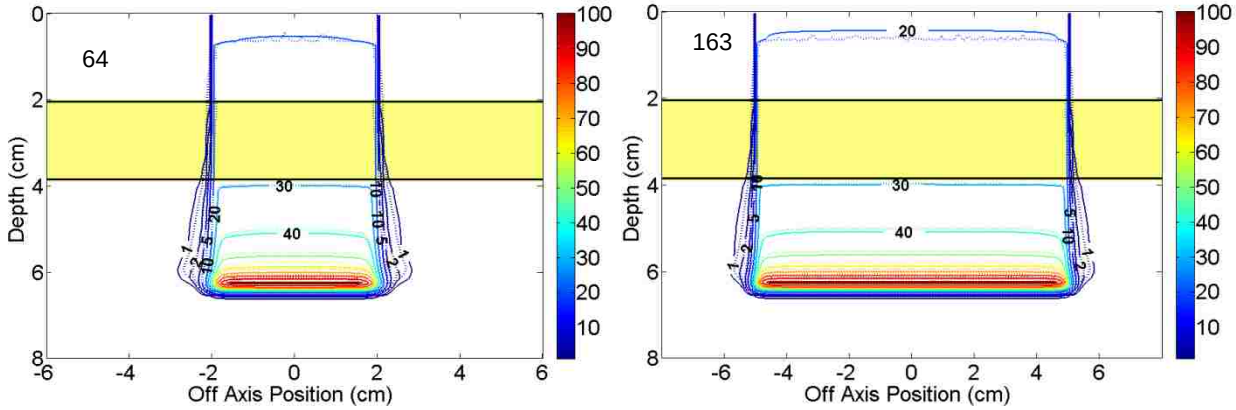

150 MeV Results

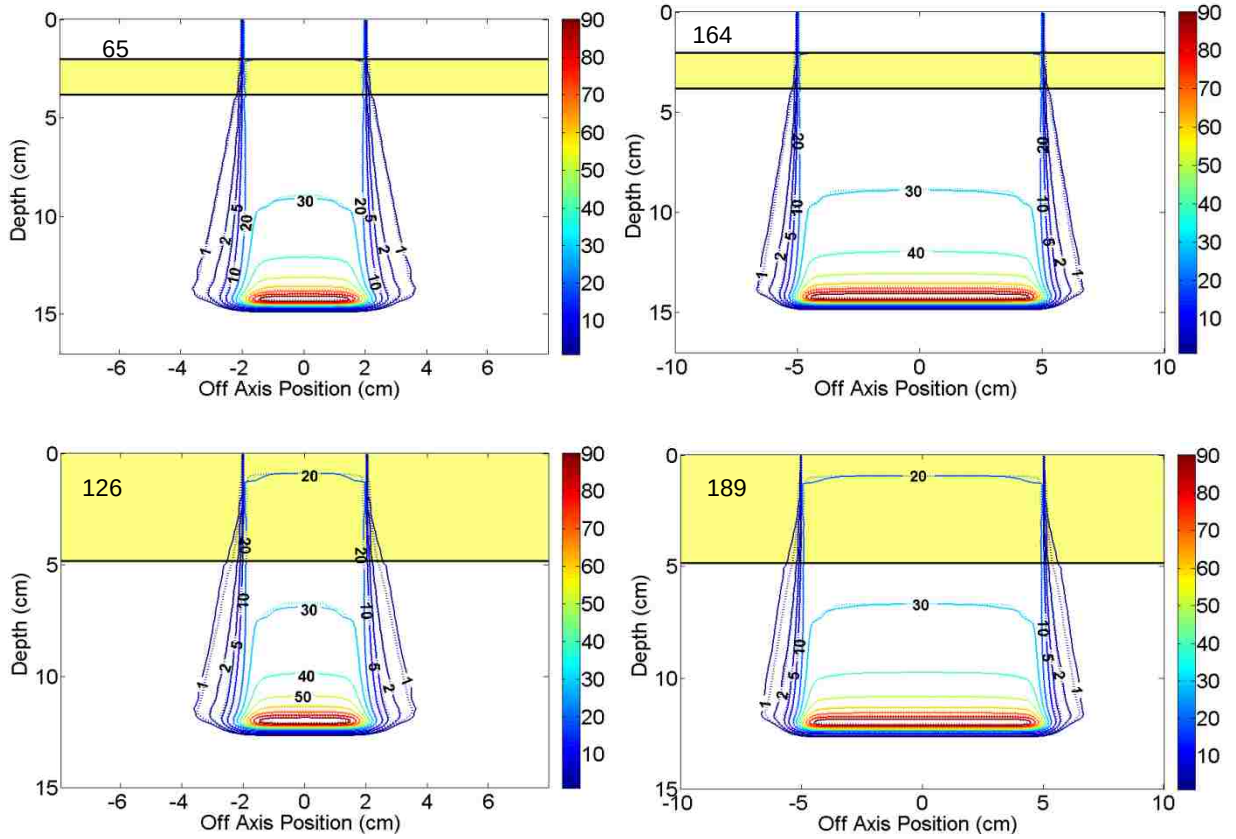

200 MeV Results

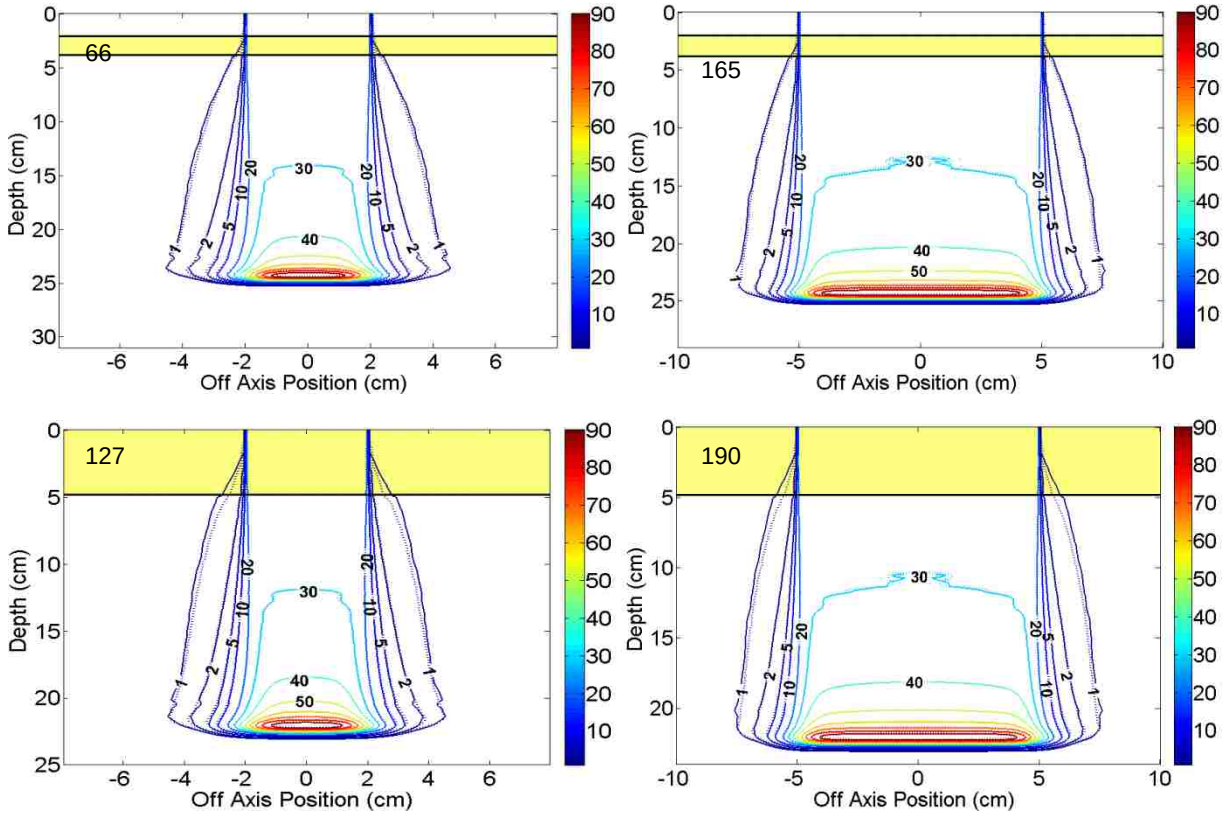

250 MeV Results

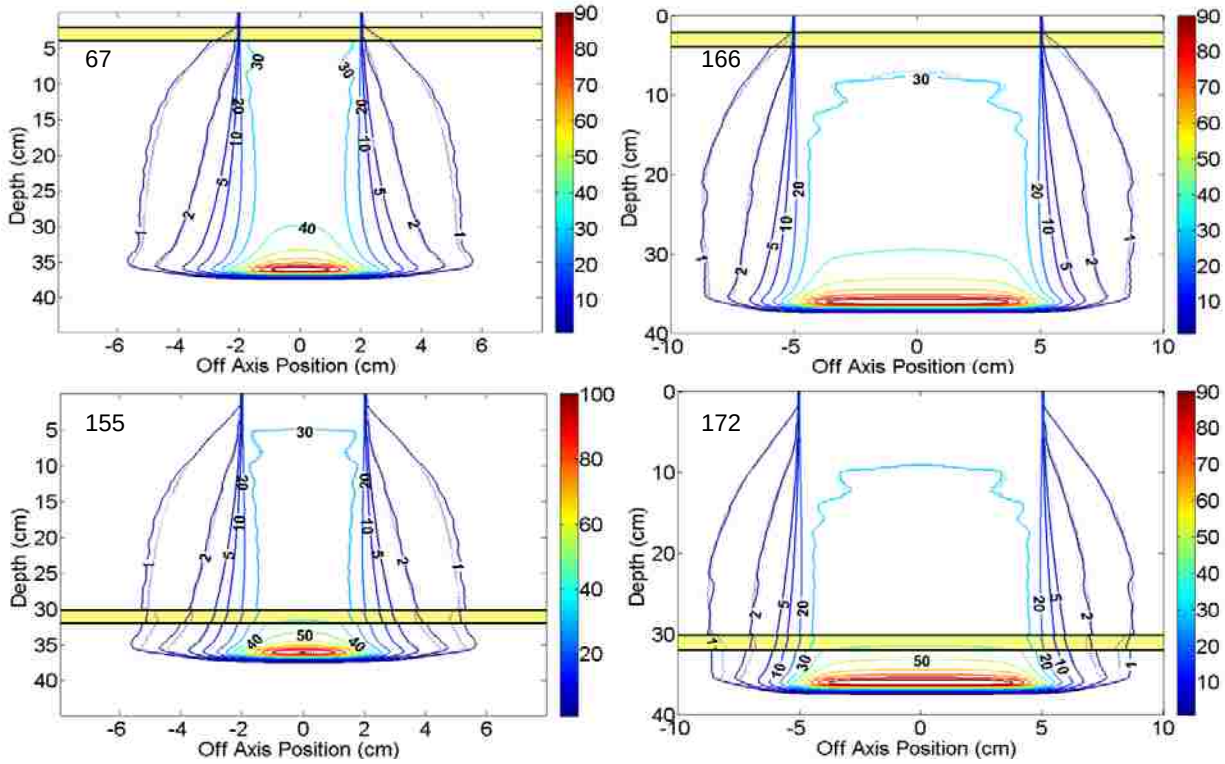

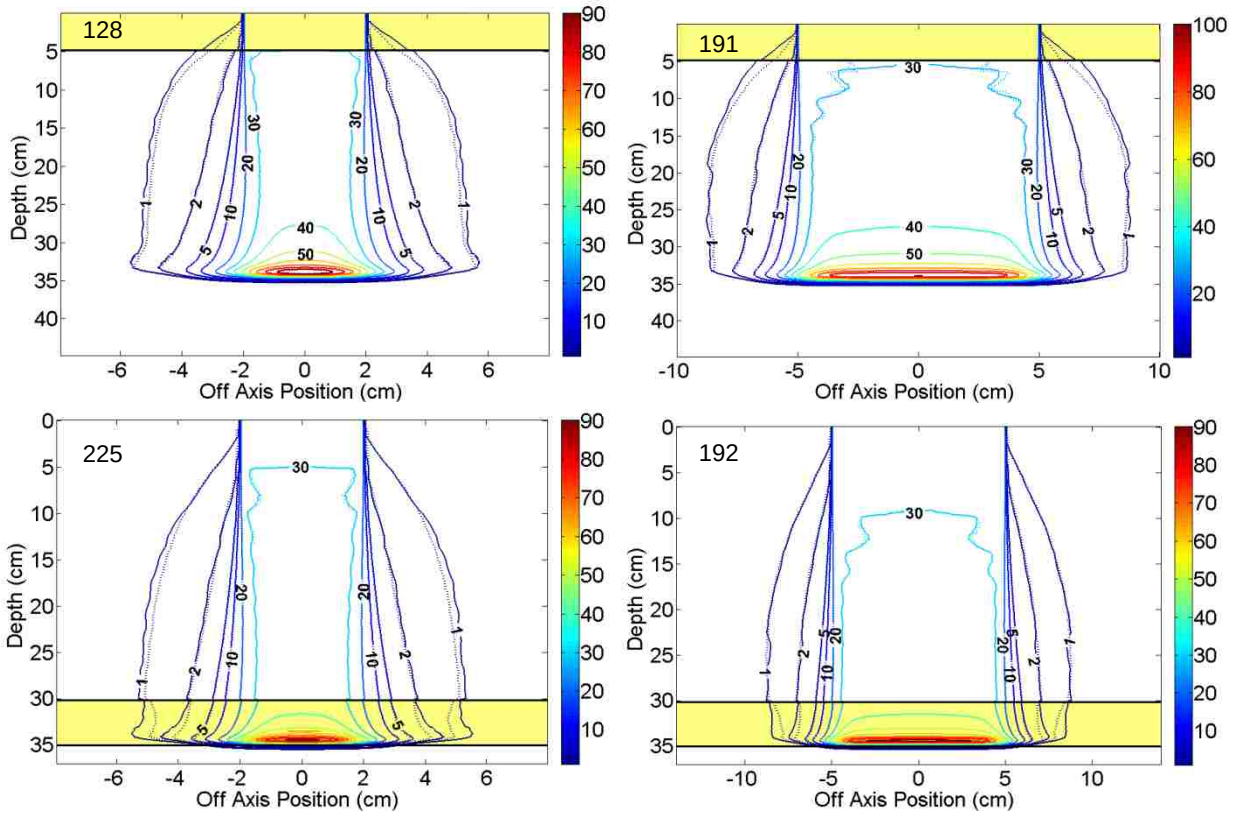

A4: Laterally Infinite Air Slab Results

100 MeV Results

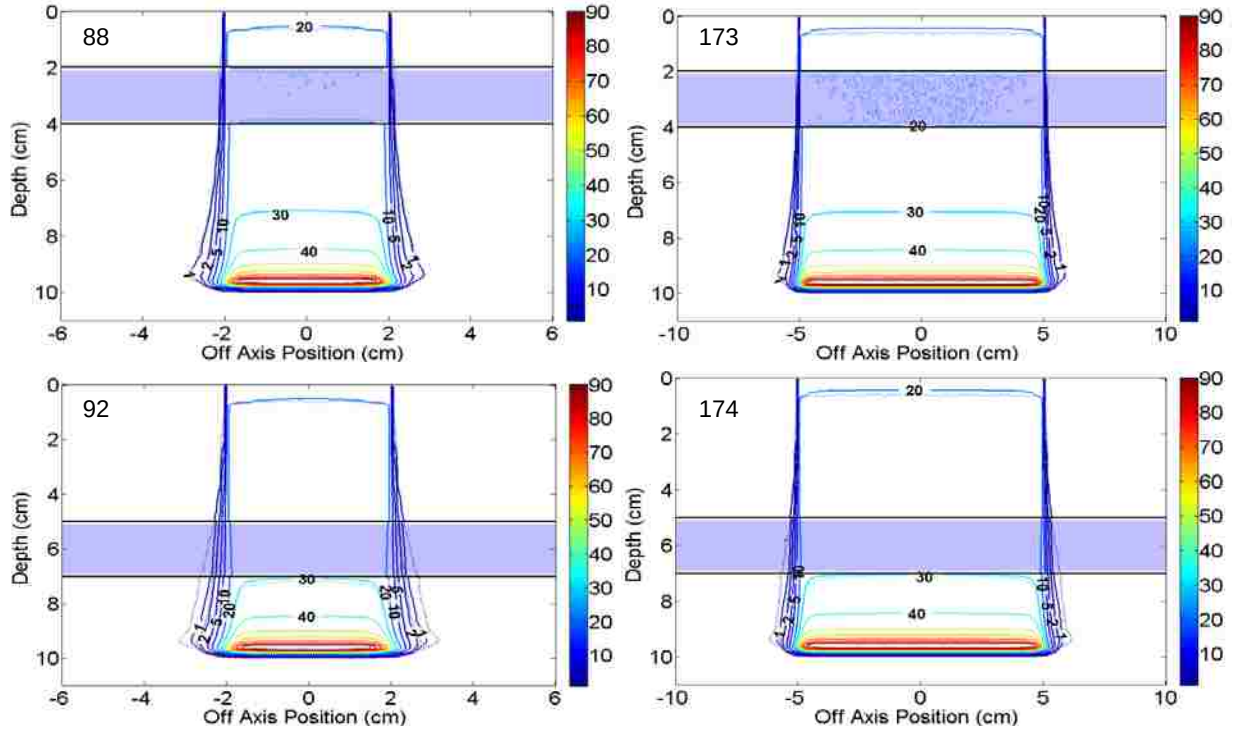

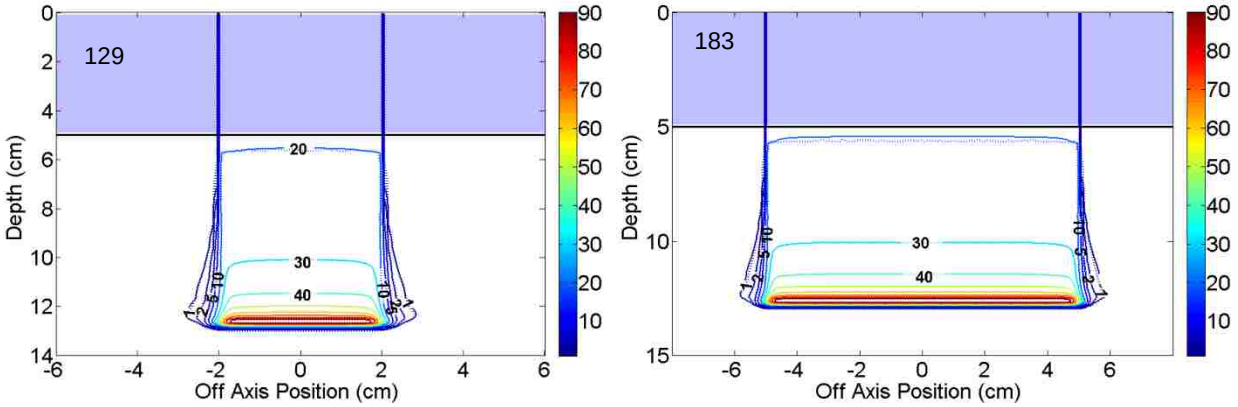

150 MeV Results

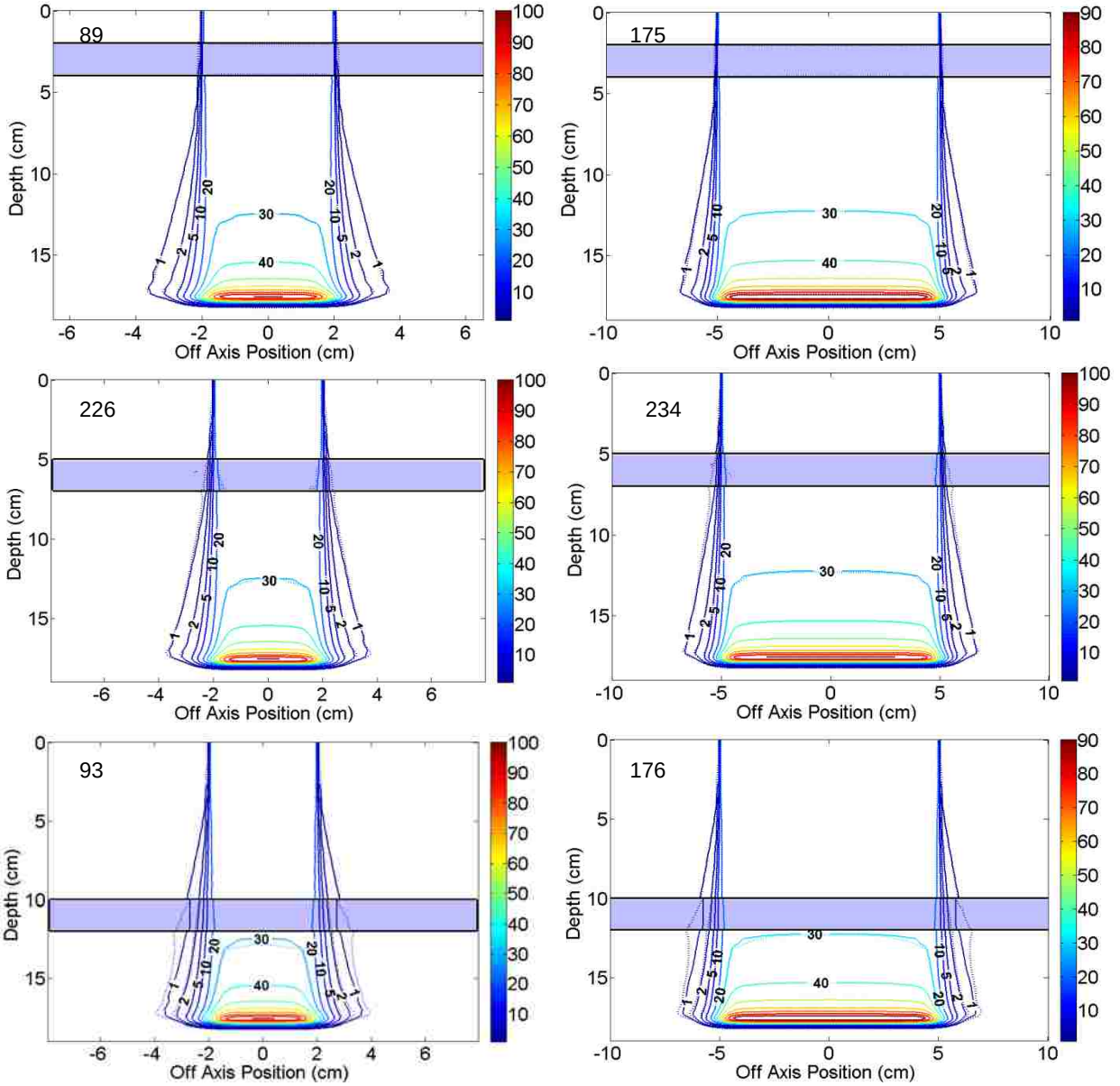

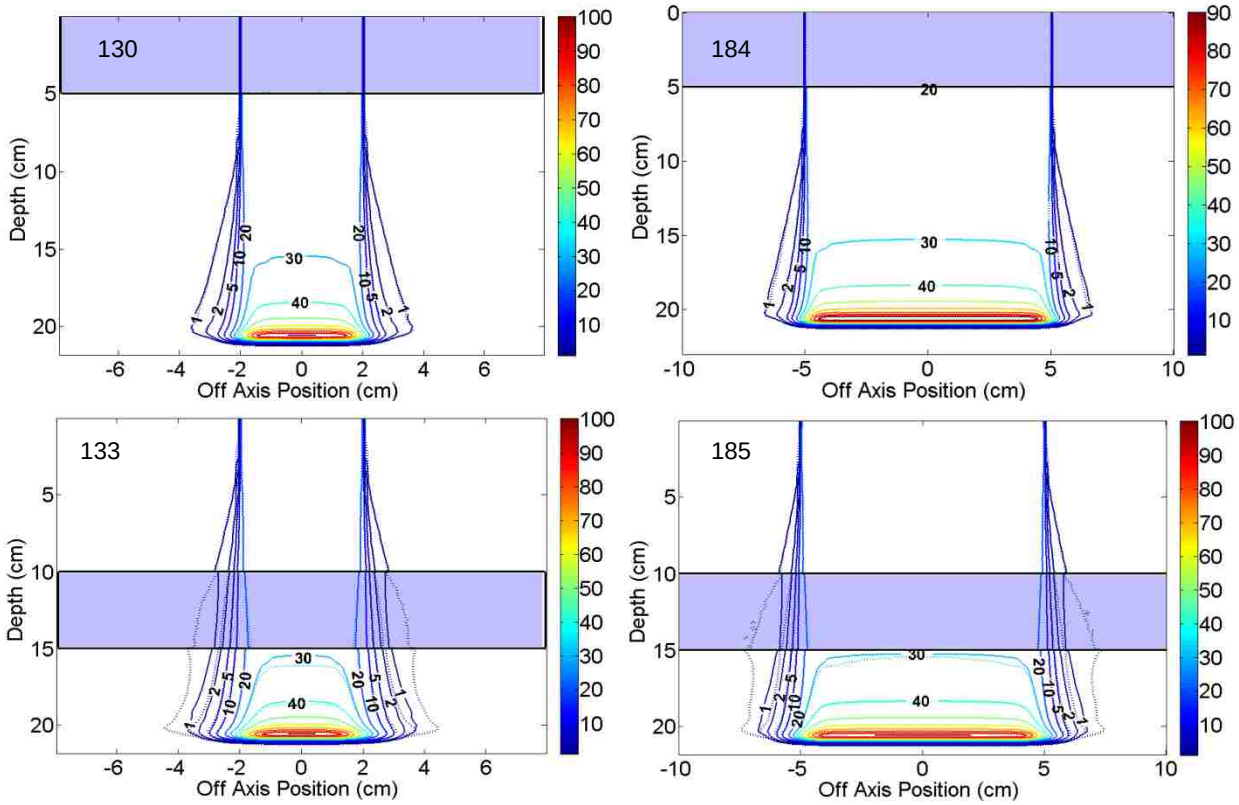

200 MeV Results

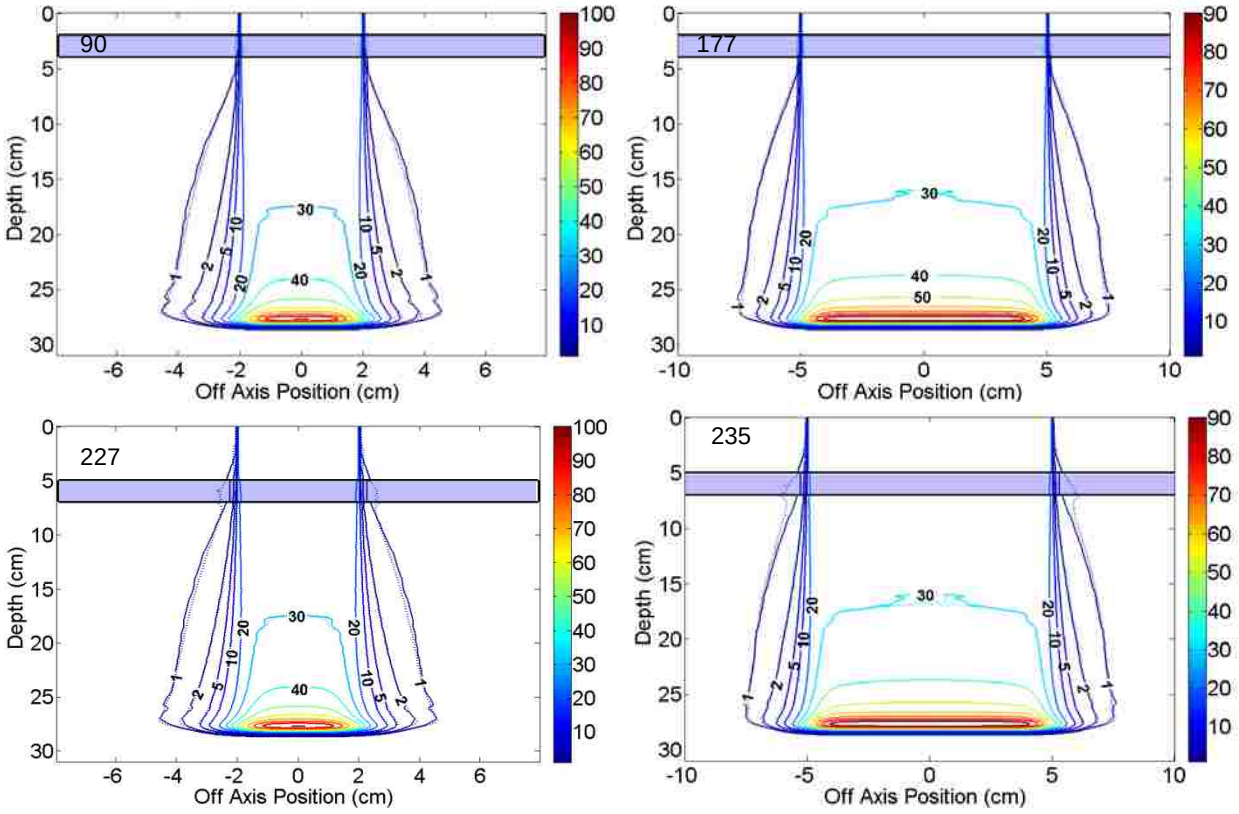

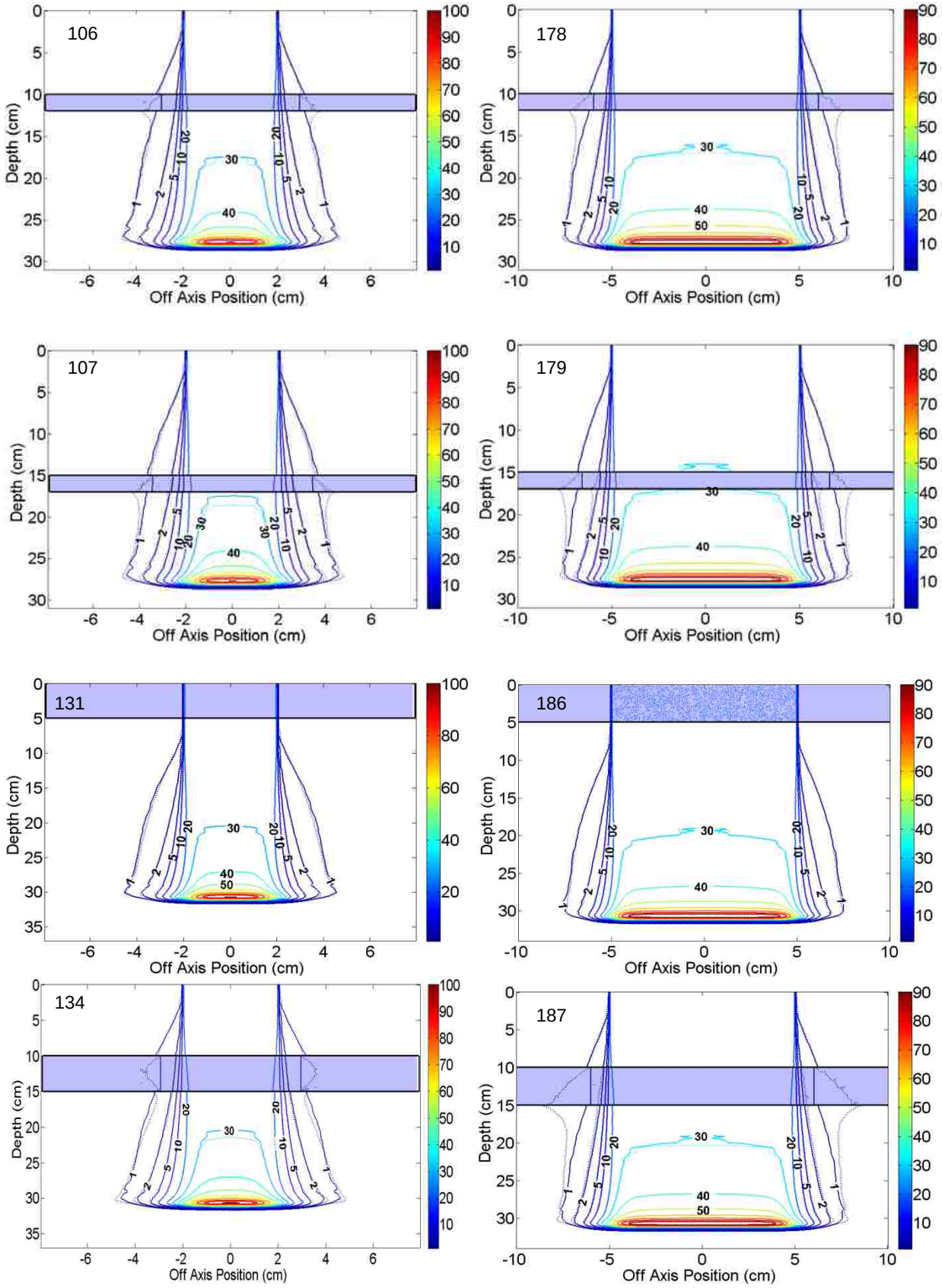
106
178
107
179
131
186
134
187
Depth (cm)
Off Axis Position (cm)

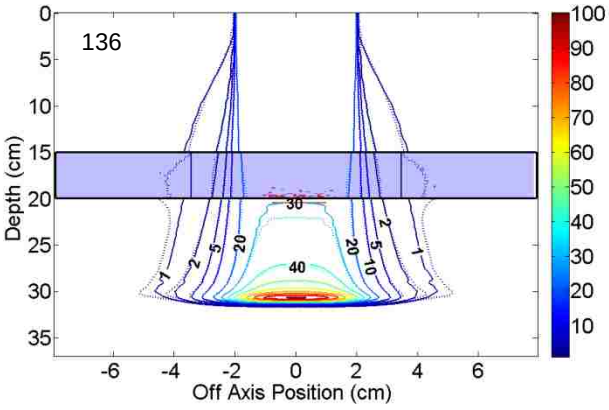

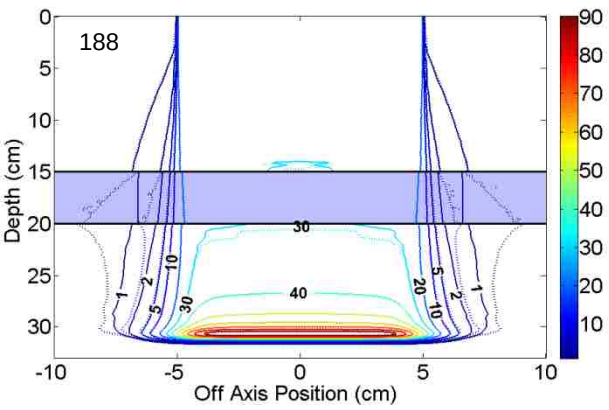

250 MeV Results

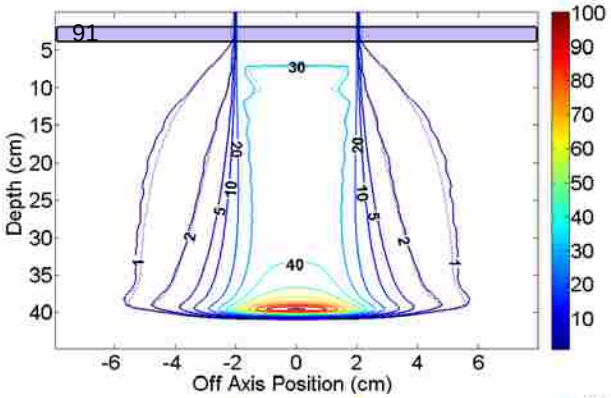

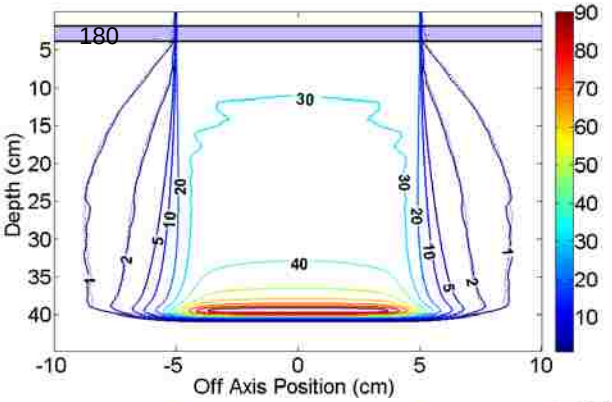

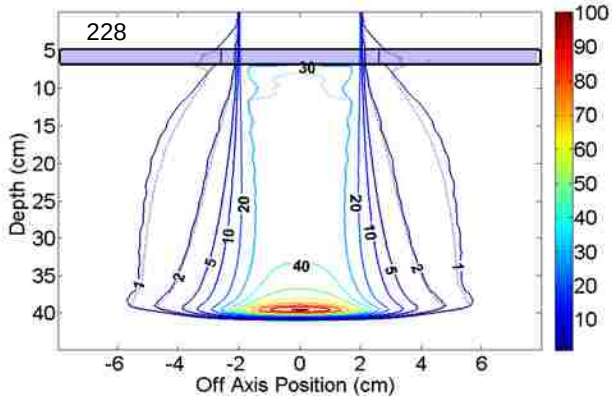

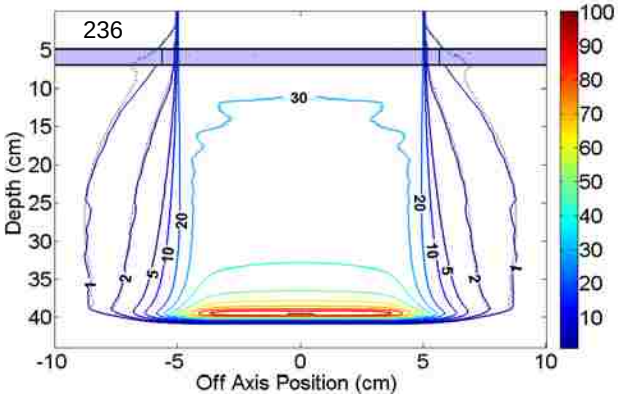

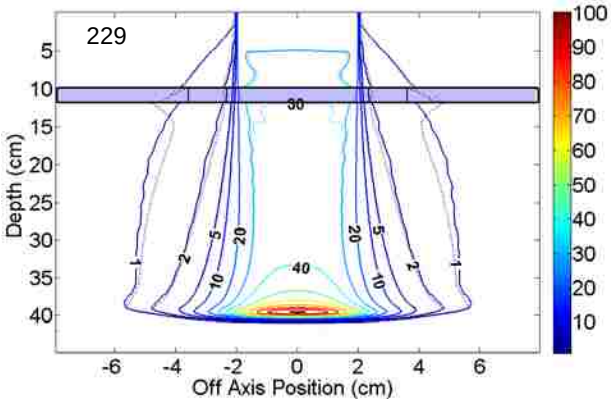

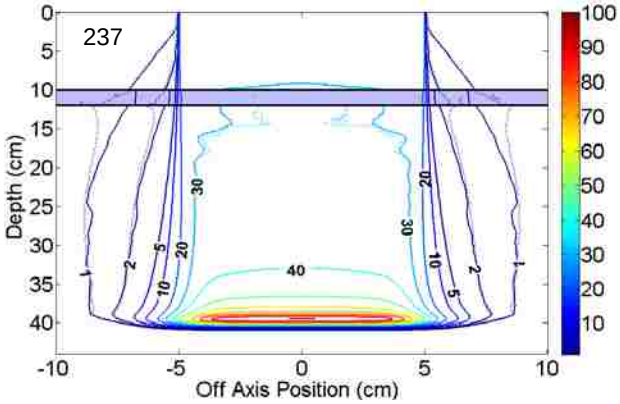

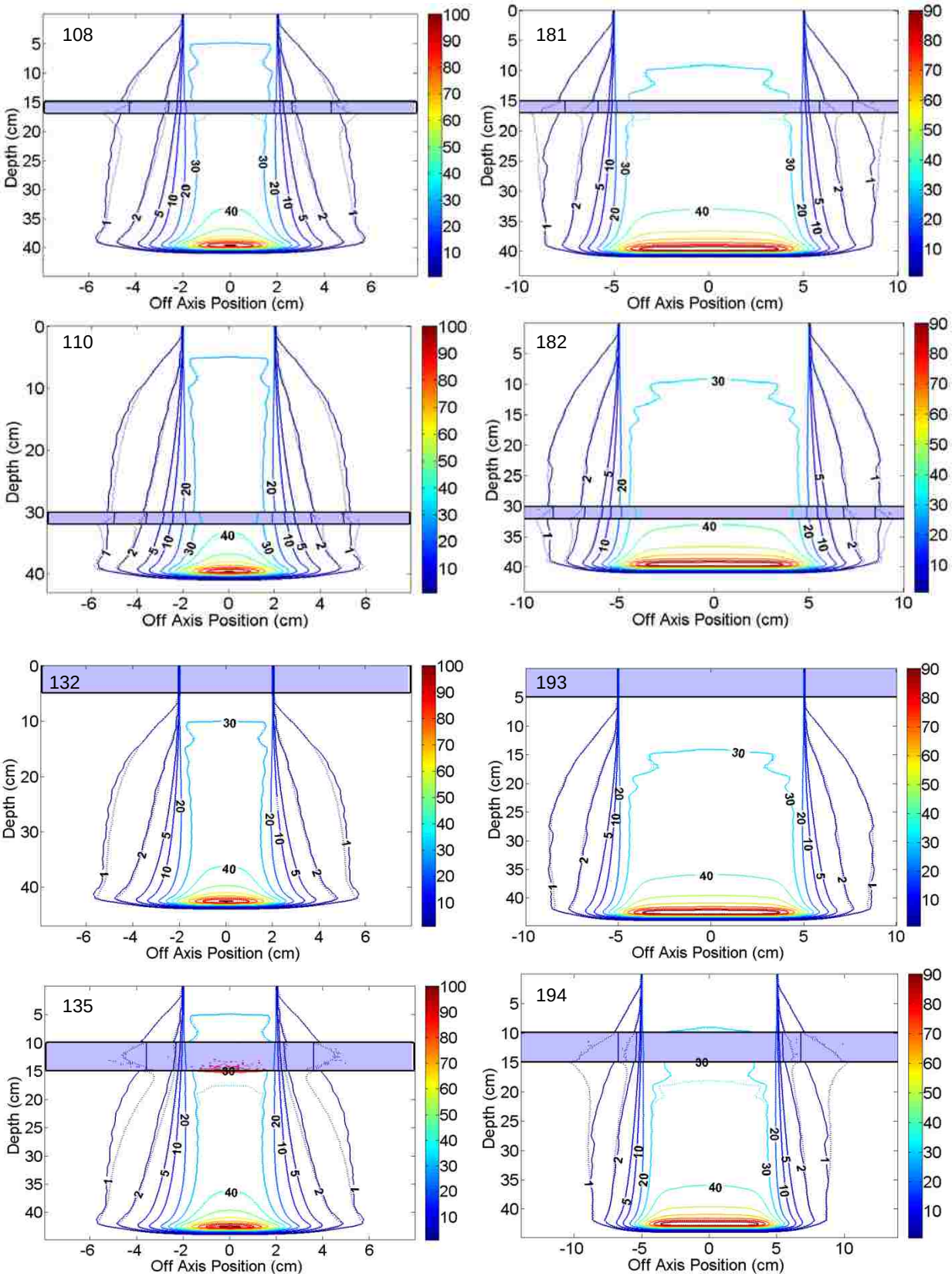
108
181
110
182
132
193
135
194
Depth (cm)
Off Axis Position (cm)

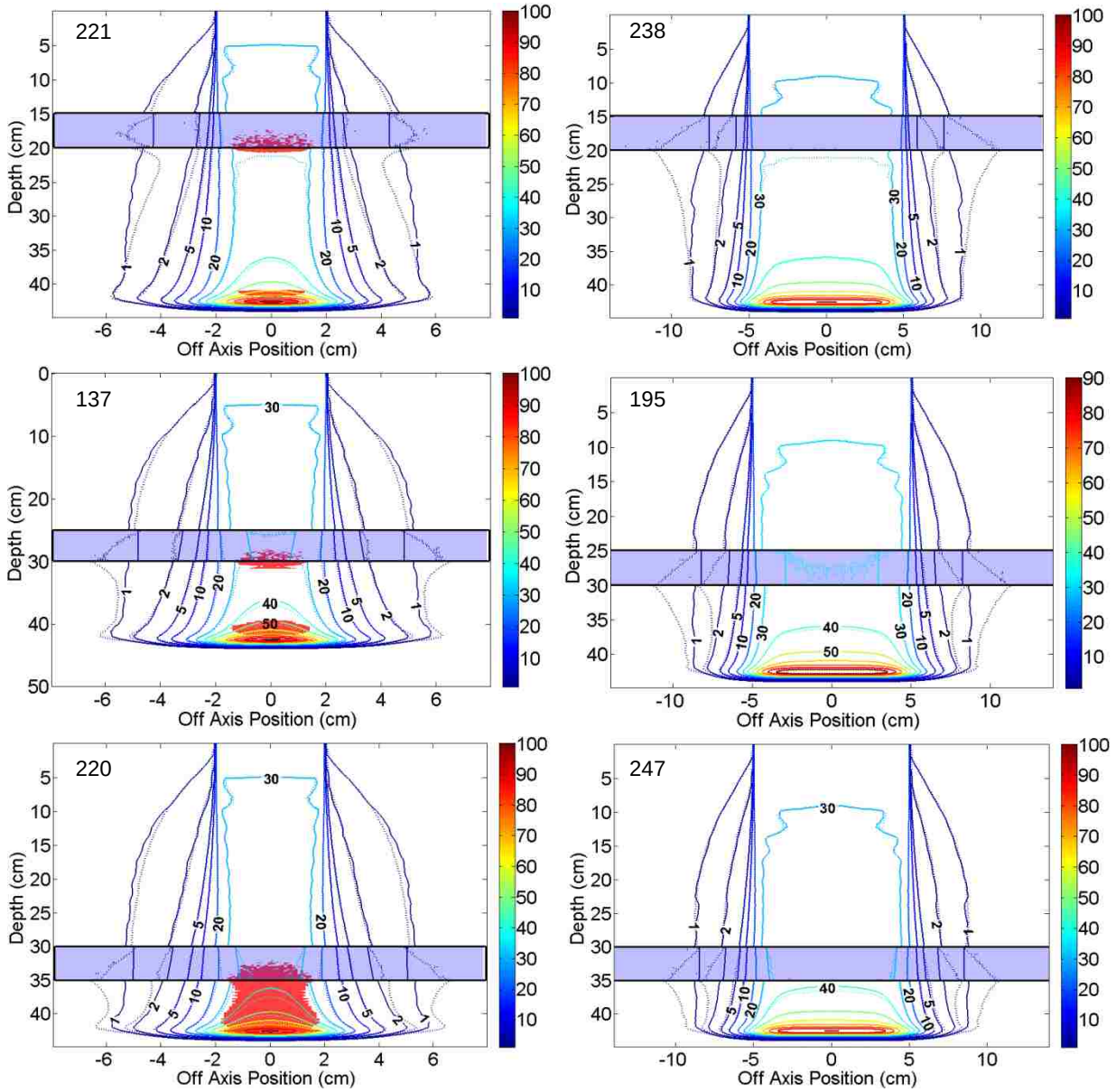

A5: Laterally Finite Compact Bone Slab Results

100 MeV Results

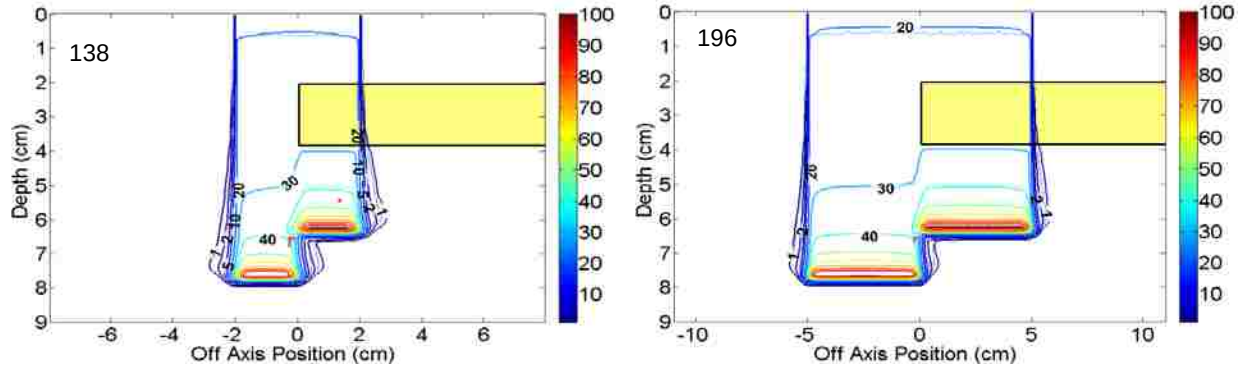

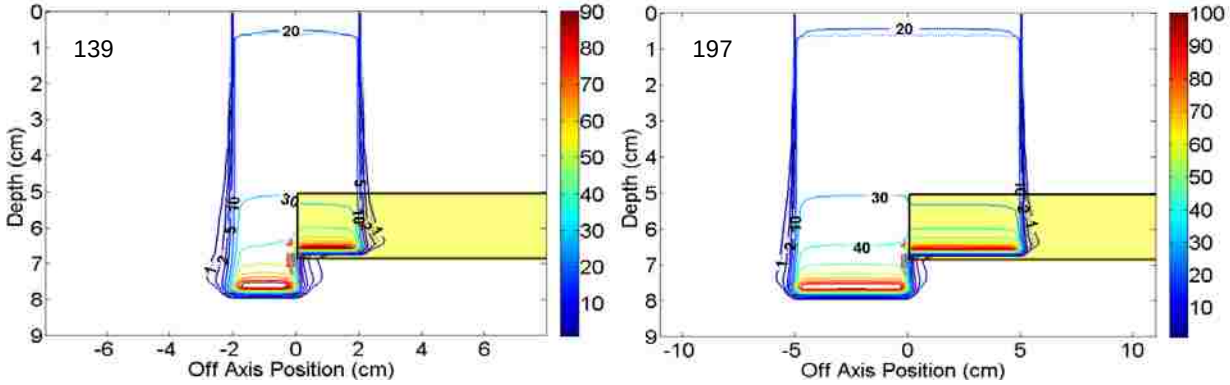

150 MeV Results

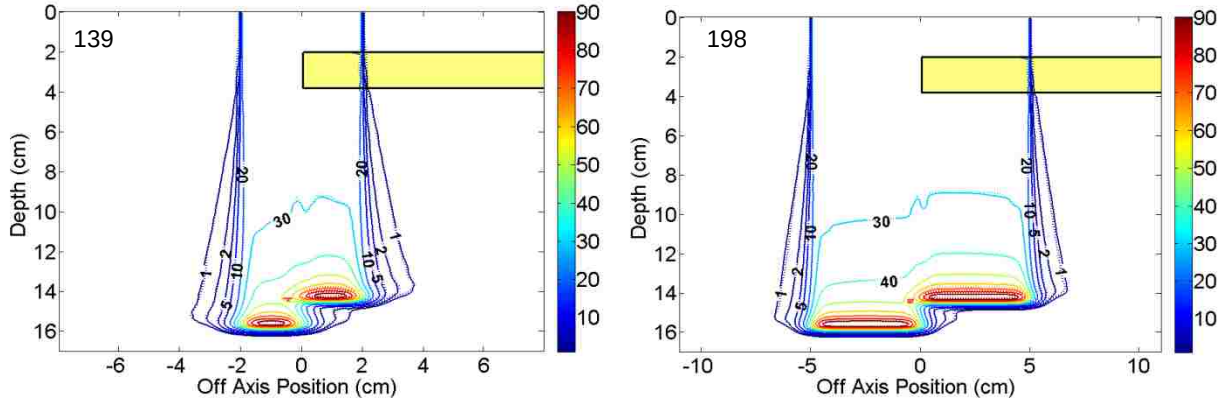

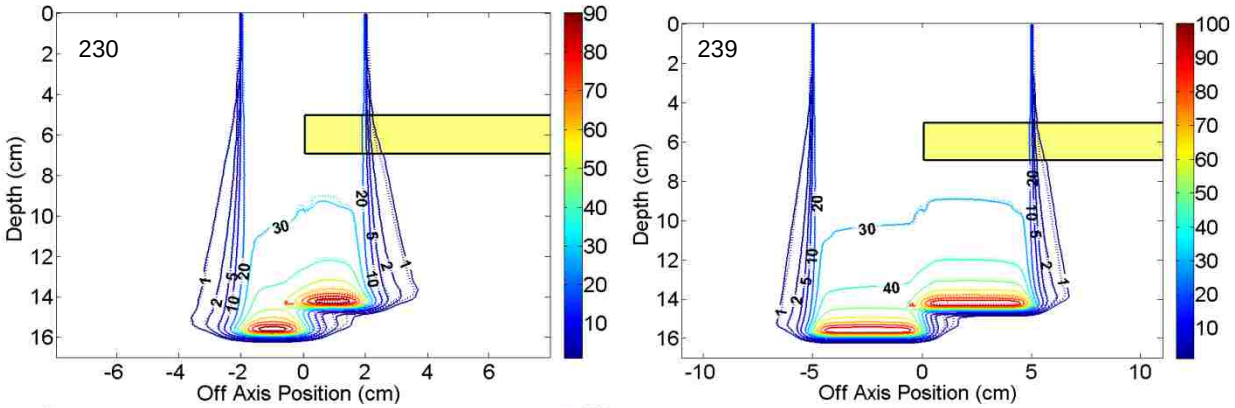

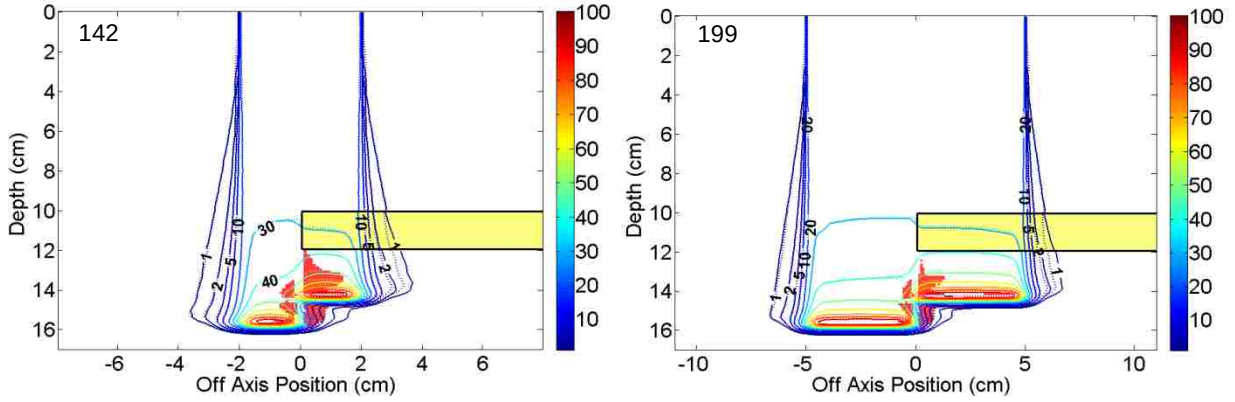

200 MeV Results

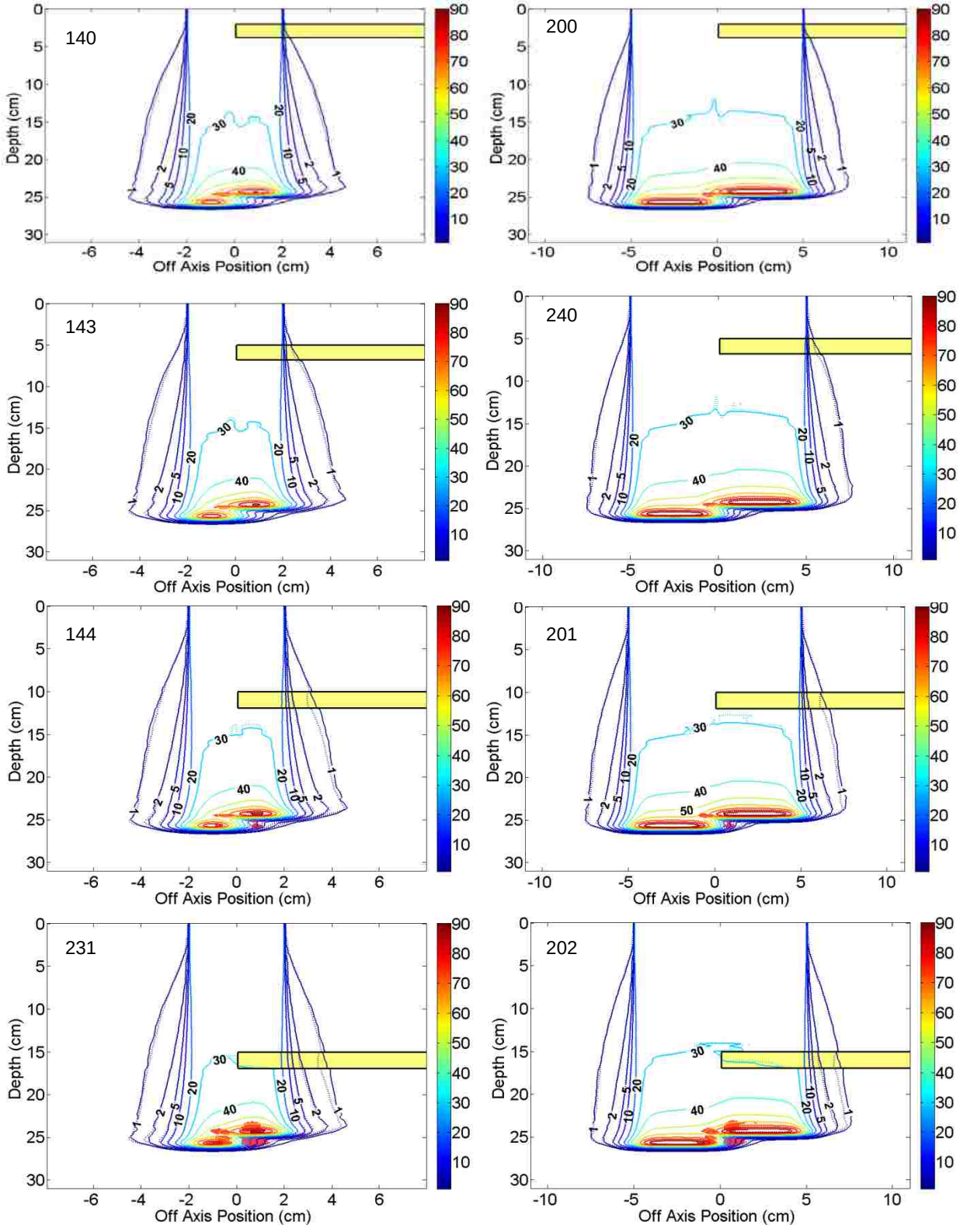

250 MeV Results

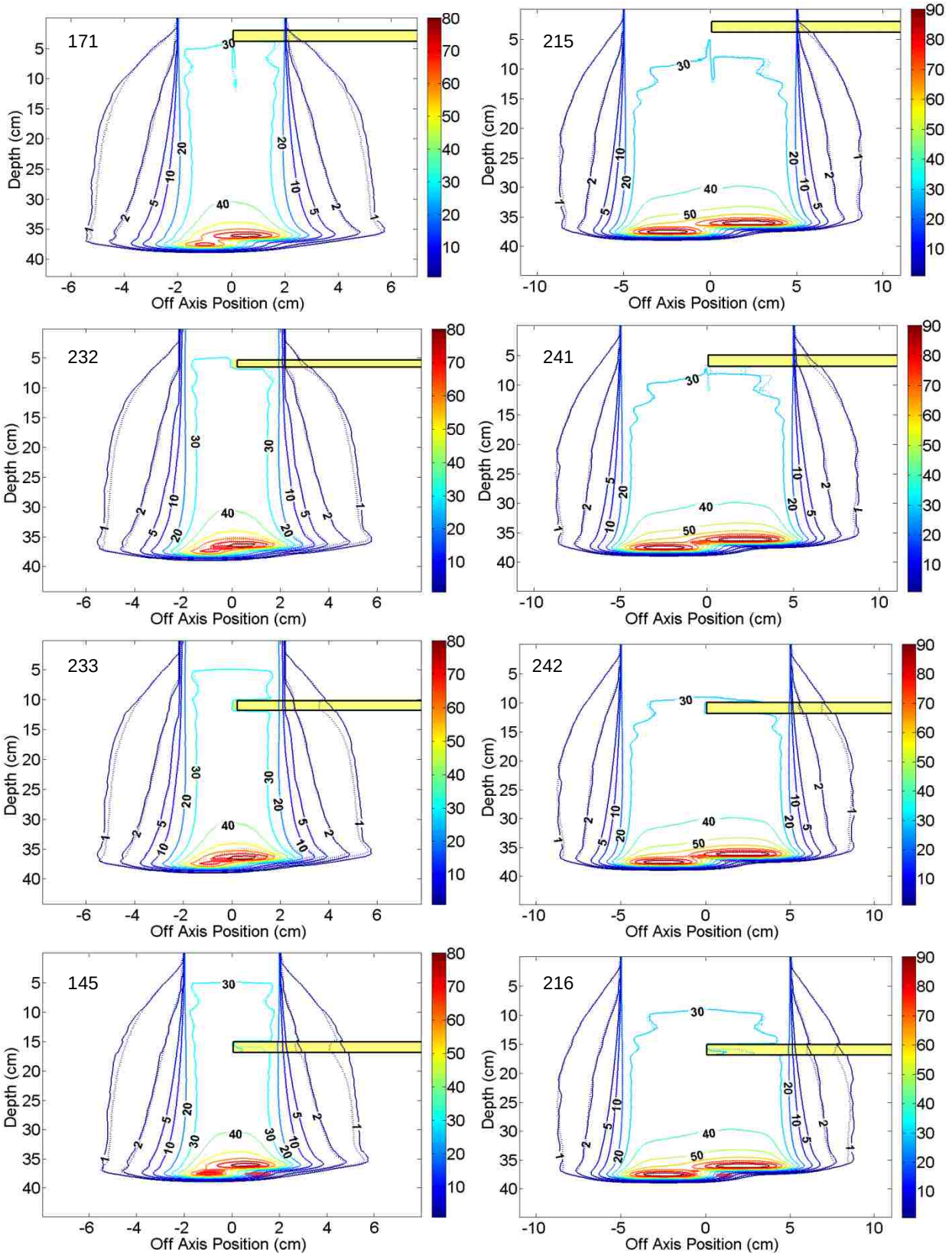

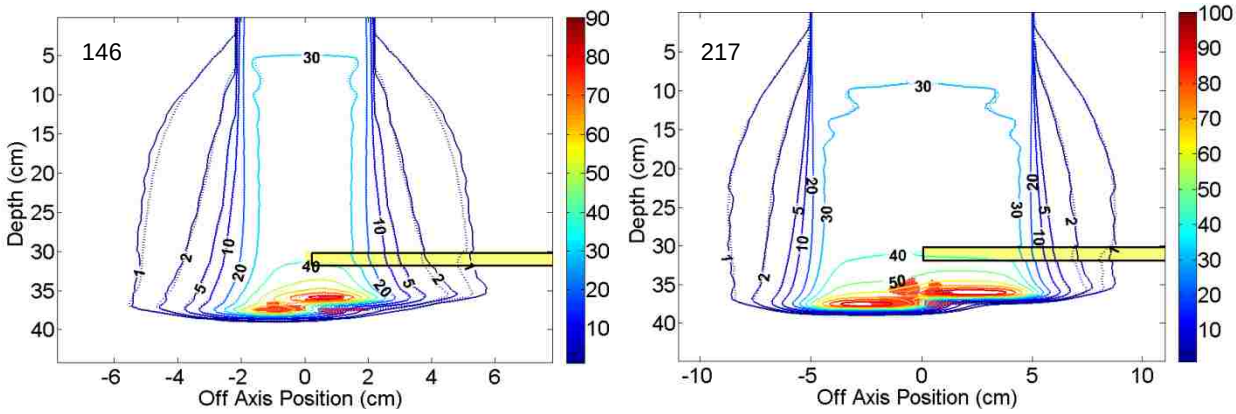

A6: Laterally Finite Air Slab Results

100 MeV Results

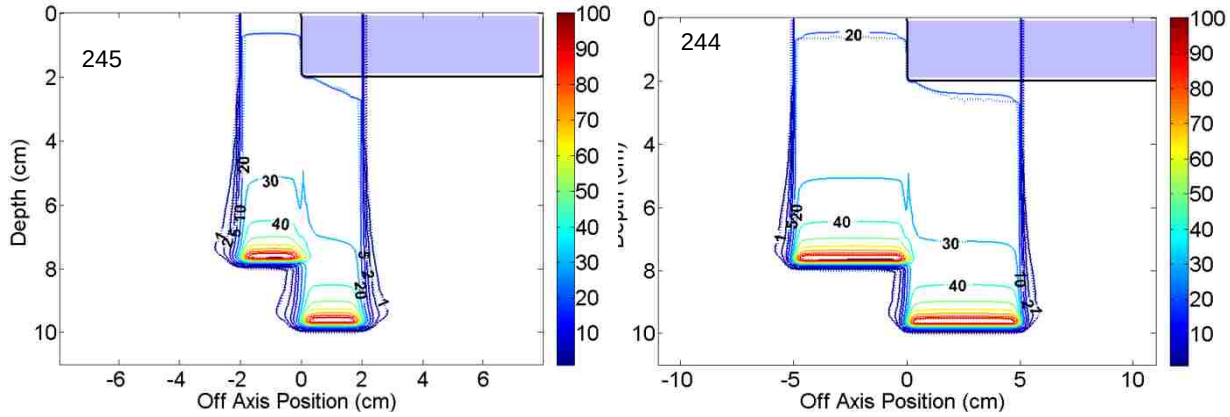

150 MeV Results

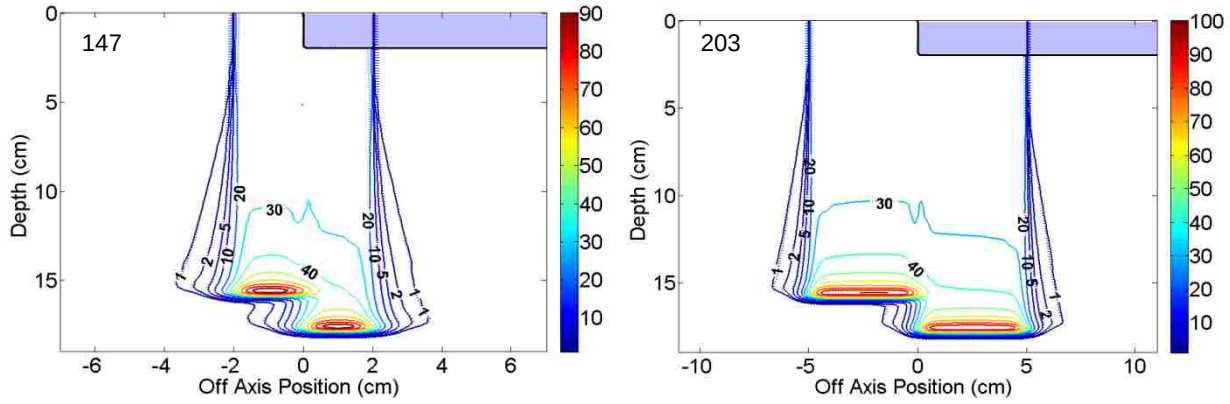

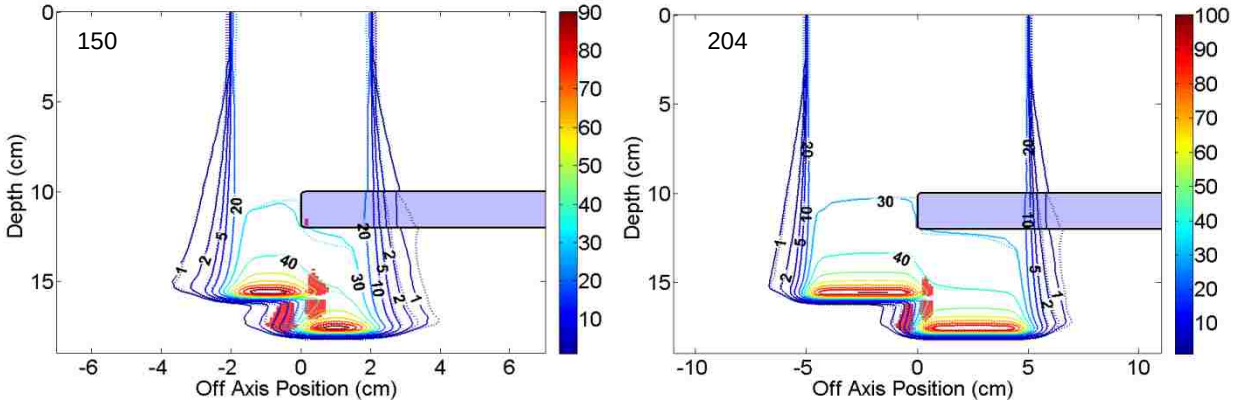

200 MeV Results

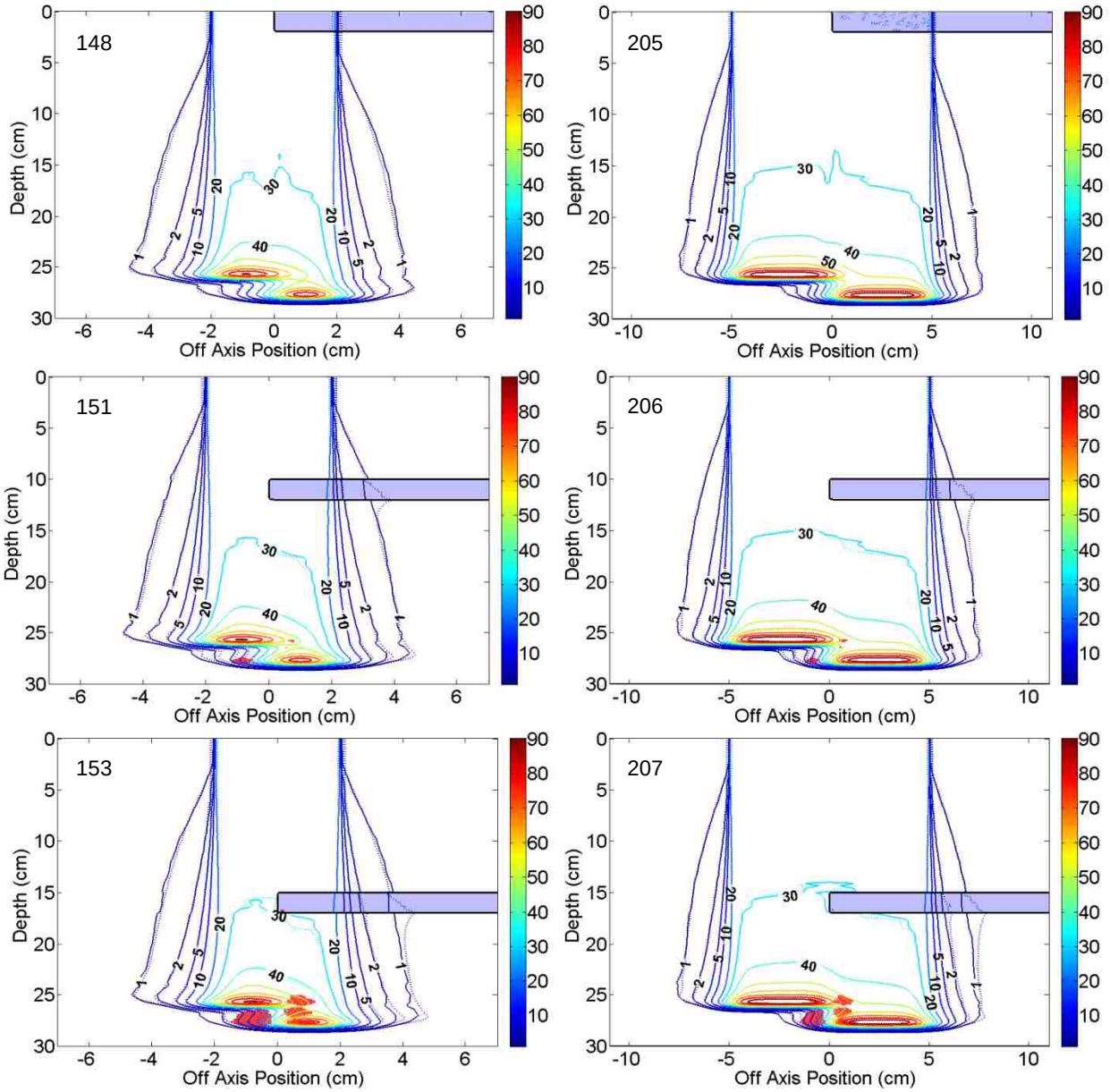

250 MeV Results

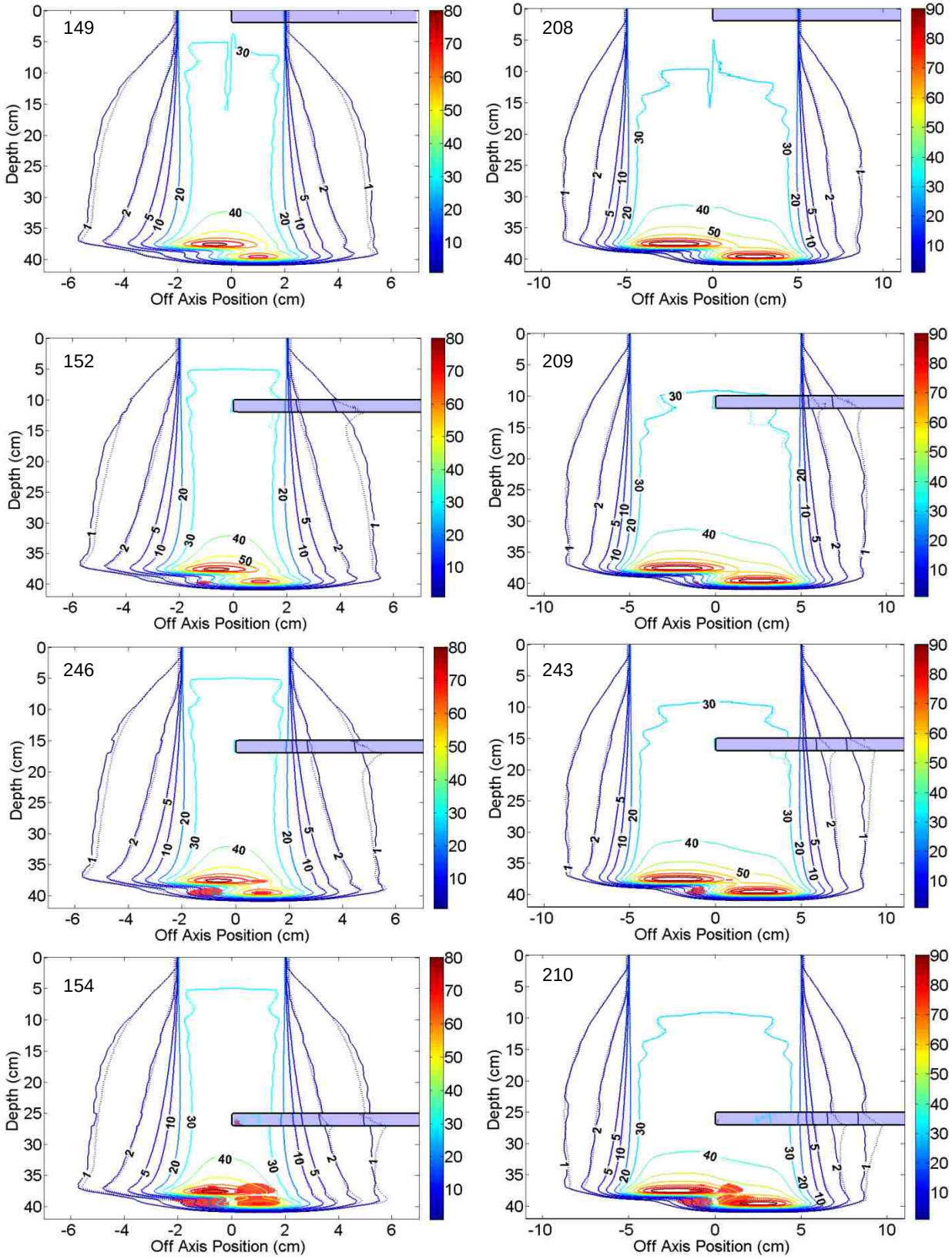

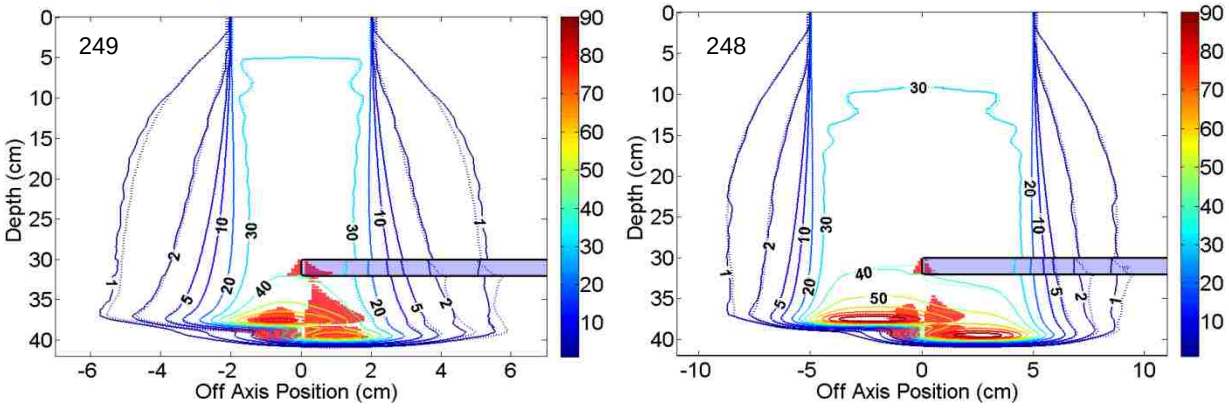

Figure A.1: Complete collection of 2D isodose comparisons from this work.

Appendix B: Table of Results & Data

In this chapter all of the result data of every test geometry dose comparison done in this work has been put in this single table. Each simulation was given a tag number and entered in the table. The initial energy, field size, slab material, slab thickness, slab width, and the depth where the slab was located were specified. The slab width was described as either laterally infinite (Inf) or laterally finite (Fin). Along with the parameters of the dose calculation geometry, the pass rate, mean dose difference of the all the pixels tested (MeanDD total), max dose difference of all the pixels tested (MaxDD Total), mean dose difference of the all the failing pixels (MeanDD in Failure), and maximum dose difference of the all the failing pixels (MaxDD in Failure) was entered for each dose calculation.

Table B.1: Table of results and data from this study.

Table of Results & Data											
Tag #	**Eo**	**FS**	**Slab Mat.**	**Slab Depth**	**Slab Thick**	**Slab Width**	**Pass Rate**	**MeanDD Total**	**MaxDD Total**	**MeanDD in Failure**	**MaxDD in Failure**
64	100	4	Bone	2	2	Inf	100	2.11	44.36	0	0
65	150	4	Bone	2	2	Inf	100	0.81	23.91	0	0
66	200	4	Bone	2	2	Inf	100	0.39	15.35	0	0
67	250	4	Bone	2	2	Inf	100	0.15	4.97	0	0
74	100	4	Bone	0	60	Inf	100	0.4	4.72	0	0
75	150	4	Bone	0	60	Inf	99.31	0.45	3.18	2.69	3.18
76	200	4	Bone	0	60	Inf	99.43	0.57	3.83	2.81	3.66
77	250	4	Bone	0	60	Inf	97.86	0.8	6.44	3.08	6.44
82	250	4	Water	0	60	Inf	100	0.08	1.64	0	0
88	100	4	Air	2	2	Inf	100	0.39	6.25	0	0
89	150	4	Air	2	2	Inf	100	0.2	2.76	0	0
90	200	4	Air	2	2	Inf	100	0.15	1.68	0	0
91	250	4	Air	2	2	Inf	100	0.15	3.74	0	0
92	100	4	Air	5	2	Inf	100	0.46	6.24	0	0
93	150	4	Air	10	2	Inf	100	0.27	2.66	0	0
106	200	4	Air	10	2	Inf	100	0.2	1.95	0	0
107	200	4	Air	15	2	Inf	100	0.21	1.98	0	0
108	250	4	Air	15	2	Inf	100	0.21	4.13	0	0
110	250	4	Air	30	2	Inf	99.96	0.2	2.73	2.62	2.73

Table of Results & Data cont.											
Tag #	Eo	FS	Slab Mat.	Slab Depth	Slab Thick	Slab Width	Pass Rate	MeanDD Total	MaxDD Total	MeanDD in Failure	MaxDD in Failure
126	150	4	Bone	0	5	Inf	100	0.64	14.17	0	0
127	200	4	Bone	0	5	Inf	100	0.33	8.85	0	0
128	250	4	Bone	0	5	Inf	100	0.16	2.03	0	0
129	100	4	Air	0	5	Inf	100	0.26	6.29	0	0
130	150	4	Air	0	5	Inf	100	0.11	2.08	0	0
131	200	4	Air	0	5	Inf	100	0.1	1.54	0	0
132	250	4	Air	0	5	Inf	100	0.12	2.47	0	0
133	150	4	Air	10	5	Inf	100	0.49	2.99	0	0
134	200	4	Air	10	5	Inf	100	0.39	2.55	0	0
135	250	4	Air	10	5	Inf	99.16	0.41	3.88	2.36	3.88
136	200	4	Air	15	5	Inf	99.69	0.42	3.24	2.06	2.26
137	250	4	Air	25	5	Inf	96.69	0.43	5.83	2.89	5.83
138	100	4	Bone	2	2	Fin	99.85	1.06	44.37	2.78	4.21
139	150	4	Bone	2	2	Fin	99.95	0.43	23.11	3.19	4.41
140	200	4	Bone	2	2	Fin	99.83	0.23	12.34	3.39	5.54
141	100	4	Bone	5	2	Fin	98.93	0.49	20.96	9.16	20.96
142	150	4	Bone	10	2	Fin	95.76	0.65	24.37	5.48	17.58
143	200	4	Bone	10	2	Fin	99.39	0.3	12.82	3.3	6.95
144	200	4	Bone	15	2	Fin	97.61	0.4	13.52	5.15	13.03
145	250	4	Bone	15	2	Fin	99.37	0.18	4.78	3.2	4.3
146	250	4	Bone	30	2	Fin	98.96	0.41	20.44	12.19	20.44
147	150	4	Air	0	2	Fin	100	0.27	5.21	0	0
148	200	4	Air	0	2	Fin	100	0.19	5.89	0	0
149	250	4	Air	0	2	Fin	100	0.16	7.05	0	0
150	150	4	Air	10	2	Fin	97.58	0.53	11.77	4.82	11.77
151	200	4	Air	10	2	Fin	99.81	0.25	5.82	2.84	4.02
152	250	4	Air	10	2	Fin	99.92	0.21	6.95	2.42	2.95
153	200	4	Air	15	2	Fin	98.09	0.37	8.99	4.28	8.99
154	250	4	Air	25	2	Fin	97.54	0.37	12.82	5.59	12.82
155	250	4	Bone	30	2	Inf	99.99	0.16	5.21	2.29	2.33
156	100	4	Water	0	60	Inf	100	0.09	1.54	0	0
157	150	4	Water	0	60	Inf	100	0.05	1.36	0	0
158	200	4	Water	0	60	Inf	100	0.06	1.48	0	0
159	100	10	Water	0	60	Inf	100	0.11	1.65	0	0
160	150	10	Water	0	60	Inf	100	0.05	1.39	0	0
161	200	10	Water	0	60	Inf	100	0.06	1.5	0	0
162	250	10	Water	0	60	Inf	100	0.06	1.47	0	0
163	100	10	Bone	2	2	Inf	100	2.15	44.53	0	0

Table of Results & Data cont.											
Tag #	Eo	FS	Slab Mat.	Slab Depth	Slab Thick	Slab Width	Pass Rate	MeanDD Total	MaxDD Total	MeanDD in Failure	MaxDD in Failure
164	150	10	Bone	2	2	Inf	100	0.9	24.02	0	0
165	200	10	Bone	2	2	Inf	100	0.48	15.39	0	0
166	250	10	Bone	2	2	Inf	100	0.18	4.71	0	0
167	100	10	Bone	0	60	Inf	100	0.28	4.59	0	0
168	150	10	Bone	0	60	Inf	99.67	0.24	2.74	2.33	2.72
169	200	10	Bone	0	60	Inf	99.85	0.32	2.67	2.37	2.67
170	250	10	Bone	0	60	Inf	100	0.53	2.19	0	0
171	250	4	Bone	2	2	Fin	100	0.13	4.51	0	0
172	250	10	Bone	30	2	Inf	100	0.15	4.62	0	0
173	100	10	Air	2	2	Inf	100	0.4	6.23	0	0
174	100	10	Air	5	2	Inf	100	0.41	6.19	0	0
175	150	10	Air	2	2	Inf	100	0.17	2.82	0	0
176	150	10	Air	10	2	Inf	100	0.19	2.64	0	0
177	200	10	Air	2	2	Inf	100	0.12	2.5	0	0
178	200	10	Air	10	2	Inf	100	0.15	2.46	0	0
179	200	10	Air	15	2	Inf	100	0.16	2.2	0	0
180	250	10	Air	2	2	Inf	100	0.13	3.38	2.14	2.14
181	250	10	Air	15	2	Inf	100	0.18	3.42	0	0
182	250	10	Air	30	2	Inf	100	0.16	3.41	0	0
183	100	10	Air	0	5	Inf	100	0.21	1.66	0	0
184	150	10	Air	0	5	Inf	100	0.12	2.06	0	0
185	150	10	Air	10	5	Inf	100	0.34	2.64	0	0
186	200	10	Air	0	5	Inf	99.99	0.1	2.1	2.06	2.1
187	200	10	Air	10	5	Inf	100	0.29	2.44	0	0
188	200	10	Air	15	5	Inf	100	0.33	2.18	0	0
189	150	10	Bone	0	5	Inf	100	0.63	14.27	0	0
190	200	10	Bone	0	5	Inf	100	0.34	9.1	0	0
191	250	10	Bone	0	5	Inf	100	0.18	1.65	0	0
192	250	10	Bone	30	5	Inf	99.79	0.13	5.66	2.81	4.4
193	250	10	Air	0	5	Inf	100	0.1	2.88	0	0
194	250	10	Air	15	5	Inf	100	0.3	3.37	0	0
195	250	10	Air	25	5	Inf	100	0.32	3.52	0	0
196	100	10	Bone	2	2	Fin	99.93	1.06	44.68	2.99	4.3
197	100	10	Bone	5	2	Fin	99.56	0.37	21.12	9.29	21.08
198	150	10	Bone	2	2	Fin	99.97	0.47	24.06	3.32	4.52
199	150	10	Bone	10	2	Fin	98.24	0.56	24.97	5.64	17.58
200	200	10	Bone	2	2	Fin	99.9	0.26	15.31	3.48	6.08
201	200	10	Bone	10	2	Fin	99.62	0.31	15.71	3.43	9.43

Table of Results & Data cont.											
Tag #	Eo	FS	Slab Mat.	Slab Depth	Slab Thick	Slab Width	Pass Rate	MeanDD Total	MaxDD Total	MeanDD in Failure	MaxDD in Failure
202	200	10	Bone	15	2	Fin	98.66	0.36	16.13	5.11	13.48
203	150	10	Air	0	2	Fin	100	0.18	5.17	0	0
204	150	10	Air	10	2	Fin	98.91	0.32	11.46	4.83	11.46
205	200	10	Air	0	2	Fin	100	0.13	5.69	0	0
206	200	10	Air	10	2	Fin	99.88	0.19	5.69	2.79	4.06
207	200	10	Air	15	2	Fin	99.01	0.25	8.82	4.39	8.82
208	250	10	Air	0	2	Fin	100	0.11	6.5	0	0
209	250	10	Air	10	2	Fin	99.99	0.16	6.48	2.2	2.38
210	250	10	Air	25	2	Fin	98.66	0.26	11.33	5.27	11.33
215	250	10	Bone	2	2	Fin	100	0.13	4.57	0	0
216	250	10	Bone	15	2	Fin	99.79	0.14	4.34	2.93	3.97
217	250	10	Bone	30	2	Fin	98.6	0.23	19.88	7.25	19.88
220	250	4	Air	30	5	Inf	93.2	0.45	6.9	3.01	6.9
221	250	4	Air	15	5	Inf	98.17	0.45	4.43	2.41	4.43
225	250	4	Bone	30	5	Inf	99.47	0.19	5.78	3.89	5.78
226	150	4	Air	5	2	Inf	100	0.23	2.72	0	0
227	200	4	Air	5	2	Inf	100	0.17	1.89	0	0
228	250	4	Air	5	2	Inf	100	0.17	2.07	0	0
229	250	4	Air	10	2	Inf	100	0.2	2.14	0	0
230	150	4	Bone	5	2	Fin	99.74	0.48	23.33	2.68	4.25
231	200	4	Bone	5	2	Fin	99.85	0.24	12.54	3.43	5.35
232	250	4	Bone	5	2	Fin	99.81	0.42	24.13	11.79	14.76
233	250	4	Bone	10	2	Fin	99.8	0.44	24.98	11.27	14.47
234	150	10	Air	5	2	Inf	100	0.22	2.67	0	0
235	200	10	Air	5	2	Inf	100	0.15	2.18	0	0
236	250	10	Air	5	2	Inf	99.99	0.11	3.08	2.37	2.74
237	250	10	Air	10	2	Inf	100	0.14	3.22	2.01	2.01
238	250	10	Air	15	5	Inf	99.99	0.32	3.11	2.05	2.09
239	150	10	Bone	5	2	Fin	99.89	0.5	24.24	3	4.35
240	200	10	Bone	5	2	Fin	99.91	0.28	15.54	3.29	5.47
241	250	10	Bone	5	2	Fin	99.88	0.19	10.63	3.22	5.14
242	250	10	Bone	10	2	Fin	99.84	0.2	10.6	3.27	5.21
243	250	10	Air	15	2	Fin	99.77	0.17	6.48	2.79	3.96
244	100	10	Air	0	2	Fin	100	0.39	7.4	0	0
245	100	4	Air	0	2	Fin	100	0.56	7.36	0	0
246	250	4	Air	15	2	Fin	99.41	0.24	6.95	3.06	4.67
247	250	10	Air	30	5	Inf	99.99	0.36	4.92	2.04	2.07
248	250	10	Air	30	2	Fin	97.96	0.32	17.75	6.43	17.75
249	250	4	Air	30	2	Fin	96.15	0.49	19.84	6.48	19.84

Vita

Nels Knutson was born in Williston, North Dakota in 1985. He grew up living at Blacktail Dam, a lake 30 miles north of Williston. After high school he went to college at the University of Montana where he received a B.A. in Physics in 2007 and a B.A. in Mathematics in 2009. In the summer of 2012 he will receive a Master of Science degree in Medical Physics and Health Physics from Louisiana State University. In July of 2012 he will start his Medical Physics residency at Washington University in St Louis. After the completion of his residency he hopes to pursue a Ph D. in Medical Physics and complete his ABR certification; ultimately pursuing a career as both an academic and clinical Physicist.